CHARACTERIZING ICE CLOUD PARTICLE SHAPE AND SURFACE ROUGHNESS FROM POLARIMETRIC SATELLITE OBSERVATIONS

A Dissertation

by

SOUICHIRO HIOKI

Submitted to the Office of Graduate and Professional Studies of
Texas A&M University
in partial fulfillment of the requirements for the degree of

DOCTOR OF PHILOSOPHY

Chair of Committee,	Ping Yang
Committee Members,	Kenneth P. Bowman
	Anita Rapp
	Lifan Wang
	Jérôme Riedi
Head of Department,	Ping Yang

August 2018

Major Subject: Atmospheric Sciences

ABSTRACT

The single scattering properties of ice cloud particles are inferred from spaceborne multi-angle satellite sensors with two newly developed noise-resilient retrieval techniques. The first presented method parameterizes the phase function and phase matrix elements by a few parameters to implement the maximum likelihood estimation in the retrieval system. The second method retrieves the renormalized phase function as a difference from a known phase function. The effect of noise is more predictable for both methods than the conventional "best-fit" method, which selects the best-fitting shape and surface roughness from a predetermined particle set.

The first method is applied to the data from the Polarization and Directionality of the Earth's Reflectance (POLDER) sensor. The retrieval results indicate that long column shape (ratio of basal face diameter to prism height greater than 9) with surface roughness parameter between 0.1 and 0.5 represents the extratropical observations well. Weak temperature dependence of the surface roughness is found in the extratropical data stratified by the cloud top temperature. The tropical retrieval was not successful, and the second method is applied to the Multi-angle Imaging Spectroradiometer (MISR) data. Short hexagonal column particles or their aggregates are found to match with estimated renormalized phase function. In addition to these results, the surface roughness simulation is summarized and the derivation of the δ-fit truncation technique for polarimetric radiative transfer is included.

ACKNOWLEDGEMENTS

I would like to thank my committee chair, Dr. Yang, and my committee members, Dr. Bowman, Dr. Rapp, Dr. Wang, and Dr. Riedi for their support and beneficial comments throughout the course of this research.

Thanks go to my friends and colleagues for having valuable discussions about the research project, and the department faculty and staff for making my graduate life at Texas A&M University a great experience. I am particularly grateful to Dr. Lei Bi and Dr. Bingqiang Sun for their help in light scattering theory and calculations. I also would like to thank Dr. Bingqi Yi, Dr. Guanglin Tang, Dr. Yifeng Ding, Dr. Masanori Saito, and Mr. Adam Bell for having discussions regarding general circulation models, satellite sensors, and retrieval techniques. I am grateful to Dr. Steven Schroeder for his careful proofreading and many helpful suggestions to my papers, conference posters, and the dissertation. Last, but not least, I would like to emphasize that without the help by Dr. Chia-Pang Kuo, Dr. Guanglang Xu, Mr. Yi Wang, and Mr. Jiachen Ding, I could not finish the doctoral project. I am grateful for their warm encouragements and frequent discussions.

CONTRIBUTORS AND FUNDING SOURCES

The work was supported by a dissertation committee consisting of Professors Ping Yang, Kenneth P. Bowman, and Anita Rapp of the Department of Atmospheric Sciences, Professor Lifan Wang of the Department of Physics, and Professor Jérôme Riedi of the Université de Lille.

Data from the Polarization and Directionality of Earth's Reflectance (POLDER) sensor is acquired from the ICARE Data and Service Center. Data from the Moderate Resolution Spectroradiometer (MODIS) sensor is acquired from the NASA Level-1 and Atmosphere Archive & Distribution System (LAADS) Distributed Active Archive Center (DAAC). Data from the Multi-angle Spectroradiometer (MISR) sensor and Cloud-Aerosol Lidar with Orthogonal Polarization (CALIOP) are acquired from Atmospheric Science Data Center (ASDC) at NASA Langley Research Center. Data from the Atmospheric Infrared Sounder (AIRS) is obtained from the NASA DAAC.

A major portion of the research was conducted with advanced computing resources provided by Texas A&M High Performance Research Computing.

The research effort reported in this dissertation was partly supported by NASA Grants NNX11AR06G, NNX15AQ25G, NASA Earth and Space Science Fellowship (NESSF, NNX15AP12H), and the endowment funds related to the David Bullock Harris Chair in Geosciences at the College of Geoscences, Texas A&M University.

TABLE OF CONTENTS

LIST OF FIGURES

FIGURES Page

LIST OF TABLES

1 INTRODUCTION

1.1 Brief history of ice particle models

Spaceborne cloud measurements have been providing new perspectives to atmospheric scientists for nearly six decades. In this chapter, I go over a brief history of ice particle models since the launch of the first meteorological satellite in 1960, summarize the concepts used in the later chapters of the thesis, and define the scope of the thesis.

1.1.1 Early years

The first meteorological satellite, the Television Infrared Observation Satellite (TIROS), was launched in 1960 (Stroud 1960), and the images acquired by the TIROS revealed the unforeseen cloud structures of extratropical cyclones that stretch over thousands of kilometers (Fritz and Wexler, 1960). While TIROS images were initially used for qualitative analysis, it didn't take long before the quantitative analysis of measured satellite data emerged. Houghton and Smith (1970) summarized the theory and literature related to the estimation of vertical temperature profiles by then.

At approximately the same time, computation of the light scattering properties for cloud particles became feasible with the evolution of theory and improvements in computers. Deirmendjian (1964) computed the light scattering properties of water cloud and haze particles, and Houghton and Hunt (1971) pointed out that the spectral differences of scattering properties can be used to retrieve cloud microphysical

properties. These two studies assumed that cloud particles are spherical, for which the exact Mie theory solution is available.

While a spherical particle is a good assumption for water clouds, an ice cloud consists of highly nonspherical particles, and therefore significant research efforts were invested in calculating scattering properties of nonspherical particles. The first successful attempt was for an infinitely long circular cylinder (Wait 1955; Liou, 1972a,b). With Liou's results, Stephens (1980a,b) showed that the scattering properties of spherical particles and cylindrical particles are significantly different in terms of radiance. In addition, Asano and Yamamoto (1975) computed the scattering properties of spheroidal particles. The scattering calculations for cylinders and spheroids are numerically exact, and the theories are applicable at an arbitrary wavelength and particle size.

The calculations of single scattering properties (hereafter, light scattering calculations) are computationally expensive, and the downstream applications usually incorporate the results as look-up tables, or as a "database", a collection of look-up tables. Two primary downstream applications are radiative transfer calculations for general circulation models (GCM) and estimation of physical parameters from radiometers. Various ice particle models have been employed since the late 1980s when the particle size distribution in ice clouds became gradually known by intensive in-situ airborne measurements.

1.1.2 Ice particle models for GCM applications

Cloud models for a GCM application were initiated with a so-called cloud "bulk" radiative parameterization. Early GCMs, for example, Manabe and Wetherald (1967), used constant values of cloud reflectivity, transmissivity, and absorptivity. Later, Liou and Wittman (1979) computed these bulk radiative properties with rigorous light scattering and radiative transfer simulations. They assumed spherical and cylindrical particles and represented cloud bulk properties as polynomials of liquid/ice water path (integral of the mass of hydrometeors in the atmospheric column). Bulk radiative parameterization is no longer in use in contemporary GCMs after gradually being replaced by a new type of parameterization in the 1980s.

Most contemporary GCMs represent cloud radiative properties by three single scattering parameters, namely, mass extinction cross section (k_{ext}), single scattering albedo (ϖ, a variant of Greek letter π), and asymmetry parameter (g). All three parameters are functions of wavelength, hydrometeor type, and particle size. This kind of parameterization became popular after the adaptation of two-stream approximations in GCM radiative transfer calculations. The introduction of two-stream approximations allowed the calculation of multiple scattering to be embedded into GCMs. Wavelength dependence is handled by splitting the spectrum of solar and terrestrial radiations into dozens of subsections, called "bands", and the program executes the radiative transfer calculations for each band. Therefore, the total number of parameters is $3N_b$, where N_b is the number of bands.

The first "modern" parameterization was designed for water clouds by Slingo and Schrecker (1982), and Slingo (1989). Ebert and Curry (1992) introduced the same method to ice cloud parameterization, although their parameterization was not based on the effective radius (r_e) that is nowadays in use.

The development of GCM ice cloud parameterizations in the contemporary framework made progress in parallel with the development of light scattering calculation techniques. The single scattering properties of ice cloud particles needed for the modern parameterization are difficult to compute because the size distribution of ice particle is broad, spanning from a few μm to 1000 μm. Numerically exact methods are computationally too expensive to cover this entire size range.

The first contemporary parameterization is by Fu and Liou (1993). They combined the geometric optics method (GOM) for a hexagonal column particle (Takano and Liou, 1989) and a numerically exact method for a spheroidal particle. The combination was to overcome the limited accuracy of the GOM when particle size becomes comparable to the wavelengths, which is often the case for infrared wavelengths. At that time, covering the entire shortwave and longwave spectrum with a consistent particle shape was not practical.

Another significant advance was the improved geometric optics method (IGOM, Yang and Liou, 1996). The method can compute scattering properties of smaller particles than the GOM without losing accuracy while maintaining efficiency. Fu (1996) developed a new parameterization by combining the GOM and IGOM at shortwave

wavelengths, but the counterpart for the infrared (Fu et al., 1998) was still computed with the Mie theory, anomalous diffraction theory (ADT), and IGOM.

The diversity of particle shapes in parameterizations has increased since 2000. Yang et al. (2000) covered six particle shapes and Yang et al. (2005) parameterized based on Moderate Resolution Imaging Specrtroradiometer (MODIS) Collection 4 habit mixture model. Hong et al. (2009) revised the parameterization with the MODIS Collection 5 mixture model. The details of the mixture models are provided in Section 1.2.

At approximately the same time as the development of the GOM and IGOM, Mitchell et al. (1996) proposed to apply the modified anomalous diffraction theory (MADT) to the GCM parameterization. The method can compute two of three contemporary parameterization parameters, mass extinction coefficient and single scattering albedo. The asymmetry parameter is obtained from the GOM, assuming a surrogate shape for plate aggregates. The ice radiative parameterization in the latest version of the National Center for Atmospheric Resarch (NCAR) Community Atmospheric Model (CAM5) is the descendant of Mitchell's model (Neale et al., 2012), but the mixing ratio of ice crystal shapes is different (7% hexagonal columns, 50% bullet rosettes, 43% irregular particles for maximum dimension $D_{max} > 60$ μm and 50% quasi-spherical particles, 30% irregular particles, and 20% bullet rosette for $D_{max} < 60$ μm).

1.1.3 Ice particle models for satellite retrievals

While the contemporary GCM parameterization requires only three parameters to represent the scattering properties of ice cloud particles, radiance calculations for satellite applications require detailed scattering properties. This difference is because satellite applications require a simulation of radiant intensity as a function of viewing directions while GCM applications use the directional average of radiant flux only.

Two parameters are the same as in the GCM parameterization: mass extinction cross section (k_{ext}) and single scattering albedo (ϖ). The other parameter, asymmetry parameter (g), is replaced with phase function ($\mathcal{P}(\vec{\Omega}_{sca}, \vec{\Omega}_{in})$). In general, a phase function is a function of two directions: the incident direction $\vec{\Omega}_{in}$ and scattered direction $\vec{\Omega}_{sca}$, and describes the directional distribution of scattered radiant intensity. The asymmetry parameter (g) used in the GCM parameterization is an integral of a phase function. These three properties, k_{ext}, ϖ, and $\mathcal{P}(\vec{\Omega}_{sca}, \vec{\Omega}_{in})$ are computed for every spectral channel of satellite sensors. At first, the single scattering properties were computed only at the center wavelength, but most contemporary operational data production scheme uses scattering properties averaged over the receiver's spectral response (channel-average properties).

Like the GCM parameterizations, ice particle models for satellite retrieval developed over time to become increasingly realistic and complex. The term, "satellite retrieval" hereafter means the estimation of physical properties from spaceborne radiometric instruments. For example, the Moderate Resolution Imaging

Spectroradiometer (MODIS) measures radiant intensity at 36 spectral channels, and retrieves various parameters for the atmosphere, land, and ocean.

As previously mentioned, Houghton and Hunt (1971) modeled ice and water clouds as spherical particles and showed the feasibility of the retrieval of cloud particle size. In 1970s, several studies empirically derived the cloud top height and cloud phase (e.g. Shenk and Curran, 1973, Reynolds and Vonder Haar, 1977), but it was not common to use results from light scattering calculations. This is presumably because of the low resolution of satellite sensors and the extensive use of thermal infrared channels. At the time, research was primarily focused on the effective emissivity of clouds. However, some studies used shortwave channels. Platt (1983) used the cloud reflectivity computed by Liou (1973) with cylindrical ice particle.

The simultaneous retrieval of cloud optical thickness and effective radius with near-infrared channels became popular starting with works by Curran and Wu (1982) and Nakajima and King (1990). In these papers, they focused on water clouds, and light scattering calculations were based on Mie theory, but later, the near-infrared bispectral method was incorporated into operational algorithms for both water and ice clouds. Along with the increasing popularity of the near-infrared bispectral method, results from light scattering calculation using the GOM and IGOM were adopted by the research community. This is why various particle models have continued to be developed and tested since 2000.

The earliest adaptation of the near-infrared bispectral method was developed by the science team for the Moderate Resolution Imaging Spectroradiometer (MODIS). The

MODIS science team has developed three ice particle models specifically oriented for their ice microphysics retrieval. The first model was used in MODIS Collection 1 through 4. Two mixture bins were used: (1) 50% 4-element bullet rosettes, 25% hexagonal plates, and 25% hollow columns for $D_{max} < 70$ μm; and (2) 30% aggregates, 30% bullet rosettes, 20% hexagonal plates, and 20% hollow columns for $D_{max} > 70$ μm (Baum et al., 2000; King et al., 2004). The size distributions were obtained from in-situ measurements. The second model was used for MODIS Collection 5. The model was more complex because of the increased number of mixture bins: (1) 100% droxtals for $D_{max} < 60$ μm; (2) 50% solid columns, 35% hexagonal plates, and 15% 6-element bullet rosettes for $60 < D_{max} < 1000$ μm; (3) 45% solid columns, 45% hollow columns, 10% column aggregates for $1000 < D_{max} < 2000$ μm; and (4) 97% bullet rosette and 3% column aggregates for $D_{max} > 2000$ μm (Baum et al., 2005). These mixing ratios were determined to best explain airborne in-situ measurements of particle size distribution, ice water content, and median mass diameter. The same model is used for the Atmospheric Infrared Sounder (AIRS) version 6 retrievals. The third model by the MODIS science team is rather simple; it consists only of hexagonal column particles, regardless of particle maximum dimension, and gamma particle size distributions are assumed. This model was used in the production of the current MODIS Collection 6.

In the computation of MODIS particle models, the definition of maximum dimension (D_{max}) depends on particle shapes. D_{max} is defined as the crystal height for a hexagonal (solid and hollow) column, diameter of basal facets for a hexagonal plate, and the longest distance between two vertices for a column aggregate, bullet rosette, or

droxtal. The mixed scattering properties averaged over the particle size distribution are called “bulk” scattering properties. The precise definitions of bulk properties are well summarized by Baum et al. (2011).

The Cloud and the Earth’s Radiant Energy System (CERES) science team has developed three different ice particle models. For CERES Edition 2 and Edition 3 products, they used smooth hexagonal column particle models in eight discrete size bins to cover ten particle size distributions measured by airborne field campaigns (Minnis et al., 1998, 2011). Edition 4 keeps the particle shape and particle size distribution the same, while applying surface roughness to the particle model (Minnis 2017, personal communication). The planned Edition 5 will use a two-habit model (Loeb et al., 2018). The two-habit model consists of a roughened hexagonal column and the ensemble average of 20 random aggregates of 20 distorted hexagonal columns. The mixing ratios between the single column and the aggregates are determined based on the in-situ airborne measurements.

For retrievals from the Polarization and Directionality of the Earth’s Reflectance (POLDER) sensors, the inhomogeneous hexagonal particle model (IHM) is used (C.-Labonnote 2001). The particle shape of this model is a hexagonal column with aspect ratio (ratio of basal face diameter to column height) $AR = 0.2$, but inclusion of air bubbles is considered. The model is used to produce operational products from three POLDER sensors: POLDER-1 aboard Advanced Earth Observation Satellite (ADEOS), POLDER-2 aboard ADEOS-2, and POLDER-3 aboard Polarization and Anisotropy of

Reflectances for Atmospheric Sciences coupled with Observations from a Lidar (PARASOL).

In addition to these operational models, some other models have been proposed in the research community. Baran and C.-Labonnote (2007) produced an ice particle model that increases the morphological complexity with increasing sizes. Baum et al. (2011, 2014) advanced the approach used for the MODIS Collection 5 model and defined the general habit model (GHM).

1.2 Effect of particle shape on scattering properties

In Section 1.1 we summarized how ice particle models have evolved over time with a focus on two applications. For the GCM parameterization in the two-stream framework, the essential parameters are mass extinction cross section (k_{ext}), single scattering albedo (ϖ), and asymmetry parameter (g). For satellite retrieval applications, the first two parameters are used, and the phase function ($\mathcal{P}(\vec{\Omega}_{sca}, \vec{\Omega}_{in})$) replaces the asymmetry parameter. In this section, I describe how these scattering properties changes with particle shapes and surface roughness.

1.2.1 Mass extinction cross section

The largest effect of a varying particle shape is on the mass extinction cross section. At the limit of geometric optics, the extinction efficiency (Q_{ext}) is 2, and the extinction cross section of a single particle (σ_{ext}) is proportional to the projection area of the particle averaged over all incident radiation directions (σ) as follows:

$$\sigma_{ext} = Q_{ext}\sigma \rightarrow 2\sigma \text{ (geometric optics)} \quad (1.1)$$

As the mass extinction cross section is determined as $k_{ext} = \sigma_{ext}/v\rho_{ice}$, where v is the volume of a single particle and $\rho_{ice} = 917$ kg/m^3 is the mass of an ice particle, the mass extinction cross section can be written as:

$$k_{ext} \to \frac{2\sigma}{v\rho_{ice}} \tag{1.2}$$

at the limit of geometric optics. As the typical size of an ice cloud particle (several dozens of micrometers) is larger than the central wavelength of common shortwave channels (e.g. 0.865 μm), Eq. (1.2) means that the ratio of projection area to the particle volume primarily determines the mass extinction cross section in shortwave channels. In the actual atmosphere, ice clouds consist of many particles with various sizes. Thus, total projection area and total volume are used:

$$k_{ext} \to \frac{2A}{V\rho_{ice}}, \tag{1.3}$$

where

$$A = \int_{D_{max}}^{D_{max}} \sigma(D_{max}) \frac{dN}{dD_{max}} \, dD_{max}, \tag{1.4}$$

$$V = \int_{D_{max}}^{D_{max}} v(D_{max}) \frac{dN}{dD_{max}} \, dD_{max}, \tag{1.5}$$

and $N(D_{max})$ is the cumulative number concentration (i.e. $N(\infty)$ is the total number of particles per unit volume). Equation (1.3) implies that if two collections of particles have the same volume and number concentration, the collection containing bulky (less compact) particles with a larger total surface area has a larger mass extinction cross

section than compact particles, which means that interaction with the incident radiation is stronger.

The magnitude of interaction with incident radiation is characterized by optical thickness (τ). The optical thickness can be derived from the parameterized k_{ext} and ice water content IWC as follows:

$$\tau = lk_{ext}IWC \tag{1.6}$$

where l is the thickness of a cloud layer of interest. If a cloud stretches over multiple radiation calculation layers, the total cloud optical thickness is the sum of τ values in all individual layers. Since the cloud reflectivity in the shortwave increases monotonically with the increasing total cloud optical thickness, Eq. (1.6) means that the extinction cross section k_{ext} determines the cloud shortwave reflectivity for a given mass concentration. Because bulky particle has a higher mass extinction cross section, bulky particles produce higher shortwave reflectivity than compact particles for a given mass concentration. At infrared wavelengths, the increased optical thickness means more outgoing longwave radiation (OLR) originates in clouds. This increased contribution by clouds reduces the effective emission temperature to reduce the OLR. In summary, bulky particles have stronger cloud radiative effect than compact particles when the cloud contains the same mass and number of particles.

1.2.2 Single scattering albedo

The single scattering albedo (ϖ) characterizes the contribution of scattering and absorption when the incident light interacts with particles. With the mass absorption cross section (k_{abs}), ϖ is defined as follows:

$$\varpi = \frac{k_{ext} - k_{abs}}{k_{ext}}. \tag{1.7}$$

At the geometric optics limit, the mass absorption cross section is more sensitive to particle volume than the mass extinction cross section because the energy of a ray inside a particle decreases exponentially with the travel distance. The implication is that the mass absorption cross section is smaller when particles are bulky, as opposed to mass extinction cross section. Therefore, a bulky particle has higher ϖ than a compact particle as a result of combined effects.

Note that this discussion is valid when the number concentration is constant (i.e. total mass and number concentration are both fixed for a collection of particle). Since the ratio of projection area to the volume A/V is sensitive to particle size, the actual parameterization in the GCM has to take particle size into the account. In Section 1.3, we discuss how this particle size effect is implemented in GCM parameterizations.

1.2.3 Phase function and asymmetry parameter

The effect of particle shapes on the phase function is often visible in the sky as an optical phenomenon. For example, a rainbow requires spherical rain droplets to be visible, and a halo requires hexagonal ice particles. In addition to these noticeable features, the particle shape affects the asymmetry parameter (g). The asymmetry parameter is defined by a weighted integral of the phase function as follows:

$$g = \iint_{2\pi} \mathcal{P}\left(\vec{\Omega}_{sca}, \vec{\Omega}_{in}\right) \left[\vec{\Omega}_{sca} \cdot \vec{\Omega}_{in}\right] d\vec{\Omega}'_{sca}, \tag{1.8}$$

where $\vec{\Omega}_{sca} \cdot \vec{\Omega}_{in}$ is the cosine of the angle between directions of incident light and scattered light. The asymmetry parameter takes a value between -1 and 1, and becomes 0

when the scattering is isotropic. Complete forward scattering results in $g = 1$, and complete backward scattering results in $g = -1$. For typical ice particles at visible wavelengths, g ranges from 0.7 to 0.9.

For simple hexagonal column particles, the shortwave asymmetry parameter reaches a minimum when the aspect ratio (AR: ratio of basal face diameter to column height) is close to 1, and increases when the particle becomes either a long column ($AR < 1$) or a thin plate ($AR > 1$). Surface roughness reduces the asymmetry parameter and smoothens the phase function (Macke et al. 1996; Yang et al. 2008; van Diedenhoven 2012).

Since the asymmetry parameter describes the partitioning of scattered energy to forward and backward hemispheres, it plays a significant role in the GCM radiation calculations, particularly in the shortwave. For the same mass of ice, a cloud becomes more reflective when the asymmetry parameter is low. The asymmetry parameter also has an impact on the satellite retrievals. Loeb et al. (2018) showed that CERES-MODIS optical thickness is reduced after switching the particle model to one with a low asymmetry parameter, and Ding et al. (2017) pointed out that the retrieved optical thickness and asymmetry factor of the cloud model are correlated.

1.3 Three kinds of ice cloud models

Previous sections covered how ice cloud models have increased in complexity and how the assumptions of particle shape and surface roughness affects the radiative transfer calculations. This section identifies three types of cloud models used for the

GCM and remote sensing applications, and describe how variable shapes can be incorporated into these ice cloud models.

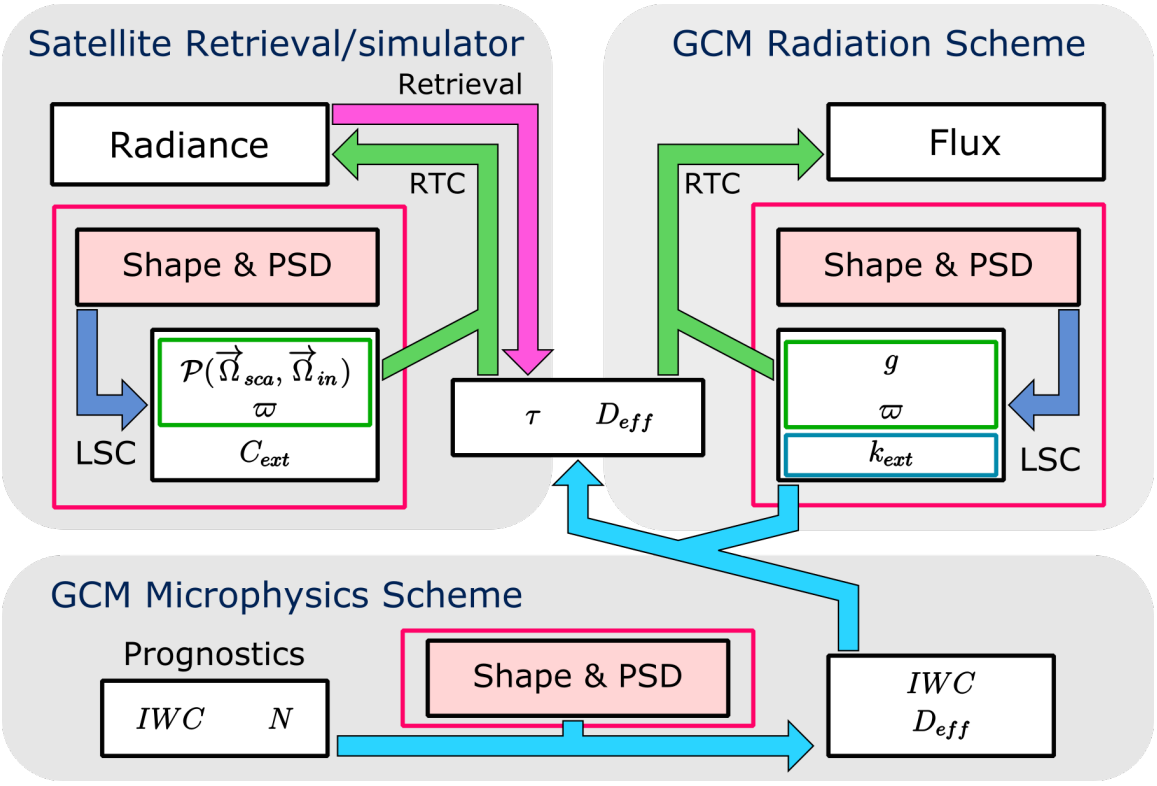

Fig. 1.1. Relations of physical quantities in the thesis. Three red boxes indicate ice particle models used in three major groups of computer programs. In the figure, RTC refers to Radiative Transfer Calculations, and LSC refers to the Light Scattering Calculations. g is asymmetry parameter, $\mathcal{P}(\vec{\Omega}_{sca}, \vec{\Omega}_{in})$ is phase function, k_{ext} is mass extinction cross section, C_{ext} is volumetric extinction cross section, τ is optical thickness, D_{eff} is effective diameter, IWC is ice water content, and N is number concentration.

Figure 1.1 shows three groups of computer programs that needs ice particle models: (1) Satellite retrievals/simulator, (2) GCM radiation scheme, and (3) GCM microphysics scheme. The ice particle models summarized in Section 1.1 was for (1) and

(2). While the three groups of programs are depicted in a format that resembles a flow chart, the figure illustrates general relations between physical quantities, and the groups do not necessarily need to be modules of any particular application. A satellite retrieval may provide physical parameters other than cloud optical thickness (τ) and effective diameter (D_{eff}) shown in Fig. 1.1, but to emphasize the link between GCM applications, only these two parameters are included.

In following subsections, I describe how ice particle models (enclosed by red boxes in Fig. 1.1) are implemented and related to each other.

1.3.1 Satellite retrieval / Satellite simulator

The goal of a satellite retrieval is to estimate physical properties from spaceborne radiometric measurements. The radiance data acquired by spaceborne sensors are processed through an inversion program to produce τ, D_{eff}, and other desired parameters (purple arrow in Fig. 1.1). This is an inverse process of radiative transfer calculation (RTC, green arrow in Fig 1.1.), which requires a specified ice particle model. The ice particle model consists of predetermined shape, particle size distribution, and single scattering properties that may have been inferred from field campaigns, laboratory measurements, or light scattering calculations (LSC).

The cloud models can also include horizontal and vertical variation of particle shape and size distribution, but this application to an operational algorithm is not common. Most satellite retrievals employ simplified models such as a 1-D radiative transfer model in a plane-parallel homogeneous atmosphere, even though the radiative transfer process that occurs in the Earth's atmosphere is fundamentally three-

dimensional (3-D) in nature. For example, the operational retrievals from satellite imaging sensors such as MODIS and CERES assume a 1-D plane-parallel homogeneous atmosphere with randomly oriented particles.

To perform satellite retrievals for a large number of data values operationally, the results of light scattering calculations are usually stored as look-up tables. The look-up table includes volumetric extinction cross section ($C_{ext} = k_{ext}/(v\rho)$), single scattering albedo (ϖ), and phase function ($\mathcal{P}(\vec{\Omega}_{sca} \cdot \vec{\Omega}_{in})$) for every channel of the satellite sensor. When particles are randomly oriented, the phase function can be simplified to be a function of scattering angle $\Theta = \cos^{-1}(\vec{\Omega}_{sca} \cdot \vec{\Omega}_{in})$. When the effect of polarization is included, the phase function is replaced by a 4 × 4 phase matrix $M(\Theta)$.

The single scattering properties are provided to the radiative transfer calculation programs (forward model), and an iterative process is often used to improve the retrieval parameters (e.g. τ and D_{eff}). In addition to the look-up table for the single scattering properties, the results of radiative transfer calculations are often stored in the look-up table for fast iteration. When only the forward component is used, this program group can be considered as satellite simulator. Satellite simulators are used to design a satellite sensor and to assimilate observational data to GCMs and numerical weather prediction (NWP) models.

1.3.2 GCM microphysics scheme

Most radiative transfer calculations employ a two-stream method, which requires optical thickness (τ), single scattering albedo (ϖ), and the asymmetry parameter (g). However, these three parameters do not come out of the GCM microphysics calculation

directly, and a two-stage conversion is implemented in contemporary GCMs. The first stage is implemented in the GCM microphysics scheme (horizontal blue arrow in Fig. 1.1), and the second is in the GCM radiation scheme (upward blue arrow in Fig. 1.1). In this subsection, the conversion implemented in the GCM microphysics scheme is described.

The first stage of conversion is purely geometric, and does not involve the results from light scattering calculations. The goal of the first conversion is to compute the effective diameter D_{eff}. The effective diameter is defined as follows:

$$D_{eff} = \frac{3V}{2A}, \tag{1.9}$$

where V is the total volume and A is the total cross section as defined in Eqs. (1.4) and (1.5). From the similar discussion of the shape dependence of mass extinction efficiency (k_{ext}), it can be derived that the effective diameter (D_{eff}) of compact particles is larger than the effective diameter of bulky particles, when the IWC and N are kept constant.

Bulk two-moment microphysics schemes (e.g. Morrison et al. 2005) used in current GCMs estimates ice water content (IWC) and number concentration (N), so therefore, D_{eff} is derived from these two parameters. In Morrison et al. (2005)'s scheme, the conversion is formulated by assuming cloud ice particles are spherical with a gamma distribution (Deirmendjian, 1964)

$$\frac{dN}{dD_{max}} = \frac{N(\infty)}{\beta\Gamma(\alpha)}\left(\frac{D_{max}}{\beta}\right)^{\alpha-1} e^{-\frac{D_{max}}{\beta}}, \tag{1.10}$$

where $N(D_{max})$ is the cumulative number concentration (i.e. $N(\infty)$ is the total number concentration), α is the shape parameter, β is the scale parameter, and $\Gamma(\alpha)$ is the gamma function.

In Morrison's scheme, $\alpha = 1$, and effective density $\rho_{eff} = 500$ kg/m^3. The rearranged equation of the conversion is as follows:

$$D_{eff} = \frac{3}{\rho_{ice}} \left(\frac{{\rho_{eff}}^2}{\pi} \frac{IWC}{N} \right)^{\frac{1}{3}}. \tag{1.11}$$

Therefore, the effect of nonsphericity can be incorporated by modifying ρ_{eff}.

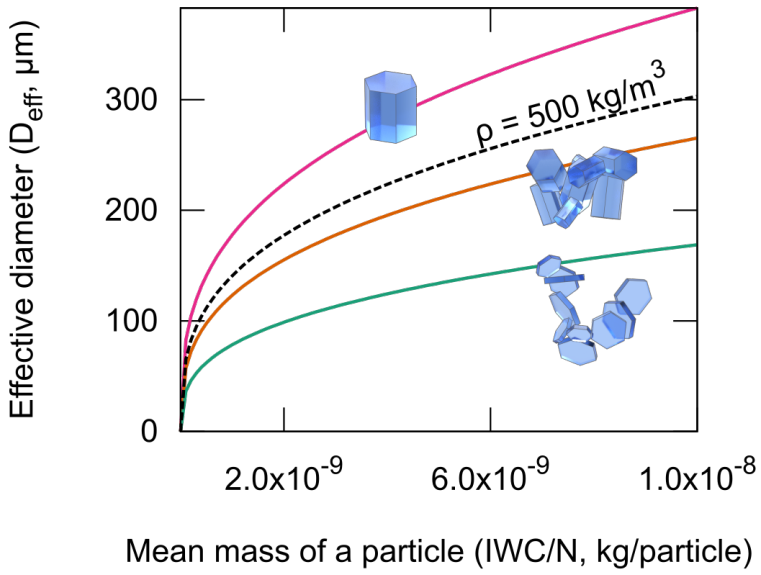

Fig. 1.2. Effective diameter computed as a function of the mean mass of a particle. The black dotted line indicates the spherical shape assumption used in the Community Atmospheric Model 5.0 (CAM 5.0). Solid lines correspond to the calculations for non-spherical particles when $\alpha = 1$.

Figure 1.2 shows that the effective diameter computed from Morrison's scheme (Eq. 1.11, black dotted line) is between effective diameter for hexagonal column and aggregate of column shapes when a gamma distribution with $\alpha = 1$ is specified. The results in Fig. 1.2 imply that Morrison's scheme implicitly assumes the particle shape as somewhat less compact particle than the hexagonal column particle, but not as bulky as aggregates.

1.3.3 GCM radiation schemes

The second stage of conversion involves the results of the light scattering calculation. Since it is computationally prohibitive to run the light scattering calculations every time for every grid box of the GCM, scattering properties of clouds are usually imbedded into the two-stream radiative transfer code (radiation scheme) as regression coefficients. The form of the regression function varies from investigator to investigator, but all of them express the following three parameters as functions of effective diameter (D_{eff}): mass extinction cross section (k_{ext}), single scattering albedo (ϖ), and asymmetry parameter (g), or, equivalently, k_{ext}, g, and mass absorption cross section (k_{abs}).

When the radiation scheme in GCM receives IWC and D_{eff} from the microphysics scheme, it first computes the values of k_{ext}, ϖ, and g corresponding to the given D_{eff} by interpolation in the look-up tables. Then, using Eq. (1.6), the radiation scheme computes the optical thickness (τ). Finally, the two-stream radiative transfer solver is executed with necessary parameters: τ, ϖ, and g (green arrow in upper right hand of Fig. 1.1).

The effects of particle shape and size distribution are incorporated into the regression coefficients in the parameterization of k_{ext}, ϖ, and g, obtained as a result of light scattering calculations. As k_{ext} asymptotically approaches $2A/(V\rho_{ice})$ for any particle shape, the effect of the variable particle shape primarily appears in ϖ and g. Grenfell and Warren (1999) conclude that a spherical particle can mimic the flux calculation for a cylindrical particle as long as the effective diameter is conserved. Their results imply that (1) In GCM radiation schemes, the effect of particle shape is small, and (2) In GCM microphysics schemes, the effect of particle shape should be taken into consideration properly.

These two implications can be derived from Eqs. (1.3), (1.6), (1.9) and (1.11). In the geometric optics limit, the two-stage conversion computes the optical thickness as follows:

$$\tau \to l\left(\frac{IWC^2}{{\rho_{eff}}^2}\frac{\pi}{N}\right)^{\frac{1}{3}}. \tag{1.12}$$

Equation (1.12) does not contain any parameterized term, and therefore, the particle shape influences the flux calculation only through ϖ and g. As Grenfell and Warren's results imply that $\varpi(D_{eff})$ and $g(D_{eff})$ are not sensitive to particle shapes, the most important parameter for the two-stage conversion is actually ρ_{eff} in GCM microphysics scheme that eventually controls τ and D_{eff}.

1.3.4 Consistency of three kinds of ice cloud models

Although the impact of assumed particle model is substantial for the satellite retrieval products (e.g. Ding et al., 2017) and flux calculation from GCM prognostics

(Eq. (1.12)), coordination of particle models used in these three groups of computer programs is still premature. A recent study by Loeb et al. (2018) performed flux estimations to show that the consistency of models used in CERES satellite retrieval and flux calculation (equivalent to GCM radiation scheme, but with higher accuracy) are needed for the precise flux retrieval.

Maintaining consistency between three kinds of cloud ice particle models is important to produce useful satellite and reanalysis products that can be compared to each other. This doctoral project therefore characterizes the ice particle shapes and surface roughness at a global scale to further the knowledge of ice cloud particles. The scope of project is outlined in the following section.

1.4 Scope of this research

This doctoral project is aimed at the inference of particle shape and surface roughness from the spaceborne polarimetric imaging sensor. This project evaluates existing roughness model, reorganizes the theory of truncation for polarimetric radiative transfer, represents the particle shapes with a few parameters, and retrieves these shape parameters from the multi-directional satellite measurements. In addition, the effect of cloud inhomogeneity and the 3-D effect are discussed with the supplementary phase function retrieval algorithm.

The scientific questions to be answered are as follows:

- What kind of ice particle habit and particle roughness can explain the radiance and the polarization state of ice cloud reflection observed with a satellite polarimeter?
- What atmospheric conditions control the distribution of inferred particle roughness?

- What are the impacts of cloud heterogeneity on inferred particle roughness?

This thesis is structured as follows. Section 2 summarizes how surface roughness is simulated in the light scattering calculations and derives analytical expression of tilt angles using the distribution theory. Section 3 reorganizes the theory of truncation and introduces the application of the δ-fit method in the radiative transfer calculation with polarization, to compare the accuracy to the widely-used δ-M method. Section 4 describes the two-stage approach that parameterizes complex particle shapes and roughness with a few parameters, enabling the application of the statistical inference in the retrieval. A semi-analytical retrieval of phase function is demonstrated in Section 5 to supplement the tropical data that are missing in Section 4. A brief summary is given in Section 6.

2 SURFACE ROUGHNESS SIMULATIONS

2.1 Introduction

Particles in ice clouds have diverse highly nonspherical shapes (Heymsfield and Iaquinta, 2000; Heymsfield, et al., 2002; Heymsfield et al., 2013; Lawson et al., 2006). Laboratory experiments reveal that the distributions of particle shapes vary with the ambient temperature and degree of supersaturation in clouds (Nakaya, 1951, Kobayashi, 1957; Bailey and Hallett, 2002, 2004). Bailey and Hallett (2009) compiled a habit diagram for natural clouds, combining recent results from aircraft measurements and laboratory experiments, whereas Kikuchi et al. (2013) proposed a comprehensive classification of ice particles and snowflakes based on surface field measurements.

Light scattering calculations show that imperfections of cloud particles such as surface roughness, inclusion of air bubbles, and crystal distortion result in the similarly featureless phase function and reduced asymmetry parameter. Surface roughness is therefore a convenient tool to mimic the various imperfections of ice crystals in natural clouds with a small number of parameter. The surface texture of actual particles is measured quantitatively by Neshyba et al. (2013) and Butterfield et al. (2017).

Surface roughness of an ice particle is simulated by two ways in light scattering calculations. The first approach, the explicit method, represents particle surfaces with triangular polygons and explicitly specifies the roughening. This approach is applicable to any light scattering calculation technique that can handle an arbitrary shape. While the implementation is simple, the computational burden is significant. The second approach

is to apply a random process on the interface of an undistorted particle. This approach is implemented as the surface tilt method and beam tilt method in ray-tracing calculations. Yang et al. (2008) confirmed that the surface tilt method is a good approximation of the explicit method in 2-D ray-tracing calculations.

Few studies have compared various implementations of roughness. A recent study by Geogdzhayev and van Diedenhoven (2016) used Macke's geometric optics computer program (Macke et al., 1996) to compare the effects of varying shape the parameter of a Weibull distribution on the phase function. There is confusion regarding the numerical implementation of surface roughness and the behavior of the asymmetry parameter when roughness is large. In the rest of this section, I characterize the existing distribution models of tilt angle and tilt methods. Section 2.2 describes the statistical representation of common tilt angle distributions, and Section 2.3 describes the difference between surface and beam tilt methods. In Section 2.4, results from light scattering calculations are provided with a focus on the asymmetry parameter. A brief summary is given in Section 2.5.

2.2 Statistical representation of tilt angle

Both surface tilt and beam tilt methods modify the interaction of a ray with particle interfaces at every reflection/refraction event in the ray-tracing calculation. The surface tilt method changes the direction of the surface normal vector, while the beam tilt method changes the beam direction. A random number generator is used to produce two random numbers that characterize the modulation: tilt angle θ and tilt direction ϕ. Once θ and ϕ are determined, the new vector is determined by the following relation:

$$\vec{k} = \begin{pmatrix} \sin\theta\cos\phi \\ \sin\theta\sin\phi \\ \cos\theta \end{pmatrix}, \tag{2.1}$$

where the z-axis is taken along the original vector, and the x-axis is taken in the plane containing the incident direction and surface normal vectors. As most methods take a uniform distribution for ϕ in current frameworks, a greater interest is in the distribution of θ.

Since the slope of the tilt is given by $s = \tan\theta$, the relation between the slope and tilt angle is as follows:

$$s = \sqrt{\frac{1}{\cos^2\theta} - 1}. \tag{2.2}$$

In general, a random variable X can be characterized by the probability density function (PDF, $f_X(x)$) and cumulative distribution function (CDF, $F_X(x)$). The CDF $F_X(x)$ is defined as the probability of obtaining a value less than or equal to x as follows:

$$F_X(x) = P(X \leq x), \tag{2.3}$$

and when the distribution is differentiable, the PDF is given by

$$f_X(x) = \frac{d}{dx} F_X(x). \tag{2.4}$$

Applying these general relations (Eqs. (2.3) and (2.4)) to a random sampling of slope s from random variable S, the CDF and PDF of the tilt angle can be written as follows:

$$F_\theta(\theta) = F_S(\tan\theta), \text{ and} \tag{2.5}$$

$$f_\theta(\theta) = \frac{1}{\cos^2\theta} f_S(\tan\theta). \tag{2.6}$$

In the following parts of this section, I introduce four distributions models of tilt angles. To simplify the expression, distributions are defined for slope s with CDF $F_S(s)$ and PDF $f_S(s)$. Figure 2.1 shows the distribution of tilt angles for the four distributions described below. As a roughness parameter, $\sigma^2 = 0.5$ is selected, and as a distortion parameter, $\alpha = 0.5$ is selected.

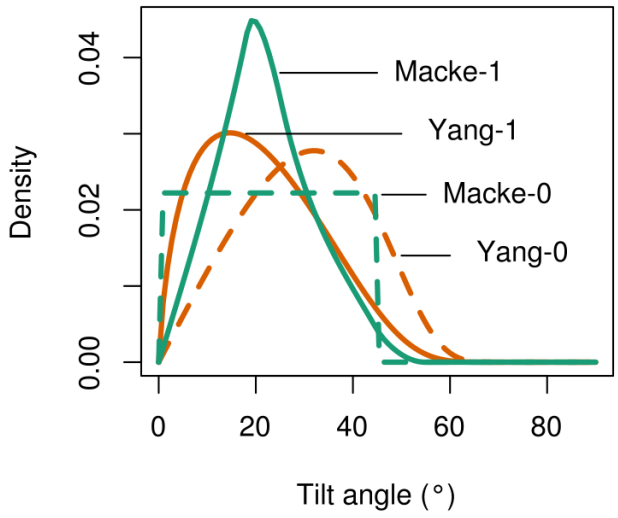

Fig. 2.1. Probability density function of four tilt angle distributions.

2.2.1 Yang-0 distribution

Yang and Liou (1998) used the 2-D Gaussian distribution to represent the distribution of slope. The PDF of slope in x and y directions are given by the 2-D probability density function used by Cox and Munk (1954) to characterize the rough ocean surface as follows:

$$f_{S_x,S_y}(s_x, s_y) = \frac{1}{\pi\sigma^2} e^{-\left(\frac{s_x^2+s_y^2}{\sigma^2}\right)}. \tag{2.7}$$

where S_x and S_y are random variables, s_x is the sampled slope in the x direction, s_y is the sampled slope in the y direction, and σ^2 is an arbitrary parameter called the "roughness parameter". The implication of this distribution is that random variables S_x and S_y follow an identical normal distribution $N(0, \sigma^2)$ independently.

Using the Box-Muller transform (Box and Muller, 1958), two random variables S_x and S_y can be generated from two random variables U_1 and U_2 following a uniform distribution between 0 and 1:

$$S_x = \sqrt{\sigma^2/2}\sqrt{-2\ln U_1}\cos(2\pi U_2), \tag{2.8}$$

$$S_y = \sqrt{\sigma^2/2}\sqrt{-2\ln U_1}\sin(2\pi U_2). \tag{2.9}$$

Since the local slope can be written as $s = \sqrt{{s_x}^2 + {s_y}^2}$, the random variable from which the local slope can be sampled is as follows:

$$S_{Y0} = \sigma\sqrt{-\ln U_1}. \tag{2.10}$$

The PDF of the slope distribution is derived step-by-step below. The probability of the event that the slope is less than an arbitrary number s is written as

$$P(S_{Y0} \le s) = P\left(\sigma\sqrt{-\ln U_1} \le s\right). \tag{2.11}$$

By using the identity of inequalities, the probability is:

$$P(S_{Y0} \le s) = P\left(U_1 \ge e^{-\left(\frac{s}{\sigma}\right)^2}\right) = 1 - P\left(U_1 \le e^{-\left(\frac{s}{\sigma}\right)^2}\right). \tag{2.12}$$

As U_1 is a random variable following a uniform distribution between 0 and 1,

$$P\left(U_1 \le e^{-\left(\frac{s}{\sigma}\right)^2}\right) = e^{-\left(\frac{s}{\sigma}\right)^2}, \tag{2.13}$$

and the CDF of S_0 is as follows:

$$F_{S_{Y0}}(s) = P(S_{Y0} \le s) = \begin{cases} 0, & s < 0 \\ 1 - e^{-\left(\frac{s}{\sigma}\right)^2}, & s \ge 0 \end{cases}, \tag{2.14}$$

The PDF of S_{Y0} is the derivative of $F_{S_{Y0}}(s)$ with respect to s.

$$f_{S_{Y0}}(s) = \frac{dF_{S_{Y0}}}{ds} = \begin{cases} 0, & s < 0 \\ \frac{2s}{\sigma^2} e^{-\left(\frac{s}{\sigma}\right)^2}, & s \ge 0 \end{cases} \tag{2.15}$$

Note that the distribution of local slope does not follow a normal distribution as a result of the convolution of two normal distributions.

2.2.2 Yang-1 distribution

The Improved Geometric Optics Method (IGOM) computer program has an alternative mode to specify a roughness. In this dissertation, I refer to this distribution as Yang-1 distribution. When this mode is selected, the IGOM code subsamples the roughness parameter between the specified roughness parameter and 0. The slope s is a sample from the random variable S_{Y1} defined as follows:

$$S_{Y1} = \sigma\sqrt{-U_2 \ln U_1} = S_{Y0}V, \tag{2.16}$$

where $V = \sqrt{U_2}$. The PDF of S_1 is obtained by computing the integral:

$$f_{S_{Y1}}(s) = \int_{-\infty}^{\infty} f_{S_{Y0}}(t) f_V\left(\frac{s}{t}\right)\frac{1}{t}dt. \tag{2.17}$$

To compute $f_{S_{Y_1}}(s)$, the PDF of V is obtained first in a similar manner to the derivation of $f_{S_{Y_0}}$. The probability of the event that V is less than or equal to an arbitrary number v is given by

$$P(V \leq v) = P(U_2 \leq v^2) = v^2, \tag{2.18}$$

and the CDF of V is written as

$$F_V(v) = P(V \leq v) = \begin{cases} 0, & v < 0 \\ v^2, & 0 \leq v < 1. \\ 1, & 1 \leq v \end{cases} \tag{2.19}$$

The PDF $f_V(v)$ is the derivative of this function, i.e.

$$f_V(v) = \frac{dF_V}{dv} = \begin{cases} 2v, & 0 \leq v < 1 \\ 0, & \text{otherwise} \end{cases}. \tag{2.20}$$

Therefore, the PDF of the product is given by

$$f_{S_{Y_1}}(s) = \int_z^\infty \frac{2x}{\sigma^2} e^{-\left(\frac{x}{\sigma}\right)^2} \frac{2s}{x} \frac{1}{x} dx. \tag{2.21}$$

Taking $t = (x/\sigma)^2$, the upper end of the integral remains the same while the lower end of the integral becomes $(z/\sigma)^2$. By using the relation

$$dt = \frac{2x}{\sigma^2} dx, \tag{2.22}$$

the integral can be written as:

$$f_{S_{Y_1}}(s) = \frac{2s}{\sigma^2} \int_s^\infty \frac{1}{t} e^{-t}\, dt. \tag{2.23}$$

The integral on the right hand side cannot be expressed with elementary functions, and is called a E_1 function. It is one kind of exponential integral:

$$f_{S_{Y_1}}(s) = \frac{2s}{\sigma^2} E_1\left(\frac{s^2}{\sigma^2}\right). \tag{2.24}$$

As exponential integrals satisfy the relation $\frac{d}{dx}E_n(x) = -E_{n-1}(x)$, the CDF can be computed by integrating Eq. (2.22) as follows:

$$f_{S_{Y_1}}(s) = 1 - E_2\left(\frac{s^2}{\sigma^2}\right). \tag{2.25}$$

2.2.3 Macke-0 distribution

Macke et al. (1996) apply the roughness based on uniform sampling of tilt angles between 0 and 90α degrees, where α is defined as a distortion parameter. I refer to this distribution as the Macke-0 distribution in this thesis. The random variable S_{M0} from which the slope is sampled is defined as

$$S_{M0} = \tan\frac{\pi}{2}\alpha\, U_1, \tag{2.26}$$

where U_1 is the random variable following a uniform distribution between 0 and 1, and the CDF can be written as follows:

$$F_{S_{M0}}(s) = P(S_{M0} < s) = P\left(\tan\frac{\pi}{2}\alpha U_1 \le s\right). \tag{2.27}$$

Thus, the final CDF and PDF are:

$$F_{S_{M0}}(s) = \begin{cases} \frac{2}{\alpha\pi}\tan s & 0 \le s < \tan\frac{\alpha\pi}{2} \\ 0 & s < 0 \end{cases}, \text{ and} \tag{2.28}$$

$$f_{S_{M0}}(s) = \begin{cases} \frac{2}{\alpha\pi}\frac{1}{1+s^2} & 0 \le s < \tan\frac{\alpha\pi}{2} \\ 0 & s < 0 \end{cases}. \tag{2.29}$$

2.2.4 Macke-1 distribution

The geometric optics computer program by Macke et al. (1996) is publicly available from the web site: http://tools.tropos.de/. In the downloaded computer program, the slope is computed in a different way from the description in Section 2.2.3. I refer to the resultant distribution as Macke-1 distribution. As the Macke-1 distribution depends on the incident direction of the beam to the interface, it is not possible to analytically derive the PDF and CDF for complex particle shapes. However, an approximate distribution can be obtained by assuming that the direction of the beam is fixed to the positive z direction. Figure 2.2 shows the PDF of Macke-1 distributions assuming fixed (positive z) incident direction (solid line, analytical function) and completely random direction (histogram bars, Monte Carlo simulation).

The analytical CDF for the Macke-1 distribution with the fixed incident direction $(0,0,1)$ is as follows:

$$F_{S_{M1}}(s) = \begin{cases} 0 & x_A \le 0 \quad \text{and} \quad x_B \le 0 \\ F_1(s) & 0 < x_A \le \frac{1}{2} \quad \text{and} \quad 0 < x_B \le \frac{1}{2} \\ F_2(s) & 0 < x_A \le \frac{1}{2} \quad \text{and} \quad \frac{1}{2} < x_B \le \frac{1}{\sqrt{2}} \\ F_3(s) & 0 < x_A \le \frac{1}{2} \quad \text{and} \quad \frac{1}{\sqrt{2}} < x_B \\ F_4(s) & \frac{1}{2} < x_A \le \frac{1}{\sqrt{2}} \quad \text{and} \quad \frac{1}{2} < x_B \le \frac{1}{\sqrt{2}} \\ F_5(s) & \frac{1}{2} < x_A \le \frac{1}{\sqrt{2}} \quad \text{and} \quad \frac{1}{\sqrt{2}} < x_B \\ 1 & \frac{1}{\sqrt{2}} < x_A \quad \text{and} \quad \frac{1}{\sqrt{2}} < x_B, \end{cases} \tag{2.30}$$

where

$$x_A = \beta s, \tag{2.31}$$

$$x_B = (\beta + 1)s, \text{ and} \tag{2.32}$$

$$\beta = \frac{1}{2}\left(\frac{1}{\alpha} - 1\right). \tag{2.33}$$

Functions $F_1(s)$ ... $F_5(s)$ are defined as follows. For the detailed derivation, readers are referred to Appendix A.

$$F_1(s) = I_{A1} = \frac{1}{3}[(\beta + 1)^3 - \beta^3]\pi s^2 \tag{2.34}$$

$$\begin{aligned} F_2(s) = &-\frac{\pi}{3}{x_A}^2\beta + \frac{2}{3}{x_B}^2(\beta + 1)[\phi(x_B) + 2\cos\phi(x_B)] \\ &-\frac{1}{6s}\ln(2x_B + 2{x_B}^2\cos\phi(x_B)) \end{aligned} \tag{2.35}$$

$$F_3(s) = (\beta + 1) - \frac{\pi}{3}\beta{x_A}^2 - \frac{1}{s}\left[\frac{1}{3\sqrt{2}} + \frac{1}{6}\ln\left(\sqrt{2} - 1\right)\right] \tag{2.36}$$

$$\begin{aligned} F_4(s) = &\frac{2}{3}{x_B}^2(\beta + 1)(\phi(x_B) + 2\cos\phi(x_B)) \\ &-\frac{2}{3}{x_A}^2\beta(\phi(x_A) + 2\cos\phi(x_A)) \\ &-\frac{1}{6s}[\ln(2x_B + 2{x_B}^2\cos\phi(x_B)) \\ &-\ln(2x_A + 2{x_A}^2\cos\phi(x_A))] \end{aligned} \tag{2.37}$$

$$\begin{aligned} F_5(s) = &\frac{1}{3}(\beta + 1) - \frac{2}{3}{x_A}^2\beta(\phi(x_A) + 2\cos\phi(x_A)) \\ &-\frac{1}{6s}\left[\ln\left(\sqrt{2} + 1\right) - \ln(2x_A + 2{x_A}^2\cos\phi(x_A))\right], \end{aligned} \tag{2.38}$$

and similarly, the PDF is as follows:

$$f_{S_{M1}}(s) = \begin{cases} 0 & x_A \le 0 \quad \text{and} \quad x_B \le 0 \\ f_1(s) & 0 < x_A \le \frac{1}{2} \quad \text{and} \quad 0 < x_B \le \frac{1}{2} \\ f_2(s) & 0 < x_A \le \frac{1}{2} \quad \text{and} \quad \frac{1}{2} < x_B \le \frac{1}{\sqrt{2}} \\ f_3(s) & 0 < x_A \le \frac{1}{2} \quad \text{and} \quad \frac{1}{\sqrt{2}} < x_B \\ f_4(s) & \frac{1}{2} < x_A \le \frac{1}{\sqrt{2}} \quad \text{and} \quad \frac{1}{2} < x_B \le \frac{1}{\sqrt{2}} \\ f_5(s) & \frac{1}{2} < x_A \le \frac{1}{\sqrt{2}} \quad \text{and} \quad \frac{1}{\sqrt{2}} < x_B \\ 0 & \frac{1}{\sqrt{2}} < x_A \quad \text{and} \quad \frac{1}{\sqrt{2}} < x_B, \end{cases} \tag{2.39}$$

where

$$f_1(s) = \frac{2}{3}[(\beta+1)^3 - \beta^3]\pi s \tag{2.40}$$

$$f_2(s) = -\frac{2\pi}{3}x_A\beta^2 + \frac{4}{3}x_B(\beta+1)^2\left[\phi(x_B) + \frac{1}{2}\cos\phi(x_B)\right] + \frac{1}{6s^2}\ln(2x_B + 2{x_B}^2\cos\phi(x_B)) \tag{2.41}$$

$$f_3(s) = -\frac{2\pi}{3}\beta^2 x_A + \frac{1}{s^2}\left[\frac{1}{3\sqrt{2}} + \frac{1}{6}\ln\left(\sqrt{2}-1\right)\right] \tag{2.42}$$

$$f_4(s) = \frac{4}{3}\left[x_B(\beta+1)^2\left(\phi(x_B) + \frac{1}{2}\cos\phi(x_B)\right) - x_A\beta^2\left(\phi(x_A) + \frac{1}{2}\cos\phi(x_A)\right)\right] + \frac{1}{6s^2}[\ln(2x_B + 2{x_B}^2\cos\phi(x_B)) - \ln(2x_A + 2{x_A}^2\cos\phi(x_A))] \tag{2.43}$$

$$f_5(s) = \frac{\sqrt{2}}{3}(\beta+1)^2 - \frac{4}{3}x_A\beta^2\left(\phi(x_A) + \frac{1}{2}\cos\phi(x_A)\right) + \frac{1}{6s^2}\left[\ln\left(\sqrt{2}+1\right) - \ln(2x_A + 2{x_A}^2\cos\phi(x_A))\right]. \quad (2.44)$$

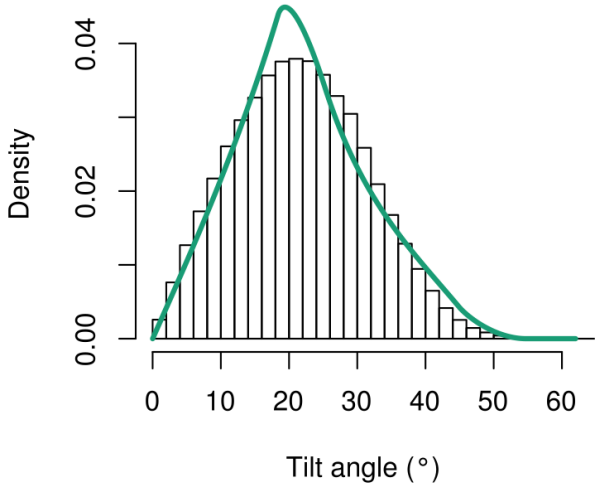

Fig. 2.2. The probability density function for Macke-1 distribution. Green line is simulation by the analytical expression for a fixed (positive z) incident direction (line) and the result from the Monte Carlo simulation assuming random incident direction.

2.3 Surface tilt and beam tilt

The tilt angle distributions described in the previous section determine the original "raw" distribution of θ and ϕ, but it is not the actual distribution of θ used in light scattering calculations. This is because some combinations of tilt angle, tilt azimuth direction, and incident beam direction are unphysical, and the light scattering program computes θ and ϕ with a new realization until a physically possible combination is

obtained. This process is significantly affected by the rejection criteria that depend on tilt methods.

As briefly described in Section 2.2, the surface tilt method changes the direction of the surface normal, and the beam tilt method changes the direction of the ray-tracing beam. Figure 2.3 shows the schematics of the two tilt methods. The surface normal vector is $\vec{n}$, the direction of the incident ray is $\overrightarrow{k_0}$, the direction of the reflected ray is $\overrightarrow{k_l}$, and the direction of the refracted ray is $\overrightarrow{k_r}$. In Fig. 2.3, primes indicate that the vector is modified by the surface or beam tilt method.

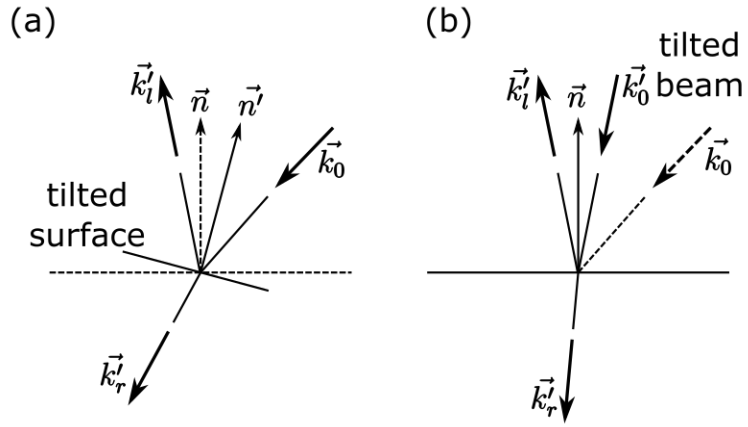

Fig. 2.3. Schematics of (a) surface tilt method and (b) beam tilt method.

2.3.1 Surface tilt method

The surface tilt method requires two rejection criteria: (a) direction of incident beam, and (b) direction of reflected beam. Criterion (a) is straightforward. When the incident direction makes a small angle to the interface, the surface may tilt more than the

angle between the incident direction and interface as shown in Fig. 2.4 (a). The incident direction $\overrightarrow{k_0}$ is invalid because the beam looks like it is coming from the other side of the interface. The second criterion (b) requires the reflected ray to leave the particle and not to propagate into the particle. This situation happens when the incident direction $\overrightarrow{k_0}$ is close to the tilted interface as shown in Fig. 2.4 (b). As a result of these two rejection criteria, the distribution of tilt angle (θ) and the tilt azimuth angle (ϕ) changes from the original distribution as shown in Fig. 2.5. When the roughness is large, the surface tilt method prefers a backward direction and it implies that the external reflection (first reflection when a ray enters a particle) decreases and a larger intensity of rays propagates into the particle.

2.3.2 Beam tilt method

The beam tilt method requires only one criterion for the rejection, (a) direction of the incident beam. The criterion is the same as for the surface tilt method and Fig. 2.6 illustrates an example of a rejected tilt configuration. Figure 2.7 shows the distribution of θ and ϕ for the same three degrees of surface roughness σ^2 as in Fig. 2.5. As the rejection criterion is less restrictive, the distributions are closer to the original distribution than the for the surface tilt method.

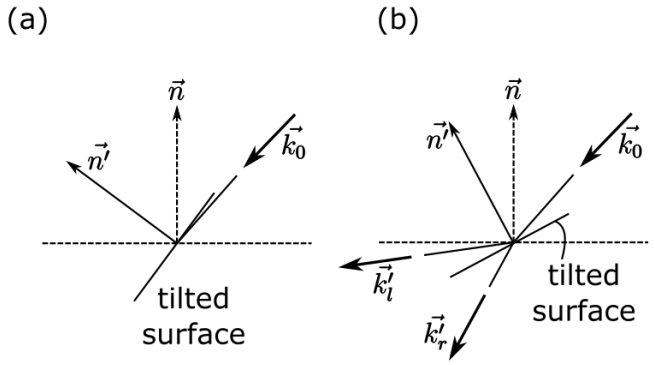

Fig. 2.4. Examples of rejected geometric configurations for the surface tilt method. (a) The direction of incident beam $\vec{k}_0$ is from the other side of interface. (b) The reflected beam $\vec{k}_t'$ enters into the particle (c.f. downward to the original surface).

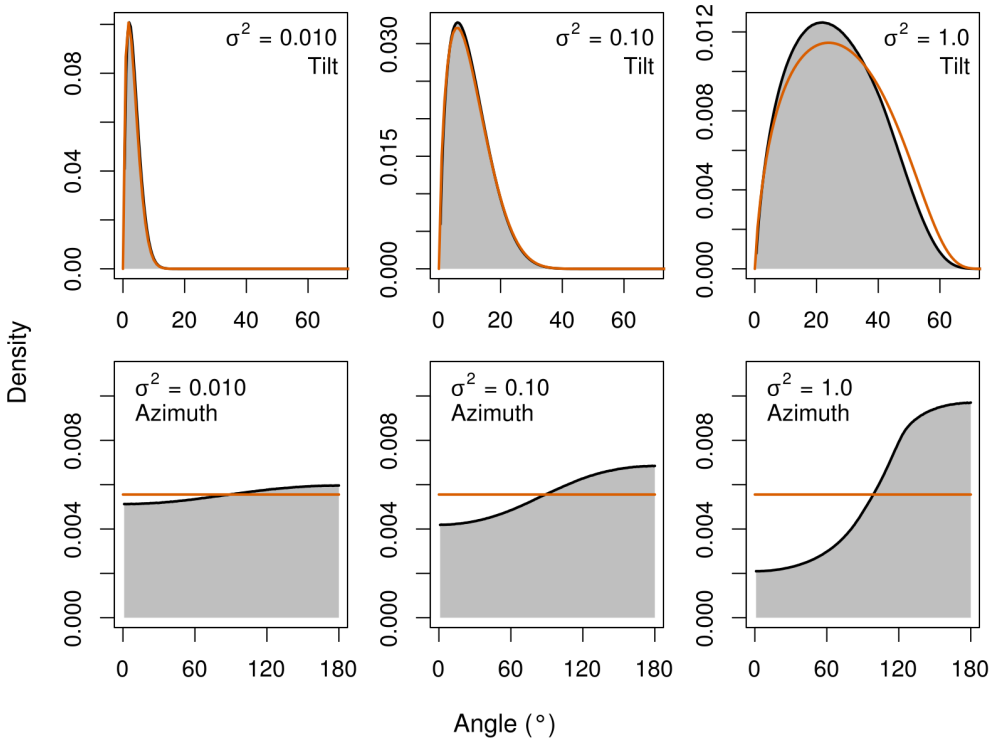

Fig. 2.5. Distribution of original and accepted tilt and azimuth angles for the surface tilt method. Columns correspond to three degrees of surface roughness. The grey shading indicates the results from IGOM calculations and the orange line is the original distribution (Yang-1).

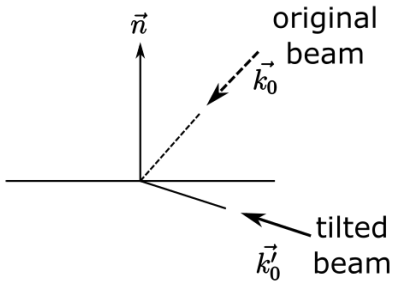

Fig. 2.6. An example of rejected geometric configurations for the beam tilt method. The direction of the incident beam is from the other side of interface.

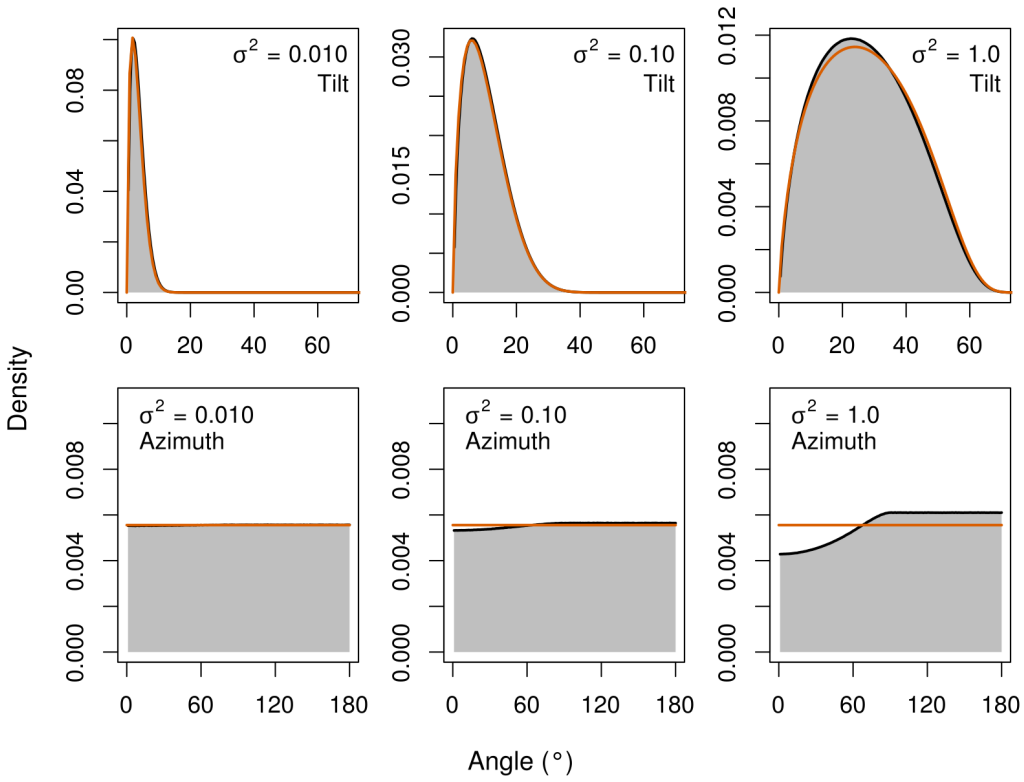

Fig. 2.7. Distribution of original and accepted tilt and azimuth angles for the beam tilt method. Columns correspond to three degrees of surface roughness. The grey shading indicates the results from IGOM calculations and the orange line is the original distribution (Yang-1).

Besides the difference in rejection criteria, the beam tilt method has an uncertainty related to the polarization state of the light. The polarization state of light is related to the phase and direction of the electric vector. With the surface tilt method, a straightforward sequential application of the Fresnel formula simulates a chain of reflection/refraction events. Between two reflection/refraction events, the direction and magnitude of the electric vector are conserved. However, the beam tilt method cannot conserve the direction of the electric vector because the direction of propagation changes. This is especially true when the tilt angle is large.

2.4 Single scattering properties

To elucidate the differences caused by the tilt distributions and tilt techniques, light scattering calculations are performed for a hexagonal column particle using the improved geometric optics (IGOM, Yang and Liou 1996) method and Invariant-Imbedded T-Matrix (IITM) method (Bi and Yang, 2014). The calculations are performed for 198 particle sizes ranging from $D_{max} = 2$ μm to 10000 μm, and the results are averaged over the gamma particle size distribution (shape parameter $\alpha = 8$, scale parameter $\beta = 4.538$). The effective diameter of the particle is $D_{eff} = 60$ μm, and the size distribution (weighted by geometric cross section) is shown in Fig. 2.8. For sizes smaller than $D_{max} = 10.6$ μm, scattering properties are computed with the IITM method, and results from the IGOM and IITM methods are merged by the method described by Yang et al. (2013). Since the particle size distribution is almost completely weighted with $D_{max} > 11.2$ μm, the results can be considered to be the results by IGOM calculations.

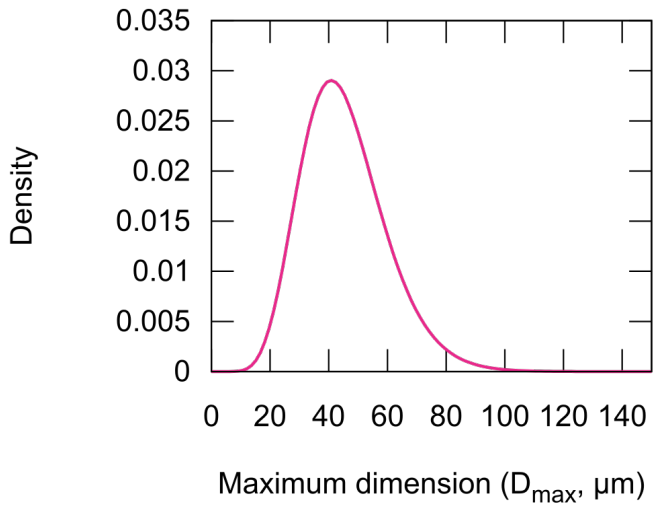

Fig. 2.8. Projection-area weighted gamma distribution. The distribution is plotted as a function of maximum dimension (D_{max}). The shape parameter is $\alpha = 8$, and scale parameter is $\beta = 4.538$.

Figure 2.9 shows the asymmetry parameter as a function of roughness parameter (σ^2) or distortion parameter (α). With Yang-0 and Yang-1 distributions (Fig. 2.9a), the asymmetry parameter has a peak at $\sigma^2 = 10^{-5}$ to 10^{-4}, while in Fig. 2.9 (b), with Macke-0 and Macke-1 distributions, the peaks are near $\alpha = 7{\times}10^{-3}$. These peaks are presumably because of the way IGOM handles the near-forward scattering. In the phase matrix calculation, the intensity in scattering angle less than $\Theta < 0.1146°$ is applied with a diffraction phase function instead of a ray-tracing phase function. With the current version of IGOM code, it is therefore recommended to use $\sigma^2 > 0.001$ and $\alpha > 0.05$. Nonetheless, the location of the peak is a good indicator for the deflection of rays from the original direction, and therefore the effective direction of surface

roughness. Although the shapes of Macke-0 and Macke-1 distributions are different, the asymmetry parameter calculations surprisingly agree with each other.

Figure 2.10 illustrates the effect of the tilt method on the asymmetry parameter. The results indicate that the beam tilt method reaches the peak at a smaller roughness or distortion parameter. This is because the beam tilt method is less restrictive in the rejection criteria described in Section 2.3, and the effective slope distribution tends to be biased low. In addition to the difference of the peak locations, the behavior of the asymmetry parameter at large roughness is different between surface and beam tilt methods. The asymmetry parameter (g) computed with the surface tilt method increases when the roughness reaches about $\sigma^2 = 0.1$ or $\alpha = 0.3$, but g from the beam tilt method continues to decrease. A hypothesis to explain this difference is related to the difference of effective tilt azimuth direction. The surface tilt method prefers azimuth angle $\phi < 90°$ more strongly than the beam tilt method because of the restrictive rejection criteria as discussed in Section 2.3. Such a strong preference for scattering into the backward hemisphere increases the chance of a ray to enter the particle with a small specular reflection and to exit the particle without total reflection. The consequence is that scattering into the forward hemisphere increases, and the asymmetry parameter also increases.

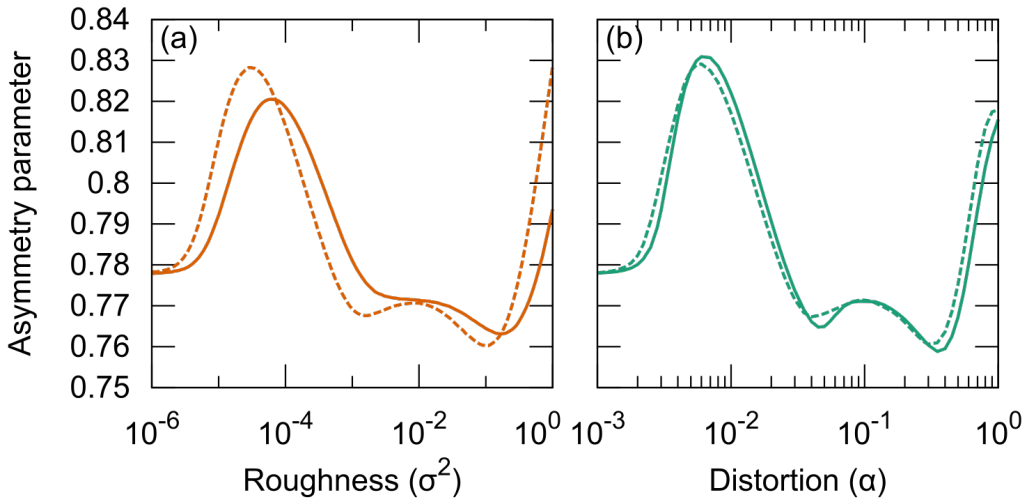

Fig. 2.9. Asymmetry parameter of a single hexagonal column particle. The aspect ratio is fixed at $AR = 1$ (diameter of basal face is equal to length of column) and the surface tilt method is used. (a) For Yang-0 distribution (dotted line) and Yang-1 distribution (solid line). (b) For Macke-0 distribution (dotted line) and Macke-1 distribution (solid line).

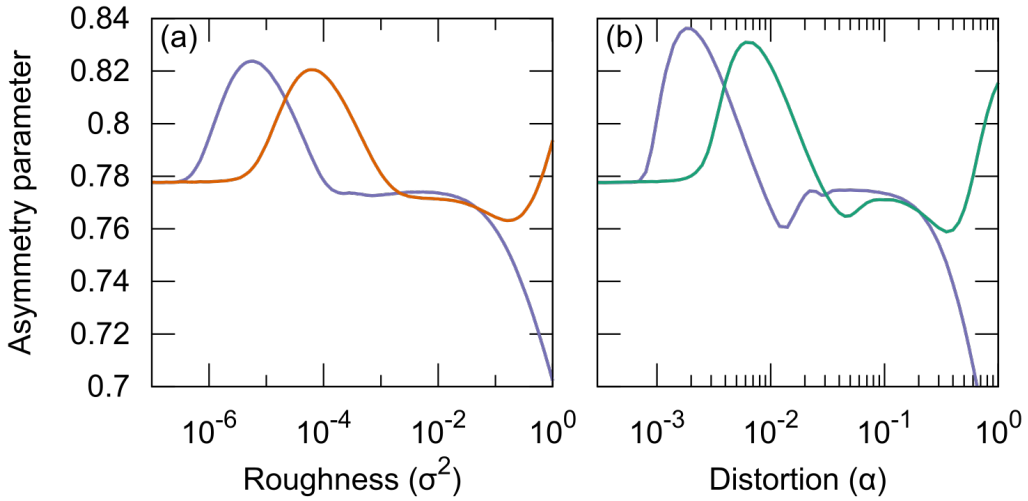

Fig. 2.10. Asymmetry parameter comparison between surface and beam tilt methods. The same hexagonal column as in Fig. 2.9 is used. (a) For Yang-1 distribution with the surface tilt method (orange solid line) and with the beam tilt method (purple line). (b) For Macke-1 distribution with the surface tilt method (green line) and the beam tilt method (purple line).

2.5 Summary

In this section, four common distributions models of surface roughening are described, and their corresponding probability density functions and cumulative distribution functions are derived. The rejection criteria used in the light scattering calculations are compared between the beam tilt and surface tilt methods to examine the difference and effect on the asymmetry parameter calculations. From the locations of spurious asymmetry parameter peaks that are related to the transition from forward scattering to side scattering, it is shown that the Yang-0 distribution reaches the asymmetry parameter peak at smaller roughness parameter σ^2 than the Yang-1 distribution, while the difference between Macke-0 and Macke-1 distributions is small. As roughness increases to a severe level, the asymmetry parameter shows the decreasing trend with the beam tilt method, but an increasing trend with the surface tilt method. In the following part of the dissertation, the surface tilt method with Yang-1 distribution is used to compute the single scattering properties. The surface tilt method does not suffer from the polarization uncertainty due to the unphysical rotation of the electric vector that is associated with the beam tilt method. Yang-1 distribution is selected because it is used to produce the widely-used database by Yang et al. (2013).

3 TRUNCATION OF PHASE MATRIX*

For an accurate ice cloud polarized reflectance calculation, a strong phase function peak in the forward direction requires special treatment. There are two popular truncation techniques (δ-M method and δ-fit method) for intensity-only calculations, but the application of the δ-fit method is limited. This section describes the theory of truncation and derives the δ-fit method for polarized radiative transfer. The results of reflectivity and transmissivity calculations are presented using these two techniques.

3.1. Introduction

In the application of vector radiative transfer solvers to simulate, for example, ice cloud reflectivity and transmissivity, the presence of large particles triggers a trade-off between the accuracy and speed of the simulation. The scattering properties of such large particles cannot be appropriately represented for the radiance simulation with an affordable directional resolution (number of streams). Anisotropic scattering in a planetary atmosphere has been a major challenge, and Sobolev (1975) discusses multiple methods of approximation for highly anisotropic scattering problems. Current common practice is to adapt a truncation technique to minimize error due to the reduced directional resolution used in the numerical radiative transfer simulations.

The δ-fit method developed by Hu et al. (2000) fits the scattering phase function with a limited number of Legendre polynomials to accurately simulate the radiance. The

* Edited and reprinted with permission from "Truncation of the scattering phase matrix for vector radiative transfer simulation" by Souichiro Hioki, Ping Yang, George W. Kattawar, and Yongxiang Hu, 2016. J. Quant. Spectrosc. Radiat. Transf., 183, 70-77. Copyright [2016] by Elsevier.

method contrasts with the δ-M method developed by Wiscombe (1977), which focuses on accurate flux simulation. Each method starts with the following plane-parallel radiative transfer equation:

$$-\mu\frac{\partial I}{\partial \tau} = -I(\tau,\mu,\phi) + \frac{\varpi(\tau)}{4\pi}\int_{-1}^{1} d\mu' \int_{0}^{2\pi} \mathcal{P}(\tau,\cos\Theta) I(\tau,\mu',\phi')\, d\phi' + (1-\varpi)B(T), \tag{3.1}$$

where τ is optical thickness measured from the top of the atmosphere, μ is the cosine of the zenith angle, ϕ is the azimuth angle, $I(\tau,\mu,\phi)$ is the radiance propagating along the direction (μ,ϕ), ϖ is the single scattering albedo, $\mathcal{P}(\cos\Theta)$ is the phase function value at scattering angle Θ, and $B(T)$ is the blackbody emission at the local temperature T.

Each method uses the following similarity transformation, which defines scaled variables with an arbitrary factor f in the form:

$$\tau^* = (1-f\varpi)\tau, \tag{3.2}$$

$$\varpi^* = \frac{1-f}{1-f\varpi}\varpi, \tag{3.3}$$

$$\mathcal{P}^*(\cos(\Theta)) = \frac{1}{1-f}[\mathcal{P}(\cos\Theta) - 4\pi f\delta(1-\cos\Theta)], \tag{3.4}$$

where $\delta(1-\cos\Theta)$ is the Dirac delta function peaked in the forward scattering direction. Substituting Eqs. (3.2)-(3.4) into Eq. (3.1) yields the same form for the radiative transfer equation but now for the scaled quantities indicated by the asterisk symbol; namely,

$$-\mu\frac{\partial I}{\partial \tau^*} = -I(\tau^*,\mu,\phi) + \frac{\varpi^*(\tau^*)}{4\pi}\int_{-1}^{1} d\mu' \int_{0}^{2\pi} \mathcal{P}^*(\tau^*,\cos\Theta) I(\tau^*,\mu',\phi')\, d\phi' + (1-\varpi^*)B(T). \tag{3.5}$$

In the classic approach (e.g. Potter, 1970), the original phase function $\mathcal{P}(\cos\Theta)$ is approximated by the sum of a delta function and a phase function without a forward peak $\mathcal{P}^*_{trunc}(\cos\Theta)$.

$$\mathcal{P}(\cos\Theta) \approx (1-f)\mathcal{P}^*_{trunc}(\cos(\Theta)) + 4\pi f\delta(1-\cos\Theta), \tag{3.6}$$

and the similarity transformation is derived as a consequence of the approximation. Eqs. (3.2)-(3.4) define an approximate radiative transfer problem in the classic approach.

However, the similarity transformation itself is mathematically exact (Mckellar and Box, 1981; Mitrescu and Stephens, 2004) and it is beneficial for our discussion to accept the exact similarity transformation to unambiguously derive the vectorized form of the δ-fit method. Specifically, we interpret Eqs. (3.2)-(3.4) as definitions of scaled quantities τ^*, ϖ^*, and $\mathcal{P}^*(\cos(\Theta))$ without approximations. When Eqs. (3.2)-(3.4) are strictly satisfied, the solution of Eq. (3.5) gives an exact solution of the original radiative transfer equation Eq. (3.1).

By accepting the exact similarity transformation, truncation techniques are seen as optimization techniques. Truncation techniques simultaneously adjust parameter f and $\mathcal{P}^*_N(\cos(\Theta))$, which is a reconstructed phase function from N coefficients (c.f. Eq. (3.14)), to reduce the error in the flux or radiance. Mitrescu and Stephens (2004) attempted a similar interpretation, showing that the parameter f depends on the

truncation method and the number of streams in addition to the original phase function. Some systematic evaluations of these truncation techniques have been reported in the literature (Rozanov and Lyapustin, 2010; Iwabuchi and Suzuki, 2009).

This section applies the framework discussed above, and interprets the δ-fit method as a correction to the source function, following the approach taken by Rozanov and Lyapustin (2010). The outcome of the theoretical development is an adaptation of the δ-fit method to vector radiative transfer. Some adjustments of the present method are provided for numerical implementation as a user-friendly computer program.

3.2 The δ-fit method

This section briefly summarizes the δ-fit method based on the original paper by Hu et al. (2000). The traditional δ-fit method starts with the expansion of the phase function in terms of Legendre polynomials $P_s(x)$,

$$\mathcal{P}(x) = \sum_{s=0}^{\infty} \alpha_1^{(s)} P_s(x), \tag{3.7}$$

where $x = \cos\Theta$ and $\alpha_1^{(s)}$ is the expansion coefficient of order s. The δ-fit method approximates this phase function with a limited number of coefficients N that are the result of fitting in the form:

$$\hat{\mathcal{P}}_N(x) = \sum_{s=0}^{N} \hat{\alpha}_1^{(s)} P_s(x), \tag{3.8}$$

where a hat indicates that the quantity is a result of fitting.

The standard least squares method is employed to minimize the sum of squared differences between 1 and the ratio of the reconstructed phase function $\hat{\mathcal{P}}_N(x)$ to the original phase function $\mathcal{P}(x)$:

$$\varepsilon = \sum_{i=1}^{m} \left(\frac{\hat{\mathcal{P}}_N(x_i)}{\mathcal{P}(x_i)} - 1 \right)^2 w_i, \tag{3.9}$$

where w_i is the step-function weight defined by the truncation angle Θ_{trc}.

$$w_i = \begin{cases} 1, & x < \cos\Theta_{trc} \\ 0, & x \geq \cos\Theta_{trc.} \end{cases} \tag{3.10}$$

Linear least square fitting based on Eq. (3.9) by singular vector decomposition yields a set of coefficients $\hat{\alpha}_1^{(s)}$. Once a set of coefficients is obtained, the similarity transformation of the radiative transfer equation is utilized to satisfy the normalization condition of the phase function. Specifically, the following scaling adjustments are applied:

$$1 - f = \hat{\alpha}_1^{(0)}, \tag{3.11}$$

$$\hat{\alpha}_1^{(s)*} = \frac{\hat{\alpha}_1^{(s)}}{1 - f}. \tag{3.12}$$

The scaling factor (truncation factor) f and fitted, scaled expansion coefficients $\hat{\alpha}_1^{(s)*}$ are used in an arbitrary solver of the scaled radiative transfer equation.

The fitting process in Eq. (3.9) can be rewritten as a linear least square fitting with weight inversely proportional to the variance in the tabulated phase function in the form:

$$\varepsilon/_{\varepsilon_1{}^2} = \sum_{i=1}^{m} \left(\hat{\mathcal{P}}_N(x_i) - \mathcal{P}(x_i)\right)^2 \frac{w_i}{(\varepsilon_1 \mathcal{P}(x_i))^2}, \tag{3.13}$$

where ε_1 is the precision of the phase function. Note that $(\varepsilon_1 \mathcal{P}(x_i))^2$ is the variance of the phase function at the ith data point. The variance is due to the numerical implementation of light scattering calculations and the numerical representation of a phase function. The precision, ε_1, is chosen as the largest value among machine precision, table precision, and the relative error in the numerical algorithm.

3.3 Source function correction by the δ-fit method

The effect of truncation is that the reconstructed phase function:

$$\mathcal{P}_N^*(x) = \sum_{s=0}^{N} \alpha_1^{(s)*} P_s(x) \tag{3.14}$$

may not fully describe the scaled phase function $\mathcal{P}^*(x)$ defined in Eq. (3.4). Note that the scaled radiative transfer equation (Eq. (3.5)) gives an exact solution only when $\mathcal{P}^*(x) = \mathcal{P}_N^*(x)$. This condition is usually not achieved because the delta function in $\mathcal{P}^*(x)$ requires an infinite number of coefficients to be fully expanded.

The error of the reconstructed phase function affects the radiative transfer equation through modifying the source function. Since the formal solution of the radiative transfer equation is an integral of the source function, the solution is affected by the error in the source function. For simplicity, we limit our discussion to cases with no emission. The untruncated source function is written as:

$$J(\tau^*, \mu, \phi) = \frac{\varpi^*}{4\pi} \int_{-1}^{1} d\mu' \int_{0}^{2\pi} \mathcal{P}^*(\cos\Theta) I(\tau^*, \mu', \phi')\, d\phi', \tag{3.15}$$

and the truncated source function is written as:

$$J_N(\tau^*, \mu, \phi) = \frac{\varpi^*}{4\pi} \int_{-1}^{1} d\mu' \int_{0}^{2\pi} \mathcal{P}_N^*(\cos\Theta) I(\tau^*, \mu', \phi')\, d\phi', \tag{3.16}$$

so the error in the source function is $J_N(\tau^*, \mu, \phi) - J(\tau^*, \mu, \phi)$. As the total radiance is a sum of direct solar radiation and diffuse radiation, the source function error can be written as the sum of two terms:

$$\begin{aligned} & J_N(\tau^*, \mu, \phi) - J(\tau^*, \mu, \phi) \\ & = \frac{\varpi^*}{4\pi} \int_{-1}^{1} d\mu' \int_{0}^{2\pi} [\mathcal{P}_N^*(\cos\Theta) - \mathcal{P}^*(\cos\Theta)] I_{dir}(\tau^*, \mu', \phi')\, d\phi' \\ & + \frac{\varpi^*}{4\pi} \int_{-1}^{1} d\mu' \int_{0}^{2\pi} \big[\mathcal{P}_N^*(\cos\Theta) I_{diff,N}(\tau^*, \mu', \phi') \\ & \qquad - \mathcal{P}^*(\cos\Theta) I_{diff}(\tau^*, \mu', \phi')\big]\, d\phi'. \end{aligned} \tag{3.17}$$

where $I_{dir}(\tau^*, \mu', \phi')$ is the direct solar radiation, $I_{diff,N}(\tau^*, \mu', \phi')$ is the diffuse radiation with the truncated phase function, and $I_{diff}(\tau^*, \mu', \phi')$ is the diffuse radiation with the untruncated phase function.

It is well known that the radiance computed with the δ-M truncation shows a significant oscillation about the true value (e.g., Fig. 3.2). This is primarily because the oscillation in the reconstructed phase function (see, Fig. 1 in Nakajima and Tanaka, 1988) propagates through the first term of Eq. (3.17) to cause the radiance error (Rozanov and Lyapustin, 2010). The oscillation mainly originates from the first term of Eq. (3.17) because the direct solar radiation $I_{dir}(\tau^*, \mu', \phi')$ is far more anisotropic than diffuse radiation $I_{diff}(\tau^*, \mu', \phi')$, which is a result of multiple scattering.

In the δ-fit method, a set of fitted coefficients $\hat{\alpha}_1^{(s)}$ that minimize the difference between the reconstructed phase function $\hat{\mathcal{P}}_N(x)$ and the original phase function $\mathcal{P}(x)$ is used after scaling. The resulting reconstructed scaled phase function $\hat{\mathcal{P}}_N^*(x)$ is close to $\mathcal{P}^*(x)$ because $\mathcal{P}(x)$ and $(1-f)\mathcal{P}^*(x)$ are identical except in the exact forward scattering direction. Specifically, we have

$$\hat{\mathcal{P}}_N^*(x) = \mathcal{P}^*(x) + \varepsilon_{fit}(x), \tag{3.18}$$

where the error of fitting $\varepsilon_{fit}(x)$ is small except between the forward scattering direction and a direction a few degrees from the specified truncation angle.

The δ-fit method minimizes the source function error by using $\hat{\mathcal{P}}_N^*(x)$, which is close to $\mathcal{P}^*(x)$. The source function error for the δ-fit method is as follows:

$$\begin{aligned} &J_{fit,N}(\tau^*,\mu,\phi) - J(\tau^*,\mu,\phi) \\ &\quad = \frac{\varpi^*}{4\pi}\int_{-1}^{1} d\mu' \int_0^{2\pi} \varepsilon_{fit}(\cos\Theta)\, I_{dir}(\tau^*,\mu',\phi')\, d\phi' \\ &\quad + \frac{\varpi^*}{4\pi}\int_{-1}^{1} d\mu' \int_0^{2\pi} \left[\hat{\mathcal{P}}_N^*(\cos\Theta) I_{diff,N}(\tau^*,\mu',\phi') \right. \\ &\quad \left. - \mathcal{P}^*(\cos\Theta) I_{diff}(\tau^*,\mu',\phi')\right] d\phi'. \end{aligned} \tag{3.19}$$

Equation (3.19) shows that the δ-fit method reduces the first term of the source function error in Eq. (3.17), and improves the accuracy of radiance computation.

Another approach to the source function correction is the TMS method (Nakajima and Tanaka, 1988). Essentially, the TMS method applies $(1-f)^{-1}\mathcal{P}(x) = \mathcal{P}^*(x) + 4\pi f(1-f)^{-1}\delta(1-\cos\ \Theta)$ for the single scattering source function and

$\hat{\mathcal{P}}_N^*(x)$ for the multiple scattering source function. As multiple scattering is less anisotropic, this approach also significantly improves the accuracy of the radiance. Rozanov and Lyapustin (2010) theoretically showed how the TMS method reduces the error. The disadvantage of the method is that a spurious delta function appears in the first-order source function, resulting in an inaccurate transmissivity. This shortcoming is corrected by the IMS method (1988) to significantly reduce the error in the transmissivity calculation.

Correction of the source term by these two approaches might not conserve the low-order moments, so these methods are not suitable for flux calculations. The δ-M method (Wiscombe, 1977) is designed to keep the lower order expansion coefficients for accurate flux computations. The contrast of the δ-fit method and the δ-M method originates from conserving different characteristics of the original phase function through truncations. The δ-fit method conserves the shape of the original phase function while the δ-M method conserves the expansion coefficients. As these two characteristics cannot be conserved simultaneously, a proper truncation technique should be selected based on the purpose.

3.4 Extending the δ-fit method in scattering matrix expansion

The vector radiative transfer equation for plane-parallel media is formulated with Stokes vector $\boldsymbol{I}(\tau, \mu, \phi)$ and phase matrix $\boldsymbol{Z}(\tau, \mu, \mu', \phi, \phi')$ as follows (Hovenier et al., 2004; de Haan et al., 1987):

$$-\mu\frac{\partial \boldsymbol{I}}{\partial \tau} = -\boldsymbol{I}(\tau,\mu,\phi) + \frac{\varpi(\tau)}{4\pi}\int_{-1}^{1} d\mu' \int_{0}^{2\pi} \boldsymbol{Z}(\tau,\mu,\mu',\phi,\phi')I(\tau,\mu',\phi')\,d\phi' + (1-\varpi)\boldsymbol{B}(T), \tag{3.20}$$

where particles and their scattering plane mirror images are randomly oriented. The similarity transformation also holds for the vector radiative transfer equation. The reader is referred to (Sanghavi and Stephens, 2015) for the derivation.

Equation (3.20) is transformed by defining scaled variables as follows.

$$\tau^* = (1 - f\varpi)\tau, \tag{3.21}$$

$$\varpi^* = \frac{1-f}{1-f\varpi}\varpi, \tag{3.22}$$

$$\boldsymbol{Z}^*(\mu,\mu',\phi,\phi') = \frac{1}{1-f}[\boldsymbol{Z}(\mu,\mu',\phi,\phi') - 4\pi f\boldsymbol{E}\delta(1-\cos\Theta)]. \tag{3.23}$$

The phase matrix $\boldsymbol{Z}(\mu,\mu',\phi,\phi')$ is related to the scattering matrix $\boldsymbol{F}(\cos\Theta)$ by

$$\boldsymbol{Z}(\mu,\mu',\phi,\phi') = \boldsymbol{L}(-\sigma_2)\boldsymbol{F}(\cos\Theta)\boldsymbol{L}(\sigma_1), \tag{3.24}$$

where $\boldsymbol{L}(-\sigma_2)$ and $\boldsymbol{L}(\sigma_1)$ are rotation matrices of the second and third elements of the Stokes vector. The matrix $\boldsymbol{E}$ is the 4×4 identity matrix. Since the second term of Eq. (3.23) appears only in the exact forward scattering direction, the rotation matrices do not modify the identity matrix. This implies that Eq. (3.23) can be written in the following form:

$$\boldsymbol{F}^*(\mu,\mu',\phi,\phi') = \frac{1}{1-f}[\boldsymbol{F}(\mu,\mu',\phi,\phi') - 4\pi f\boldsymbol{E}\delta(1-\cos\Theta)]. \tag{3.25}$$

Denoting the elements of the scattering matrix as follows:

$$\boldsymbol{F}(\cos\Theta) = \begin{pmatrix} a_1(\cos\Theta) & b_1(\cos\Theta) & 0 & 0 \\ b_1(\cos\Theta) & a_2(\cos\Theta) & 0 & 0 \\ 0 & 0 & a_3(\cos\Theta) & b_2(\cos\Theta) \\ 0 & 0 & -b_2(\cos\Theta) & a_4(\cos\Theta) \end{pmatrix}, \tag{3.26}$$

the unique elements are expanded in terms of generalized spherical functions $P_{q,r}^{(s)}(x)$:

$$a_1(x) = \sum_{s=0}^{\infty} \alpha_1^{(s)} P_{0,0}^{(s)}(x) = \sum_{s=0}^{\infty} \alpha_1^{(s)} P_s(x), \tag{3.27}$$

$$a_2(x) + a_3(x) = \sum_{s=0}^{\infty} [\alpha_2^{(s)} + \alpha_3^{(s)}] P_{2,2}^{(s)}(x), \tag{3.28}$$

$$a_2(x) - a_3(x) = \sum_{s=0}^{\infty} \left[\alpha_2^{(s)} - \alpha_3^{(s)}\right] P_{2,-2}^{(s)}(x), \tag{3.29}$$

$$a_4(x) = \sum_{s=0}^{\infty} \alpha_4^{(s)} P_{0,0}^{(s)}(x), \tag{3.30}$$

$$b_1(x) = \sum_{s=0}^{\infty} \beta_1^{(s)} P_{0,2}^{(s)}(x), \tag{3.31}$$

$$b_2(x) = \sum_{s=0}^{\infty} \beta_2^{(s)} P_{0,2}^{(s)}(x). \tag{3.32}$$

By defining $a_{\pm}(x) = a_2(x) \pm a_3(x)$ and $\alpha_{\pm}^{(s)} = \alpha_2^{(s)}(x) \pm \alpha_3^{(s)}(x)$, Eqs. (3.28) and (3.29) are written as the following:

$$a_+(x) = \sum_{s=0}^{\infty} \alpha_+^{(s)} P_{2,2}^{(s)}(x), \tag{3.33}$$

$$a_-(x) = \sum_{s=0}^{\infty} \alpha_-^{(s)} P_{2,-2}^{(s)}(x). \tag{3.34}$$

The application of the δ-fit method is based on the same principle as in the scalar version. In an analogy to Eq. (3.18), we have

$$\widehat{\boldsymbol{F}}_N^*(x) = \boldsymbol{F}^*(x) + \varepsilon_{fit}(x). \tag{3.35}$$

Similar to the scalar case, elements in the scaled scattering matrix $\boldsymbol{F}^*(x)$ are identical to the elements of the original scattering matrix $\boldsymbol{F}(x)$ times the factor $(1-f)^{-1}$ except in the exact forward direction (c.f. Eq. (3.25)). Therefore, the fitting process should minimize the differences between the original scattering matrix and the reconstructed scattering matrix, given by

$$\varepsilon_{a_p} = \sum_{i=0}^{m} \left(\frac{\hat{a}_{p,N}(x_i)}{a_p(x_i)} - 1 \right)^2 w_i \ , \tag{3.36}$$

$$\varepsilon_{b_q} = \sum_{i=0}^{m} \left(\frac{\hat{\beta}_{q,N}(x_i)}{b_q(x_i)} - 1 \right)^2 w_i \ . \tag{3.37}$$

Equation (3.36) is applied to diagonal elements ($p = 1, +, -, 4$), whereas Eq. (3.37) is applied to off-diagonal elements ($q = 1, 2$). All fittings are conducted independently, and the free parameter f is determined by the normalization constraints for $\boldsymbol{F}^*(x)$ and $\widehat{\boldsymbol{F}}_N^*(x)$:

$$1 - f = \hat{\alpha}_1^{(0)}. \tag{3.38}$$

Note that parameter f is solely determined by the fitting of $a_1(x)$. This guarantees the consistency between scalar and vector versions of the δ-fit method. The final coefficient set for $\widehat{\boldsymbol{F}}_N^*(x)$ is obtained by scaling all coefficients from the fitting Eqs. (3.36) and (3.37):

$$\hat{\alpha}_p^{(s)*} = \frac{\hat{\alpha}_p^{(s)}}{1-f}\,, \tag{3.39}$$

$$\hat{\beta}_q^{(s)*} = \frac{\hat{\beta}_q^{(s)}}{1-f}\,. \tag{3.40}$$

3.5 Theoretical comparison with other approaches

There are some other approaches to adapt the δ-fit method to fit a scattering matrix. Zhai et al. (2009) used the standard δ-fit method to fit $a_1(x)$, and applied a scaling to obtain other matrix elements to fit. Their scaling is as follows:

$$a_{p,Z}^*(x) = \frac{a_p(x)}{a_1(x)}\hat{a}_{1N}^*(x)\,, \tag{3.41}$$

$$b_{q,Z}^*(x) = \frac{b_q(x)}{a_1(x)}\hat{a}_{1N}^*(x)\,, \tag{3.42}$$

where Z indicates that the phase matrix elements in the left hand side is to be fitted by their method.

The rationale for this treatment is the consistency of ratios a_p/a_1 and b_p/a_1 in all scattering directions. Ignoring the exact forward scattering direction and using Eqs. (3.25) and (3.35), we can rewrite Eqs. (3.41) and (3.42) as follows:

$$a_{p,Z}^*(x) = \frac{(1-f)a_p^*}{(1-f)a_1^*}\left[a_1^* + \varepsilon_{fit}(x)\right] = \left[1 + \frac{\varepsilon_{fit}(x)}{a_1^*}\right]a_p^*(x), \tag{3.43}$$

$$b_{q,Z}^*(x) = \frac{(1-f)b_q^*}{(1-f)a_1^*}\left[a_1^* + \varepsilon_{fit}(x)\right] = \left[1 + \frac{\varepsilon_{fit}(x)}{a_1^*}\right]b_q^*(x). \tag{3.44}$$

Note that these relations are strictly applicable except for the exact forward scattering direction. As discussed in the previous section, $\varepsilon_{fit}(x)$ is small except at small scattering

angles. Therefore, the present approach and the approach suggested by Zhai et al. (2009) fit nearly the same function to obtain the expansion coefficients in side- to back-scattering directions.

Another adaptation proposed by Sanghavi and Stephens (2015) also uses the standard δ-fit method to obtain coefficients $\hat{\alpha}_p^{(s)*}$. The other reconstructed diagonal elements in the scattering matrix are as follows (see, Eq. 38 in Sanghavi and Stephens (2015)]):

$$\hat{a}_{2,N,S}^{*}(x) = \hat{a}_{2,N}^{*}(x) - f\sum_{s=0}^{N}\frac{2s+1}{1-f}\left[P_{2,2}^{(s)}(x) + P_{2,-2}^{(s)}(x)\right], \tag{3.45}$$

$$\hat{a}_{3,N,S}^{*}(x) = \hat{a}_{3,N}^{*}(x) - f\sum_{s=0}^{N}\frac{2s+1}{1-f}\left[P_{2,2}^{(s)}(x) - P_{2,-2}^{(s)}(x)\right], \tag{3.46}$$

$$\hat{a}_{4,N,S}^{*}(x) = \hat{a}_{4,N}^{*}(x) - f\sum_{s=0}^{N}\frac{2s+1}{1-f}P_{0,0}^{(s)}(x). \tag{3.47}$$

where S indicates that the phase matrix element is computed by Sanghavi's method.

The second terms in Eqs, (3.45)-(3.47) are small when the number of expansion coefficients N is large.

3.6 Adjustments for numerical implementation

Unlike phase functions, scattering phase matrix elements often have zeros (neutral points) at some scattering angles. As obvious from Eq. (3.13), the original δ-fit method uses the weight $(\varepsilon_1\mathcal{P}(x_i))^{-2}$, which is undefined at the aforementioned points. It is also counterintuitive that the accuracy of light scattering computation increases near neutral points. For this reason, we introduce an additional error term ε_2 to the weighting.

The weighted fittings of the scattering phase matrix elements are performed by minimizing the following quantities:

$$\varepsilon'_{a_1} = \sum_{i=1}^{m} (\hat{a}_{1N}(x_i) - a_1(x_i))^2 \frac{w_i}{[\varepsilon_1 a_1(x_i)]^2 + [\varepsilon_2]^2}, \tag{3.46}$$

$$\varepsilon'_{a_+} = \sum_{i=1}^{m} (\hat{a}_{+N}(x_i) - a_+(x_i))^2 \frac{w_i}{[\varepsilon_1 a_2(x_i)]^2 + [\varepsilon_1 a_3(x_i)]^2 + [\varepsilon_2]^2}, \tag{3.47}$$

$$\varepsilon'_{a_-} = \sum_{i=1}^{m} (\hat{a}_{-N}(x_i) - a_-(x_i))^2 \frac{w_i}{[\varepsilon_1 a_2(x_i)]^2 + [\varepsilon_1 a_3(x_i)]^2 + [\varepsilon_2]^2}, \tag{3.48}$$

$$\varepsilon'_{a_4} = \sum_{i=1}^{m} (\hat{a}_{4N}(x_i) - a_4(x_i))^2 \frac{w_i}{[\varepsilon_1 a_4(x_i)]^2 + [\varepsilon_2]^2}, \tag{3.49}$$

$$\varepsilon'_{b_1} = \sum_{i=1}^{m} \left(\hat{b}_{1N}(x_i) - b_1(x_i)\right)^2 \frac{w_i}{[\varepsilon_1 b_1(x_i)]^2 + [\varepsilon_2]^2}, \tag{3.50}$$

$$\varepsilon'_{b_2} = \sum_{i=1}^{m} \left(\hat{b}_{2N}(x_i) - b_2(x_i)\right)^2 \frac{w_i}{[\varepsilon_1 b_2(x_i)]^2 + [\varepsilon_2]^2}. \tag{3.51}$$

Note that $a_1(x_i), \ldots, b_2(x_i)$ are original scattering phase matrix elements, and $\hat{a}_{1N}(x_i), \ldots, \hat{b}_{2N}(x_i)$ are reconstructed scattering phase matrix elements from N coefficients. Our experiments show that $\varepsilon_1 = 10^{-7}$ and $\varepsilon_2 = 10^{-10}$ are good choices for fitting typical bulk scattering properties of cloud and aerosol particles.

The original δ-fit method resamples the phase function at equal scattering angle intervals, but some other investigators use an equal sampling with respect to the cosine of scattering angles. The present numerical simulations show that the fitting results are

better when equal $\mu = \cos\Theta$ intervals are used, or w_i are taken proportional to the difference of μ if other intervals are chosen.

3.7 Numerical validation of the theory

To demonstrate the performance of the vectorized δ-fit method, reflectivity and transmissivity of an ice cloud layer are computed by the adding-doubling radiative transfer model (de Haan et al., 1987; Huang et al., 2015). A moderately roughened hexagonal column shape is selected from the scattering property library (Yang et al., 2013), and weighted over a gamma-like particle size distribution. The effective variance of the distribution is 0.1 and the effective diameter is $D_{eff} = 30$ μm. The cloud optical thickness is 5. Simulations are conducted at 0.865 μm, and no contributions from background aerosol scattering and molecular Rayleigh scattering are considered.

The original phase matrix is fully expanded with 700 expansion coefficients for each scattering matrix element. The radiative transfer simulation result with 700 expansion coefficients is therefore used as a reference. The simulation results with scattering matrices truncated at 50 coefficients are compared with the reference. For the δ-fit method, the truncation angle is set to 5°. The original and reconstructed scattering phase matrix elements are shown in Fig. 3.1.

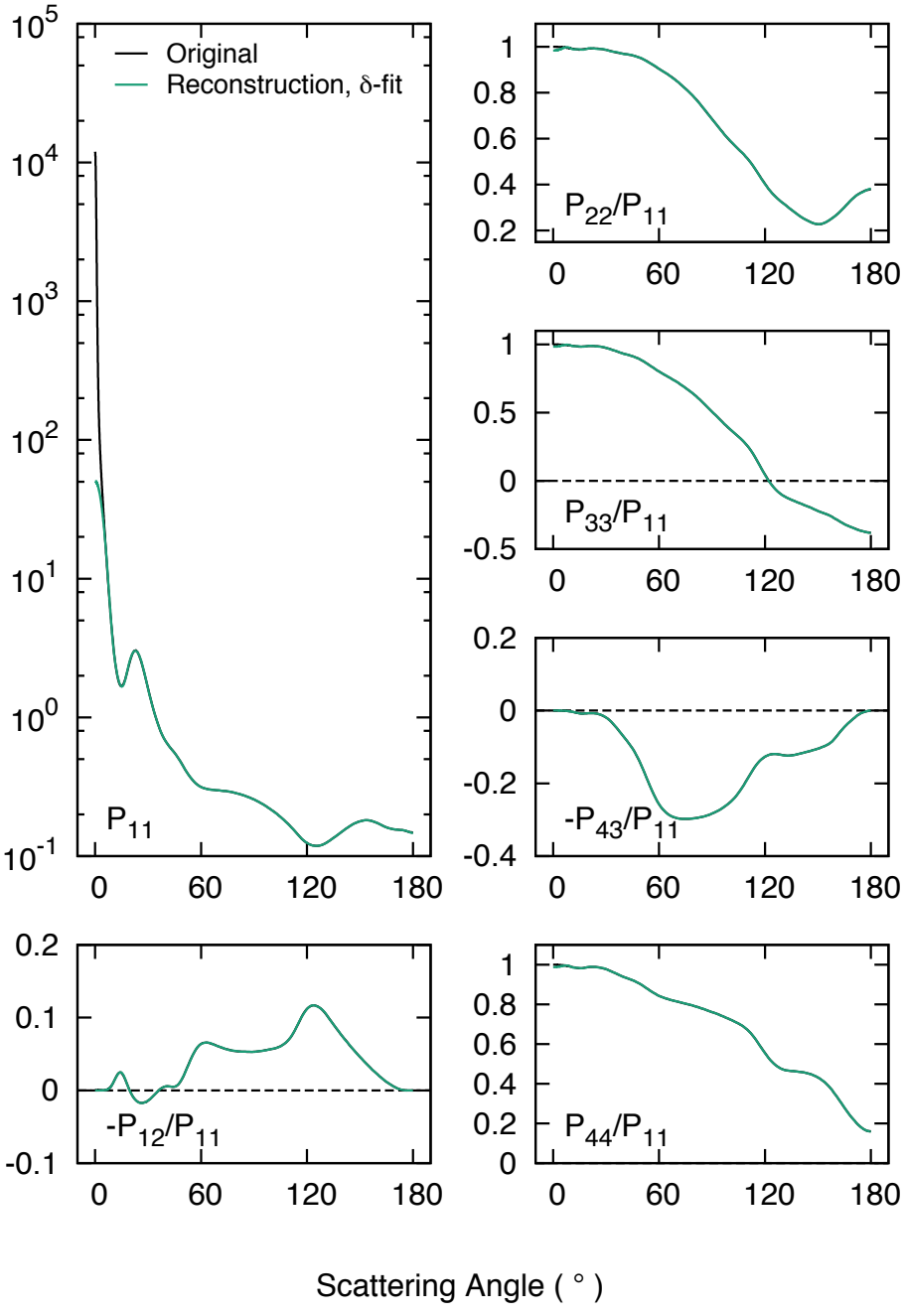

Fig. 3.1. Original and reconstructed scattering phase matrix elements. The reconstruction is from 50 coefficients computed by the δ-fit method. The scattering phase matrix elements are identical except in the forward direction.

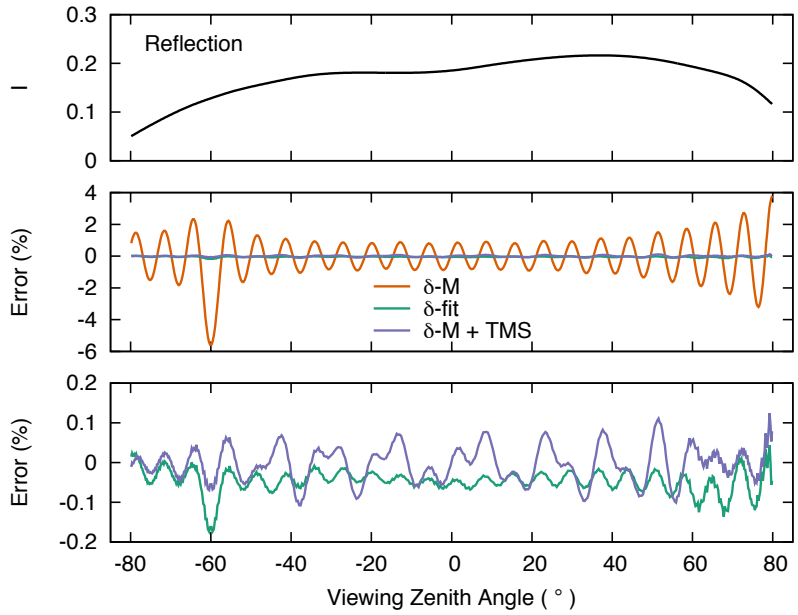

Fig. 3.2. Reflected radiance and relative errors. The radiance in the principal plane is computed with an untruncated scattering matrix with 700 expansion coefficients (top), and relative errors are plotted when the expansion is truncated at 50 coefficients (middle, bottom). The bottom panel expands around zero error. The solar zenith angle is $\theta_0 = 60°$, and the result for relative azimuth angle $\phi = 0°$ is plotted with positive viewing zenith angles, and the result for relative azimuth angle $\phi = 180°$ is plotted with negative viewing zenith angles. The peak in the error at $-60°$ corresponds to the glory direction.

Fig. 3.2 shows the result for the reflected radiance in the principal plane. The top panel is the intensity of the reference calculation, and the middle and bottom panels show relative errors of truncated simulations. The δ-fit method which has no TMS correction performs as well as the δ-M method with TMS correction. The amplitude of oscillation in the reflected radiance is smallest when the δ-fit method is used, but the bias is close to zero with the δ-M plus TMS method. These results agree with previous studies (Rozanov and Lyapustin, 2010; Iwabuchi and Suzuki, 2009). The transmissivity of the same cloud layer is presented in Fig. 3.3. The combination of the δ-M and TMS

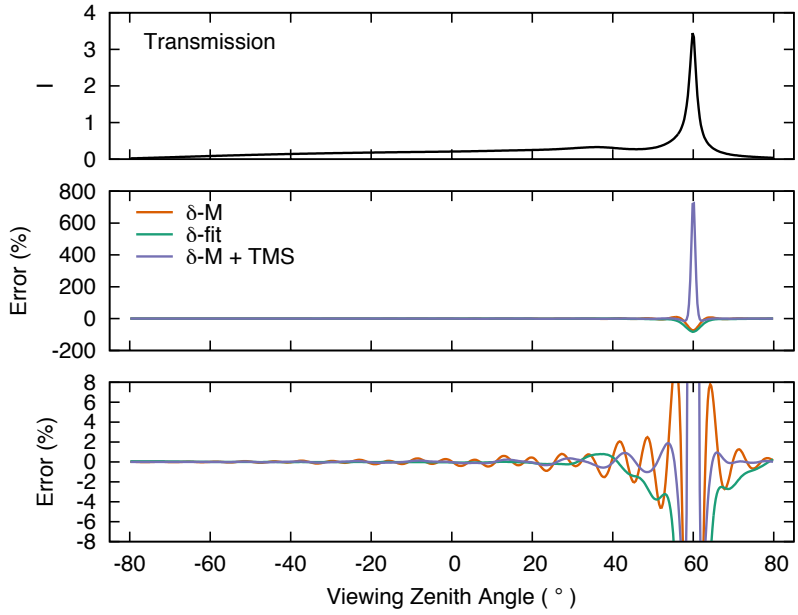

Fig. 3.3. Transmitted radiance and relative errors. Lines indicate the same as Fig. 3.2, but for transmitted radiance.

methods results in a significant error in the forward direction. This is because the TMS method introduces a spurious source term in the forward direction.

Figures 3.4 and 3.5 shows the second element (Q) of the Stokes vector in the reflected and transmitted directions. The polarized reflectivity calculation with the δ-fit method shows a significant improvement over the δ-M method. The overall errors of δ-M + TMS and δ-fit methods are comparable, but the δ-M + TMS method shows smaller biases. The transmission calculation indicates that the δ-fit method performs worse, even compared to the δ-M method without TMS correction except near the forward direction. Since the δ-fit method improves scattering matrix consistency in side- to back-scattering directions at the expense of accuracy in forward scattering directions, the result is not surprising.

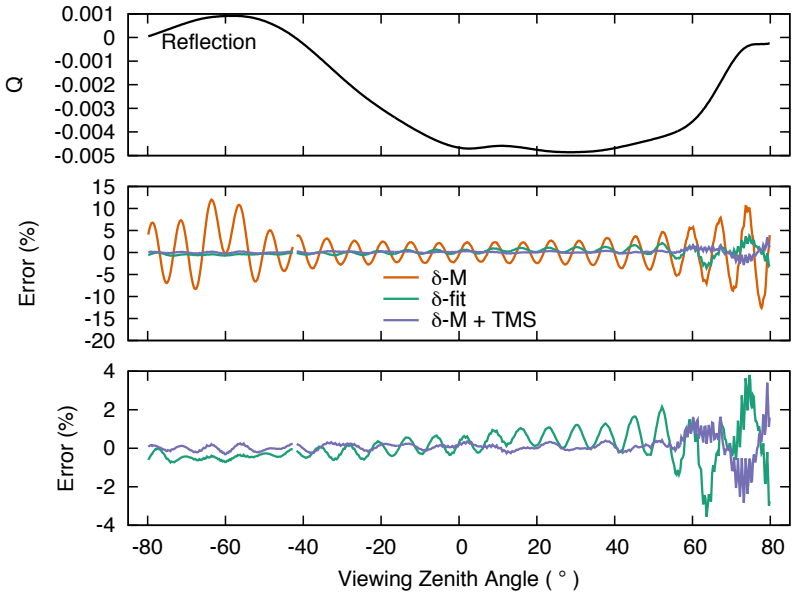

Fig. 3.4. Reflected second element of the Stokes vector and relative errors. Note that the third element is zero in the principal plane. In the vicinity of neutral points, data points are removed from relative error plots (middle, bottom)

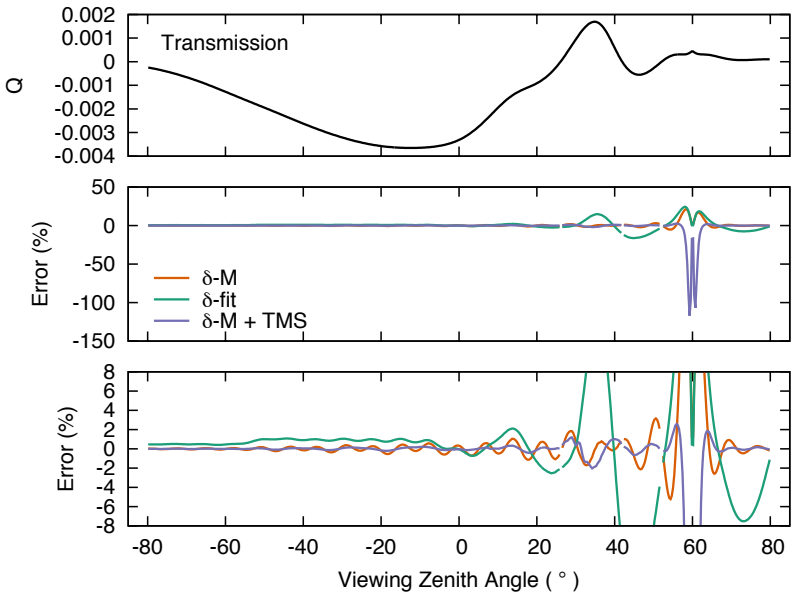

Fig. 3.5. Transmitted second element of the Stokes vector and relative errors.

3.8 Conclusions

This study interprets the δ-fit method as a correction to the source function by adapting the similarity transformation to be mathematically exact. With this theoretical framework, the traditional δ-fit method is extended for phase matrix expansion. The vectorized δ-fit method is consistent with the traditional δ-fit method for the first scattering matrix element a_1. Some adjustments to the traditional δ-fit method are applied to cope with a problem that is specific to phase matrix expansion.

The numerical experiment with an ice cloud phase matrix shows that the vectorized δ-fit method performs as well as the δ-M plus TMS method for reflectivity and polarized reflectivity calculations in the principal plane. The transmitted radiance calculation by the δ-fit method is also comparable to the δ-M plus TMS method, but achieves better accuracy in the forward directions. The polarized transmitted radiance by the δ-fit method suffers from larger error than the δ-M method without TMS correction, especially in the forward direction. This is presumably because of the design of the δ-fit method.

In the following parts of the dissertation, the δ-M method with TMS correction (120 streams) is used to accelerate the radiative transfer calculations. While accuracies of the δ-fit method and δ-M method with TMS correction are comparable, the δ-M plus TMS method is advantageous in the calculation of small differences between phase matrices because the method does not involve a fitting process.

4 TWO-STAGE RETRIEVALS OF PARTICLE SHAPE AND SURFACE ROUGHNESS*

4.1 Introduction

Satellite observations at visible and infrared wavelengths can characterize global cloud microphysical parameters and radiative properties. Numerous techniques have been developed to retrieve ice cloud optical and microphysical properties from radiometric measurements (e.g., Inoue, 1987; Nakajima and King, 1990; Minnis et al., 1993) and have been adopted in operational retrieval efforts (Rolland et al., 2000; Platnick et al., 2003; Minnis et al., 2011). A synergetic combination of satellite and in-situ observations (e.g., Heymsfield et al., 2002, 2013) serves as a constraint for the parameterization of bulk ice cloud optical properties for remote sensing implementations as well as general circulation models (GCMs).

The accuracy of these retrieval techniques and the validity of downstream applications including GCM radiation parameterization hinges on single scattering properties used in the retrievals. As ice clouds consist of nonspherical particles with characteristic sizes much larger than the wavelengths of interest, the single-scattering properties depend on the size, shape, and microscopic morphology of the particles (Macke et al., 1996; Yang et al., 2008a; Xie et al., 2009; Baum et al., 2010; Um and McFarquhar, 2007, 2009; Ulanowski et al., 2006, 2014). In the solar shortwave

* Part of this section is reprinted with permission from "Degree of ice particle surface roughness inferred from polarimetric observations" by Souichiro Hioki, Ping Yang, Bryan A. Baum, Steven Platnick, Kerry G. Meyer, Michael D. King, and Jérôme Riedi, 2016. Atmos. Chem. Phys., 16, 7545-7558. Copyright [2016] by Authors.

spectrum, particle shape, surface texture, and crystal imperfections have a substantial influence on the single-scattering properties. Recent improvements in scattering calculation techniques are being incorporated into models that represent diverse ice particle populations in clouds. As a consequence, the degree of freedom on the ice particle model has dramatically increased, and validations are needed.

The knowledge of ice cloud particle shapes, surface textures, and crystal imperfections still requires a substantial improvement. An improved particle model reduces the uncertainty of retrieved parameters from satellite data, microphysical parameters from the GCM microphysics scheme, and flux estimation from the GCM radiation scheme. The discrepancies among climate models (Waliser et al., 2009), in terms of ice water path (IWP), indicate that GCM parameterizations need more reliable constraints on IWP. One approach to validate IWP simulations in a GCM is to retrieve the IWP from the spaceborne measurements (e.g., Sourdeval et al., 2015) and compare with IWP computed from GCM.

The ability of visible/infrared imaging sensors to correctly infer IWP depends on the knowledge of ice cloud single scattering properties. Application of an unrealistic ice model, e.g., with only smooth (unroughened) surfaces, results in an overall global bias (Macke and Mishchenko 1996; Yang et al., 2007, 2008b; Holz et al., 2015), as well as seasonal biases (Zhang et al., 2009) in cloud property retrievals. The overarching goal of this section is to gain a better understanding of the constraints in the microphysical parameters of global ice clouds using angular polarimetric observations and state-of-the-art light-scattering computational capabilities.

The previous studies imply that the use of roughened particles is necessary to achieve maximum consistency between observations and numerical scattering calculations. Polarization measurements have been used to infer both particle habit (Chepfer, 1998; C.-Labonnote et al., 2001; Masuda et al., 2002; Knap et al., 2005; Baran and C.-Labonnote, 2007) and surface roughness (Baran and C.-Labonnote, 2006; Cole et al., 2013, 2014). Furthermore, Liu et al. (2014) and Holz et al. (2015) concluded that the spectral consistency of retrieved ice cloud optical thickness between visible/near-infrared and thermal infrared retrievals (Baran and Francis, 2004) improves when particles are roughened.

The treatment of particle surface roughness here is not a rigorous approach. Rather, it is an approximation of the effects of roughened surface texture (Neshyba et al., 2013) and other kinds of imperfections present in natural ice cloud. In this study, I used the surface tilt method (Section 2.3.1) with Yang-1 distribution (Section 2.2.2), which is consistent with MODIS and CERES ice particle models. The scattering properties calculated by this approximate method are in reasonable agreement with those calculated by rigorous ray-tracing methods (Yang et al., 2008a). Although previous studies suggest that some degree of roughness is desirable, the issue remains as to the amount of roughness that should be adopted for global satellite-based retrievals.

The conventional method to validate particle shape and the degree of surface roughness from polarimetric measurement utilizes the sensitivity of the polarization state of reflected light to small-scale particle structures and the insensitivity of the polarization to optical thickness. Since polarized reflectivity saturates at a relatively

small optical thickness (generally about $\tau = 5$, Masuda and Takashima, 1992), thick cloud pixels are selected based on the total reflectivity, and the residual sum of squares (RSS) are computed from the multi-angle observations of polarized reflectivity and reflectivity simulations. The particle model that minimizes the RSS is considered as the "best" model. I refer to this conventional method as the "best-fit" approach.

By utilizing the "best-fit" approach, recent work by van Diedenhoven et al. (2012, 2014) simultaneously infers both the aspect ratio and the degree of roughness from a combination of polarimetric and intensity observations over a virtually continuous parameter space, assuming that simple hexagonal ice particles can explain the observations. The ability to infer a representative ice cloud particle aspect ratio adds yet another dimension to the problem. Such exploration into the variability of ice particle microphysical properties can lead to a more reliable satellite climatology of ice clouds.

While the conventional "best-fit" approach can constrain the range of the average roughness parameter on a global scale, it is not suitable for pixel-by-pixel inferences. This is because the signal-to-noise ratio for particle roughness is low, and in the conventional "best-fit" approach, even random observational errors can modify the inferred histogram significantly when it is applied to individual pixels. Figure 4.1 illustrates how such a modification takes place if the method is applied to a synthetic signal with random noise. To produce Fig. 4.1, viewing geometries are extracted from one month (September 2005) of cloud observations by the POLarization and Directionality of the Earth's Reflectance (POLDER) sensor (Deschamps et al., 1994) onboard the Polarization and Anisotropy of Reflectances for Atmospheric Sciences

coupled with Observation from Lidar (PARASOL) satellite (Fougnie et al., 2007). The "best-fit" inference is applied to synthetic multi-angle cloud polarized reflectivities (L_p, defined in Section 4.2.1) with and without random noise. In synthesizing the signal, a column aggregate particle shape (e.g. Yang et al., 2013) is assumed with a roughness parameter of $\sigma^2 = 0.15$. For the definition of this parameter, readers are referred to Section 2.2.2. Radiative transfer calculations are performed assuming an optical thickness $\tau = 5$, and the random error following a normal distribution is added. The variance of the applied error term is equivalent to the POLDER observational error estimated in Section 4.2.2. The hatched bar is the histogram with noise and the gray bar is that without noise. Note that the distinct peak at $\sigma^2 = 0.15$ is no longer apparent when instrumental noise is included, indicating the necessity of appropriate treatment of the error distribution in the analysis.

The rest of this section is constructed as follows. Section 4.2 describes the characteristics of the POLDER instrument, and Section 4.3 introduces the two-stage retrieval technique that is less sensitive to measurement errors. The method is applied to two cases and results are discussed in Section 4.4 and 4.5: surface roughness retrieval with a fixed particle shape (Section 4.4) and variable shape and roughness retrieval (Section 4.5). Section 4.6 summarizes the findings.

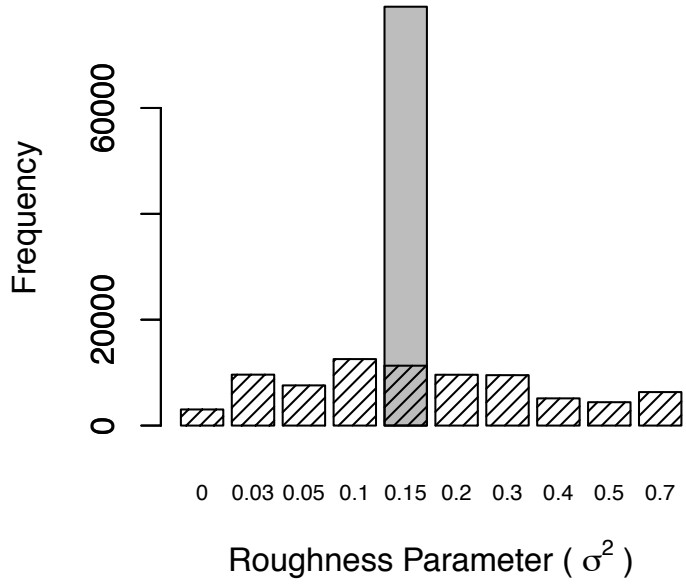

Fig. 4.1. The response of the conventional "best-fit" approach to a synthetic signal. The solid bars correspond to retrieval without random measurement noise and the hatched bars correspond to retrieval with measurement noise. The addition of noise to the synthetic signal results in a distribution of the roughness parameter, from which the true roughness cannot be inferred. This figure is to be compared to Fig. 4.12.

4.2 Error characteristics of the POLDER sensor

To establish a method resilient to observational error, we first examine random errors in POLDER data. Section 4.2.1 provides the overview of the POLDER sensor, and the error is characterized in Section 4.2.2.

4.2.1 Reflectivity and polarized reflectivity from the POLDER

The POLDER sensor aboard the PARASOL satellite provides multispectral polarimetric observations at up to 16 viewing geometries for a single overpass (Fougnie et al., 2007). The PARASOL satellite was in the A-train satellite constellation from 2004 to 2009 and continued operation in a separate orbit until late 2013, providing a total of nine years of global polarimetric observation data. The design of the instrument is

inherited from previous POLDER sensors on the ADEOS (ADvanced Earth Observing Satellite) platforms. POLDER sensors provide the first three elements of the Stokes vector from three images taken successively with linear polarization filters (Deschamps et al., 1994).

This study uses the single-pixel data set in the PARASOL Level 1B product. The nominal resolution of the nadir pixel is 6 km × 6 km. PARASOL products report the intensity of reflection in terms of normalized radiance L_n, which is equal to the reflectivity R of the surface-atmosphere system multiplied by the factor $\mu_0 = \cos\theta_0$(cosine of solar zenith angle).

$$L_n(\mu, \mu_0, \varphi, \varphi_0) = \mu_0 R(\mu, \mu_0, \varphi, \varphi_0) \tag{4.1}$$

The reflectivity R is defined as

$$R(\mu, \mu_0, \varphi, \varphi_0) = \frac{\pi I(\mu, \mu_0, \varphi, \varphi_0)}{E_0 \mu_0} \tag{4.2}$$

where $I(\mu, \mu_0, \varphi, \varphi_0)$ is the radiance and $E_0\mu_0$ is the irradiance of incoming unpolarized light (i.e., solar irradiance; E_0 is the beam flux).

In a similar manner, the polarized reflectivity is reported in terms of normalized radiance, so (L_n, Q, U) become the first three Stokes parameters. In other words, the normalized polarized radiance $L_{np} = \sqrt{Q^2 + U^2}$ is equal to the polarized reflectivity R_p multiplied by μ_0.

$$L_{np}(\mu, \mu_0, \varphi, \varphi_0) = \mu_0 R_p(\mu, \mu_0, \varphi, \varphi_0) = \frac{\pi\sqrt{Q_i^2 + U_i^2}}{E_0}, \tag{4.3}$$

where Q_i and U_i are defined to form the first three Stokes parameters in terms of radiance (I, Q_i, U_i). It is worth noting the similarity between Eqs. (4.1) and (4.3). We conduct the analysis in terms of $L_{np} = \mu_0 R_p$ defined in Eq. (4.3) to simplify the error estimation.

4.2.2 The error characteristics

The distribution of random errors in L_{np} observed with the POLDER is estimated in the following procedure. A reflection property of an optically thick ice cloud is that the modified polarized reflectivity $L_{nmp} = \eta(\mu + \mu_0)L_{np}/\mu_0$ (where $\eta = \pm 1$, C.-Labonnote et al., 2001) crosses zero at scattering angle $\Theta \approx 170°$ as shown in Fig. 4.2. This implies that the polarization signal at $\Theta \approx 170°$ is primarily due to the observational noise with additional contributions from the variation of cloud particle scattering properties. We utilize this reflection property to estimate the magnitude of observational noise from the POLDER data at scattering angles between 168° and 172°, and further estimate the noise level at other angles with a typical polarization state of cloud reflection.

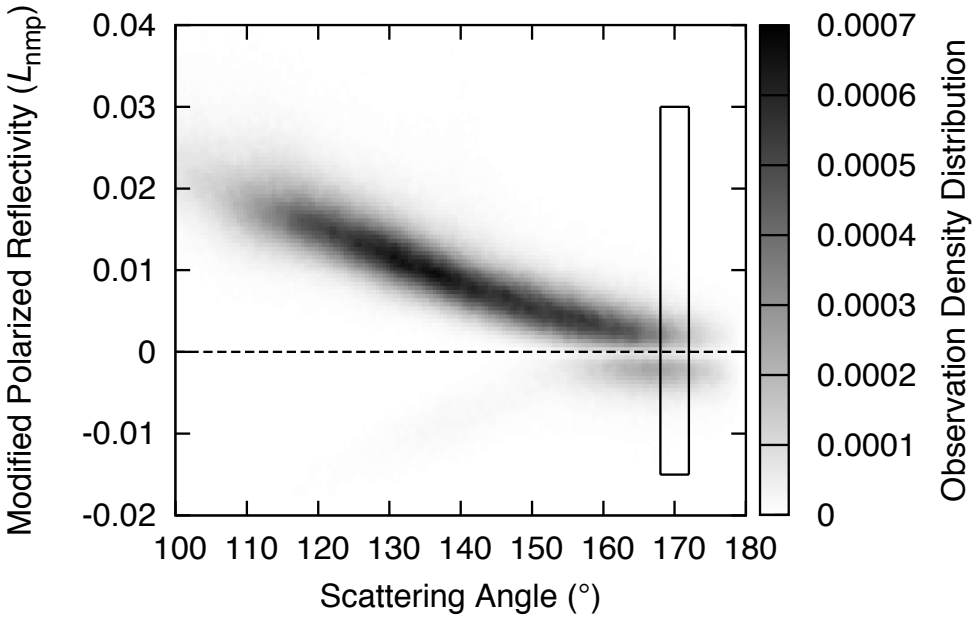

Fig. 4.2. Observation density of modified polarized reflectivity (L_{nmp}). Measurements are collected over the Western Pacific during September 2005. L_{nmp} crosses zero at a scattering angle of approximately 170°. The data in the rectangular box is used to derive the histogram in Fig. 4.3.

The POLDER observational noise consists of radiometric noise and misregistration noise. The misregistration noise is inherent in the POLDER sensor's design that extracts polarimetric information from three images successively taken with different polarizers. The co-registration process of these three images is an inevitable source of error. As the distribution of misregistration noise is unknown, our instrument model attempts to explain both noise components with a radiometric noise model in the following analysis.

We define a random variable L_{np} that serves as a statistical model of observed L_{np} as follows.

$$L_{np} = \sqrt{X_1^2 + X_2^2 + X_3^2 - X_1X_2 - X_2X_3 - X_3X_1} \tag{4.4}$$

where random variables X_1, X_2, and X_3 represent the radiances of a pixel in the original three images with different polarizers (not available in a product). With the statistical model outlined in Eq. (4.4), we first assume that X_1, X_2, and X_3 follow the same normal distribution centered at 0.5 with variance s^2 (i.e., $X_i \sim \mathrm{N}(0.5, s^2)$) because the expectation of polarized radiance L_{np} is assumed to be zero at scattering angles between 168° and 172°. Note that $L_{np} = 0$ when $X_1 = X_2 = X_3$ in Eq (4.4). With this assumption, we apply the parametric bootstrap method (e.g., Evans and Rosenthal, 2010) to obtain the distribution of L_{np} as a function of variance s^2. The observational distribution of L_{np} at 0.865 μm in the scattering angles between 168° and 172° (within the rectangular box in Fig. 4.2) is shown in the bar chart of Fig. 4.3, and compared with the theoretical distribution with $s = 0.00095$ (solid line). Figure 4.4 justifies our selection of $s = 0.00095$ by showing that the sum of squared errors of the density in each bin of the histogram (Fig. 4.3) is minimized when $s = 0.00095$. Therefore, we take $s = 0.00095$ as the standard error for X_1, X_2, and X_3. In Fig. 4.3, the distribution from observations is slightly more skewed than the distribution from bootstrapping, but their agreement justifies the use of the simple statistical model formulated in Eq. (4.4) to quantify the magnitude of measurement errors.

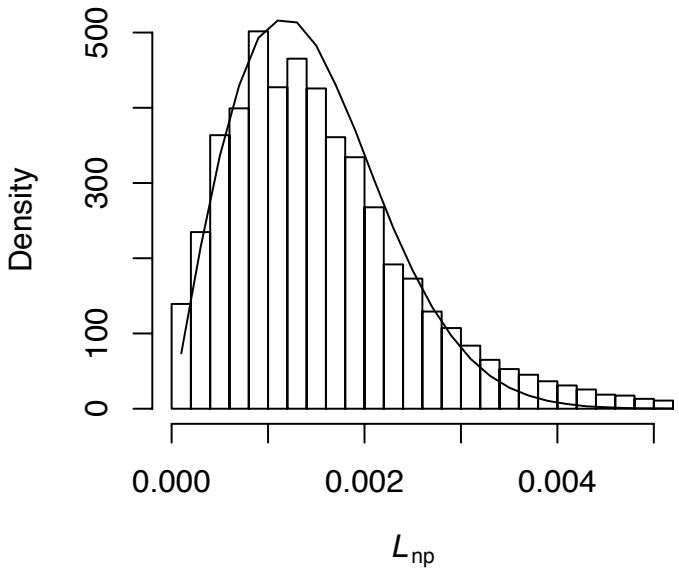

Fig. 4.3. Histogram of observed normalized polarized radiance (L_{np}). Data are from the rectangular box in Fig. 4.2. The solid line is the simulated error using a parametric bootstrapping method with $s = 0.00095$. The agreement is sufficient for estimating the noise level.

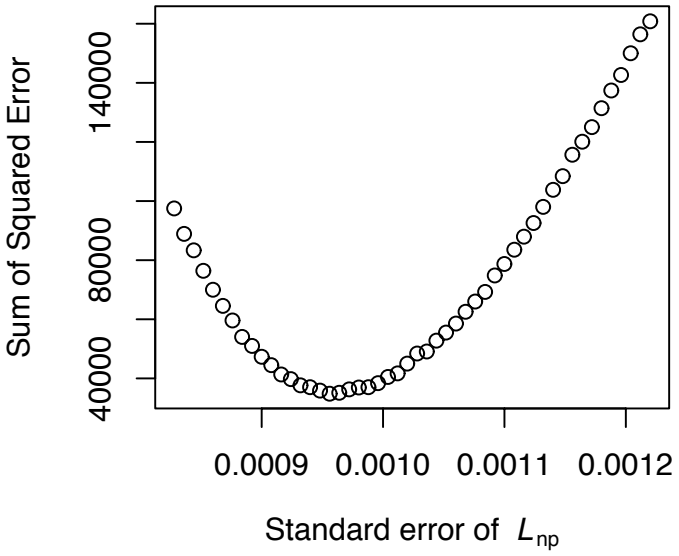

Fig. 4.4. Sum of squared error as a function of standard error (s). The minimum error is achieved when $s = 0.00095$.

To obtain the approximate magnitude of the L_{np} error at other scattering angles, the same parametric bootstrap method is applied with the degree of linear polarization fixed at 5%, which is the upper limit for typical ice cloud reflection. This selection does not significantly affect the results obtained by the following analysis. When the signal is polarized, random variables X_1, X_2, and X_3 do not follow the same distribution, but it is still reasonable to assume that the standard errors for X_1, X_2, and X_3 still stay the same because they are measured by the same imaging sensor. Figure 4.5 shows the estimated magnitude of error (variance) as a function of normalized radiance L_n. The variance of L_{np} asymptotically approaches to a near-constant value once L_n reaches $L_n = 0.2$. As shown in insets, the simulated distribution becomes closer to a normal distribution with increasing L_n (i.e. cloud becomes brighter). Based on the discussion above, we conclude that the error distribution of L_{np} approximately follows a normal distribution with variance $\mathrm{var}(L_{np}) = 1.35\times10^{-6}$ for a reflective target ($L_n \geq 0.2$). This estimate of error is about the same magnitude as the value by Fougnie et al. (2007). Note that we assume that the error is purely from observational noise, neglecting any natural cloud variability. Therefore, the actual radiometric noise level should be somewhat smaller than our estimate. We estimate the magnitude of error using the 0.865 μm channel because the channel is likely to be the least contaminated by other sources of uncertainty such as ozone absorption (0.67 μm) and Rayleigh scattering (0.49 μm, 0.67 μm). We apply the same variance to all three POLDER channels used in the analysis (0.865, 0.67, and 0.49 μm).

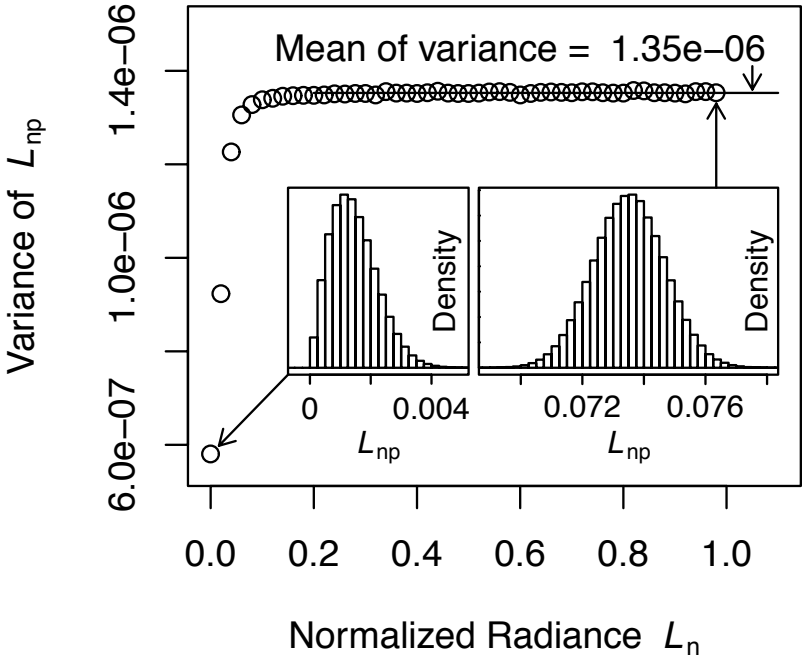

Fig. 4.5. The simulated variance of L_{np} as a function of L_n. The variance of L_{np}increases as the normalized radiance L_n (brightness of a pixel) increases, becoming nearly constant at $\mathrm{var}(L_{np}) = 1.35\times10^{-6}$ once L_n reaches $L_n = 0.2$. Insets show that the distribution of L_{np} tends to a normal distribution, justifying the use of a normal distribution as an error distribution of L_{np} for a reflective cloudy pixel.

4.3 Methodology – The two-stage method

The two-stage method consists of Stage 1: look-up table computation and Stage 2: maximum likelihood estimation. The unique feature of the two-stage method is that the particle shapes are parameterized by a few parameters and the retrieval is conducted in the continuous parameter space. The adaptation of maximum likelihood method makes the effect of noise more predictable than the "best-fit" method. The flow chart of the two-stage method is presented in Fig. 4.6. The primary input data are particle single scattering properties (Stage 1), PARASOL Level 1B product containing reflectivity data

(Stage 2), and MODIS Level 2 cloud product (Stage 2). Sections 4.3.1 and 4.3.2 describes Stage 1, and Section 4.3.3 describes Stage 2 below.

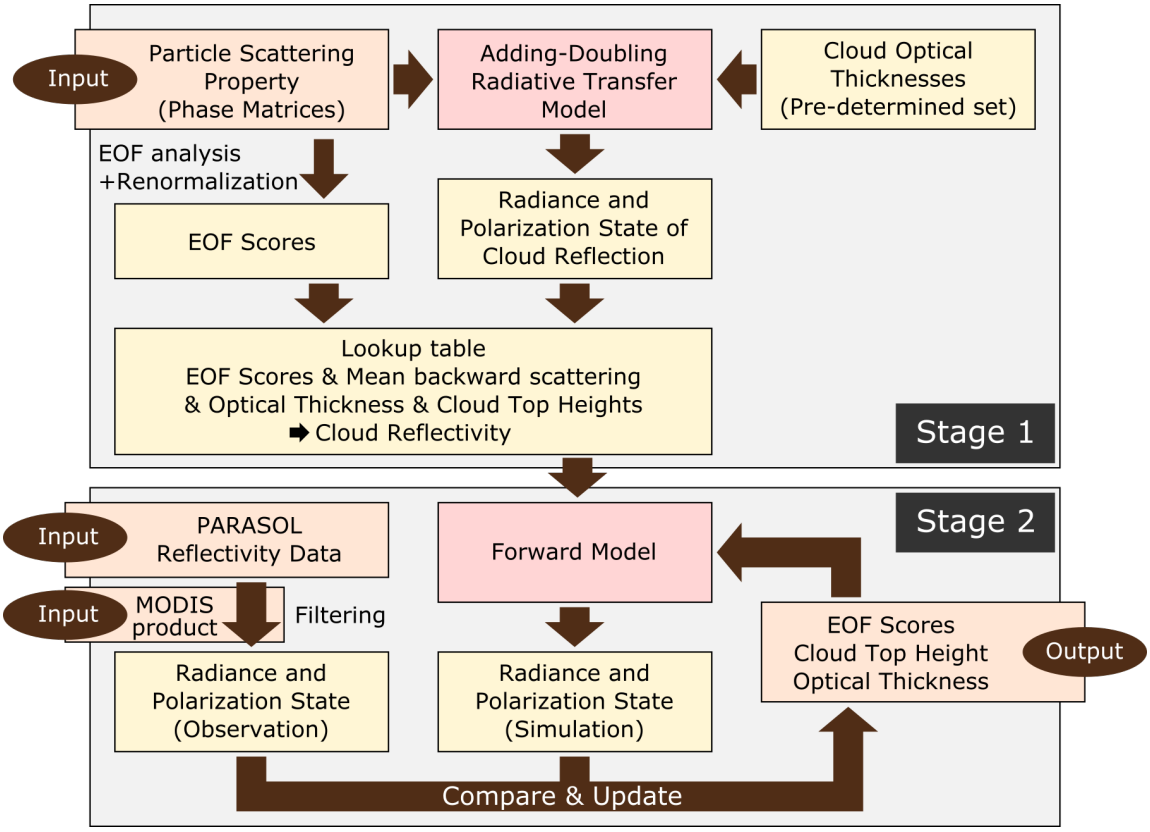

Fig. 4.6. The flow chart of the two-stage method.

4.3.1 Stage 1-1: Parameterization of particle shapes

To overcome the problem of the conventional "best-fit" approach that uses a discrete set of roughness parameters, we construct a continuous parameter space for the particle shape and roughness with empirical orthogonal functions (EOF). The goal of the EOF analysis is to find the parameters that describe the variation of the phase matrix elements when varying the particle shape and roughness. An ideal approach would be to

use a collection of phase function ($\mathcal{P}(\Theta)$) and the $-P_{12}(\Theta)$ element of the phase matrix from observations (Rodgers, 2000), but such a dataset is unavailable. For this reason, we apply EOF analysis to the $\mathcal{P}$ and $-P_{12}$ simulated with light scattering calculations.

For applications in Section 4.4 and 4.5, two different sets of phase matrices are prepared with light scattering calculations. I refer to the ice particle model used in Section 4.4 as Model A, and that used in Section 4.5 as Model B.

Model A consists of hexagonal column aggregate particles with a varying degree of surface roughness. The particles are aggregates of eight solid hexagonal column elements with slightly different particle aspect ratios (originally defined in Yang and Liou 1996, see Yang et al., 2013 for geometric parameters). Ten roughness parameter (σ^2) values are used: 0, 0.03, 0.05, 0.1, 0.15, 0.2, 0.3, 0.4, 0.5, and 0.7. These roughness parameters are selected to outline the variation of $-P_{12}$ over the course of roughness changes, including the roughness parameter used in MODIS Collection 6 ($\sigma^2 = 0.5$). The column aggregate shape is chosen because the most extensive previous study on a global scale (Cole et al., 2014) implies that this habit produces the most consistent agreement with observations. Scattering properties are computed with the Improved Geometric Optics Method (IGOM; Yang and Liou, 1996) for large particles ($D_{max} > 10$ μm) and the Amsterdam Discrete Dipole Approximation method (ADDA; Yurkin et al., 2007) for small particles. The edge effect is considered when combining the results from the ADDA method and the IGOM as described by Yang et al. (2013). A gamma particle size distribution with an effective size (diameter) of 60 μm and an effective variance of 0.1 (shape parameter $\alpha = 8$) is used, since we expect little impact on our analysis due to

this size distribution selection (Cole et al., 2014). Only $-P_{12}$ is used in the parameterization of Model A.

Model B consists of hexagonal column and plate particles with varying degrees of surface roughness and aspect ratio. Nine surface roughness values are used: 0.01, 0.03, 0.05. 0.1, 0.2, 0.3, 0.4, 0.5, 1, and 39 aspect ratio (ratio of basal face diameter to column height) values from 1/9 to 9 are used. Scattering properties are computed with the Improved Geometric Optics Method (IGOM; Yang and Liou, 1996) for large particles ($D_{max} > 11.2$ μm) and the Imbedded Invariant T-Matrix method (IITM; Bi and Yang, 2014) for small particles. The edge effect is taken into account when combining the results from the IITM method and the IGOM as described by Yang et al. (2013). Both $\mathcal{P}$ and $-P_{12}$ are used in the parameterization of Model B.

For Model A, the first and second EOFs together cover 99.3% of the entire variation of $-P_{12}$ in the scattering angle range from 60° to 160°. This implies that the following approximation is valid in the scattering angle range $60° < \Theta < 160°$.

$$-P_{12}(\Theta) = x_1(\sigma^2)q_1(\Theta) + x_2(\sigma^2)q_2(\Theta) \tag{4.5}$$

where Θ is the scattering angle, $q_1(\Theta)$ and $q_2(\Theta)$ are the first and second EOFs, and $x_1(\sigma^2)$ and $x_2(\sigma^2)$ are weights for EOFs (EOF Scores). The EOF scores are shown in Fig. 4.7. The EOF 1 primarily describes the degree of roughness, and the EOF 2 score has sensitivity to large roughness parameters.

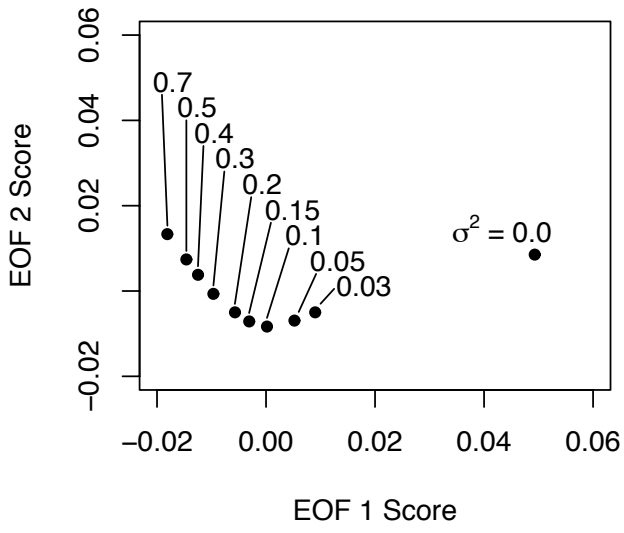

Fig. 4.7. The pairs of EOF scores needed to reconstruct the original $-P_{12}$. The EOF 1 score is a monotonic function of particle roughness parameter σ^2. The EOF 2 score reaches a minimum at particle roughness parameter of $\sigma^2 = 0.1$.

For Model B, the EOF analysis is applied to the combined function of $\mathcal{P}$ and $-P_{12}$ between 90° and 160° with a normalization by the average scattering intensity in the interval:

$$\rho = \int_{90°}^{160°} \mathcal{P}(\Theta) \sin\Theta \, d\Theta \tag{4.6}$$

The first and second EOFs together cover 88.4% of the entire variation of $\mathcal{P}$ and $-P_{12}$ in the scattering angle range from 90° to 160°. This implies that the following approximation is valid in the scattering angle range $90° < \Theta < 160°$.

$$\frac{\mathcal{P}(\Theta)}{\rho} = x_1(\sigma^2)Q_1(\Theta) + x_2(\sigma^2)Q_2(\Theta) \tag{4.7}$$

$$-\frac{P_{12}(\Theta)}{\rho} = x_1(\sigma^2)q_1(\Theta) + x_2(\sigma^2)q_2(\Theta) \tag{4.8}$$

where Θ is the scattering angle, $Q_1(\Theta)$ and $Q_2(\Theta)$ are the first and second EOFs of the $\mathcal{P}$ part of the combined EOF, $q_1(\Theta)$ and $q_2(\Theta)$ are the first and second EOFs of the $-P_{12}$ part, and $x_1(\sigma^2)$ and $x_2(\sigma^2)$ are weights for EOFs (EOF Scores). Since the EOF analysis is applied to the combined function $(\mathcal{P}, -P_{12})$, EOF scores x_1 and x_2 are common for $\mathcal{P}$ and $-P_{12}$. The EOF scores are shown in Fig. 4.8. A fan-like shape indicates that phase functions become similar when the degree of surface roughness increases.

Since the phase matrix follows a linear mixing rule, $\mathcal{P}$ and $-P_{12}$ of a mixture containing multiple degrees of roughness is also approximated by Eqs. (4.7) and (4.8). For example, a mixture of MODIS Collection 6 particle ($\sigma^2 = 0.5$) and moderately roughened particle ($\sigma^2 = 0.03$) produces EOF scores (x_1, x_2) on a straight line between $(x_1(0.5), x_2(0.5))$ and $(x_1(0.03), x_2(0.03))$. Constructing a continuous parameter space using EOF scores (x_1, x_2) is powerful because the method guarantees that the parameter space contains any mixture of prescribed shapes or degree of roughness.

When the normalization in Eq. (4.6) is used, the original phase function is decomposed into EOF scores (x_1, x_2), and mean backward scattering (ρ). Figure 4.9 shows the correlation between EOF 1 Score and mean backward scattering. Three branches are clearly evident for smooth particles, and for a roughened particle, x_1 and ρ are approximately on a straight line.

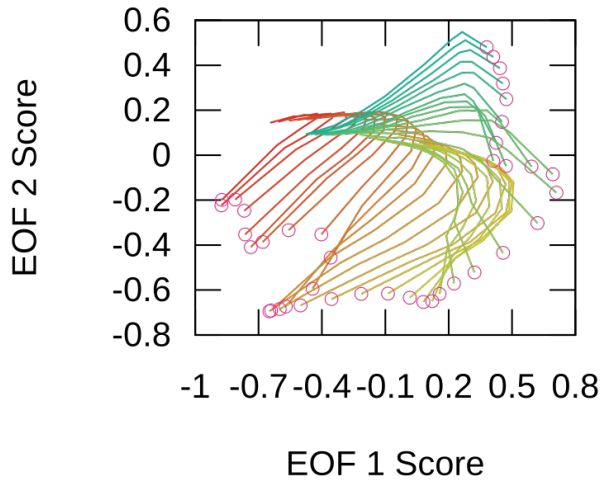

Fig. 4.8. The EOF scores of hexagonal column and plate particles. The aspect ratio is varied from 1/9 to 9, and surface roughness is varied from $\sigma^2 = 0.01$ to 1. Each line corresponds to one aspect ratio, and the green line corresponds to long columns, yellow lines correspond to compacts columns, and red lines correspond to plates. The end of each line with a circle representsthe least roughened particle ($\sigma^2 = 0.01$), and the end without a circle represents the most roughened particle ($\sigma^2 = 1$)

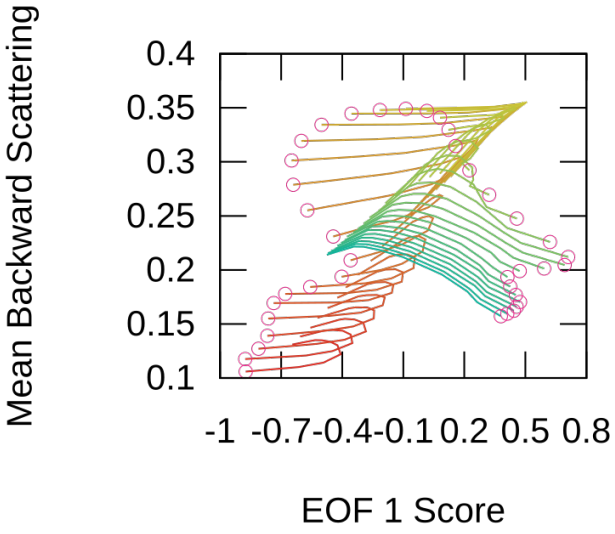

Fig. 4.9. The EOF 1 score and mean backward scattering (ρ). Color coding is the same as in Fig. 4.8.

4.3.2 Stage 1-2: Construction of the forward model

The particle shape is now parameterized by the combination of two EOF scores and mean backward scattering as (x_1, x_2, ρ). The additional parameters that are needed for the simulation of the POLDER observations are cloud top pressure and the cloud optical thickness. If the polarization-only analysis is conducted for optically thick clouds, the effect of optical thickness can be ignored since the polarized reflectivity saturates at a value of about $\tau = 5$.

The cloud top height influences the retrieval through atmospheric Rayleigh scattering above the cloud. Above-cloud Rayleigh scattering has previously been used to infer cloud top pressure from polarimetric measurements (e.g., Buriez et al., 1997), with results comparable to those from O_2-A band retrievals and ISCCP (Parol et al., 1999). With the POLDER instruments, Rayleigh scattering is primarily detected as a spectral and directional difference of polarized reflectivities. Figure 4.10 shows the change of L_{np} at 0.865 μm, as a function of scattering angle in response to a 300 hPa change in cloud top pressure (i.e., from 200 to 500 hPa, the red line). The dashed green line shows the change due to roughness parameter difference (from $\sigma^2 = 0.15$ to 0.5, the dashed green line) for Model A. The effects of cloud top pressure and roughness parameter changes on L_{np} have different directional patterns but comparable magnitudes. Variation of the cloud top pressure must therefore be well constrained or retrieved simultaneously when attempting to infer the roughness parameter. In this study, cloud top pressure is simultaneously retrieved in Section 4.4, while the cloud top pressure from MODIS is used in Section 4.5.

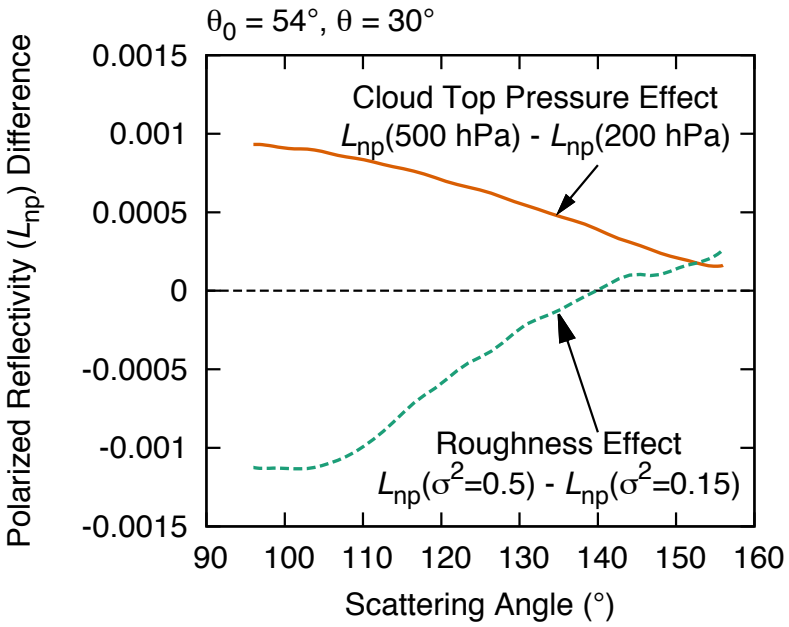

Fig. 4.10. The impact of particle roughness parameter change ($\sigma^2 = 0.15 \rightarrow 0.5$) and cloud top pressure change ($200 \rightarrow 500$ hPa). The magnitudes of the differences are comparable while the directional patterns are different. In this plot, the solar zenith angle is 54° and the viewing zenith angle is 30°.

For the application of the maximum likelihood estimation (Section 4.3.3), a forward model that is fast enough to be embedded in the inversion algorithm is needed. From the discussion in Section 4.3.1, the inverse problem is formalized as follows: (1) the parameters are the EOF 1 and EOF 2 scores, cloud top pressure, mean backward scattering (optional), and cloud optical thickness (optional); and (2) observation data are POLDER total and polarized reflectivity values. To satisfy the requirements for numerical efficiency, the present forward model is based on look up tables. The adding-doubling radiative transfer program is used to compute L_{np} for every phase matrix, cloud top pressure, and cloud optical thickness. The result at a specific viewing

geometry (denoted by subscript i), a mean backward scattering (denoted by subscript j), and an optical thickness (denoted by subscript k) is parameterized by a simple linear regression model defined as:

$$L_{np(i,j,k)} = a_{(i,j,k)} + b_{(i,j,k)}x_1 + c_{(i,j,k)}x_2 + d_{(i,j,k)}p_{top} \tag{4.9}$$

where x_1 and x_2 are EOF scores obtained in Sect. 4.3.1, p_{top} is the cloud top pressure, and $a_{(i,j,k)}$, $b_{(i,j,k)}$, and $c_{(i,j,k)}$ are regression coefficients. The viewing geometry is gridded as follows: solar zenith angles from 0° to 81°, viewing zenith angles from 0° to 75°, and relative azimuth angles from 0° to 180°, with an interval of 3° for each. The regression is repeated for seven atmospheric scattering optical thicknesses above the cloud and 40552 viewing geometries. With this forward model, once cloud top pressure, cloud optical thickness, EOF scores, and mean backward scattering are given, L_{np} can be obtained for each specific viewing geometry and wavelength. When a set of EOF scores (x_1, x_2) is not exactly at the values corresponding to the ten prescribed phase matrices, the forward model linearly interpolates the polarized reflectivity. We confirmed that the interpolation produces a reliable polarized reflectivity simulation for a phase matrix of intermediate roughness and a mixture of phase matrices.

The forward model constructed in this way is accurate enough to solve our inverse problem. I demonstrate this by taking the Model A as an example. A typical difference between an exact calculation and our forward model is shown in Fig. 4.11 for Model A. The overall accuracy is within 1×10^{-4} in terms of L_{np} and the peak-to-peak variation is 5×10^{-4} even in the worst case ($\sigma^2 = 0.03$). The overall error of 1×10^{-4}

implies that the model bias is less than 10% of the observation error given by ($\sqrt{\mathrm{var}(L_{np})} = \sqrt{1.35\times10^{-6}} = 1.16\times10^{-3}$). The bias may be detected in the residual of the inversion, but the influence on the roughness inference is negligible.

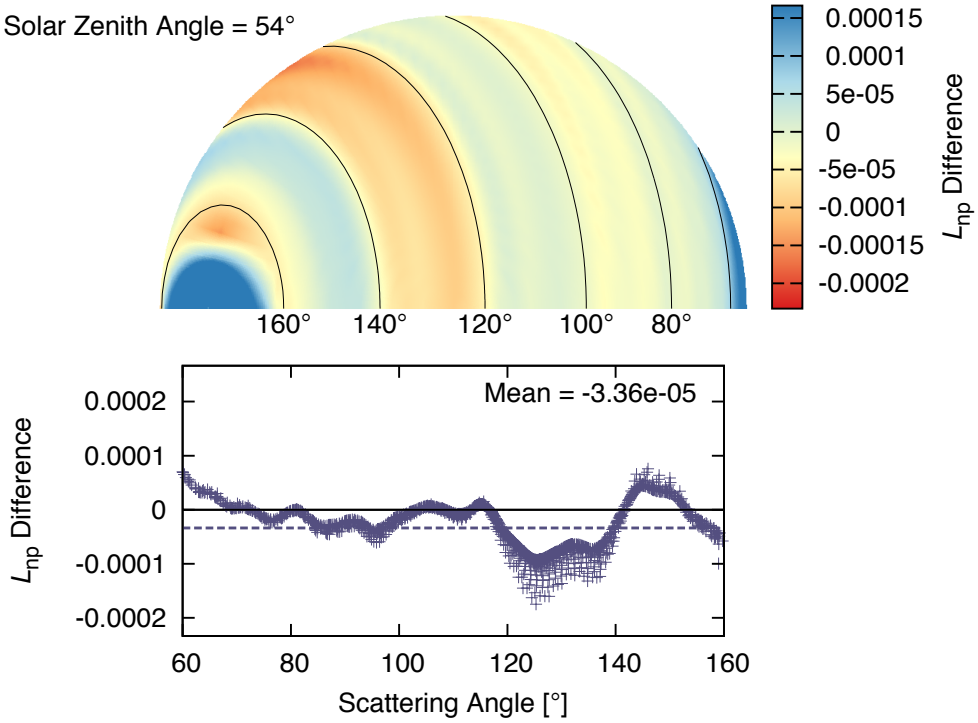

Fig. 4.11 Forward model error in L_{np}. Difference in L_{np} between exact radiative transfer calculations and our simplified forward model are plotted. At almost all angles, the difference is less than 1×10^{-4}. The polar plot shows the distribution of bias when the particle roughness parameter is $\sigma^2 = 0.15$. The bias is a function of scattering angle. However, the magnitude of error is acceptably small compared to the random observational error.

In calculating cloud reflectivity, a single-layer homogeneous cloud is assumed, and no aerosol is assumed to be present above and below clouds. As optically thick ice clouds occur in the upper troposphere, the radiometric contribution from lower

tropospheric aerosols is neglected. For the same reason, the surface is assumed to be dark. There may be an influence from aerosols above the cloud layer, such as transported mineral dust and stratospheric sulfates, but we disregard them to be consistent with previous studies. The influence of such aerosol layers on inferences of cloud properties is beyond the scope of this study.

For the reflectivity calculations, the adding-doubling radiative transfer program formulated by de Haan et al. (1987) with significant improvements by Huang et al. (2015) is used. The first-order scattering is calculated analytically and combined with the multiple scattering results from the adding-doubling model, following the TMS method (Nakajima and Tanaka, 1988). Further, the cloud reflectivity is multiplied by the transmissivity that changes due to ozone absorption for Model A retrieval. The forward model outline is summarized in Table 4.1.

Table 4.1. Forward model settings and retrieval configurations.

Parameters	Model A (Section 4.4)	Model B (Section 4.5)
Particle Shapes	Column Aggregate	Hexagonal Columns and Plates
Light Scattering Calculation	IGOM + ADDA	IGOM + IITM
Particle Size Distribution	Gamma ($v_{eff} = 0.1$)	Gamma ($v_{eff} = 0.1$)
Effective Diameter	$D_{eff} = 60$ μm	$D_{eff} = 60$ μm
Scattering Angle	60° to 160°	90° to 160°
Variance of EOF 1 and 2	99.3 %	88.4%
Parameterization	x_1, x_2	x_1, x_2, ρ
Cloud Optical Thickness	Fixed at $\tau = 5$	Retrieved
Cloud Top Height	Retrieved	Provided from MODIS product
PARASOL Channels	3 Polarization channels	1 Non-polarization + 1 polarization channels

4.3.3 Stage 2-1: Satellite data

This study uses the single-pixel data set in the PARASOL Level 1B product. The nominal resolution of the nadir pixel is 6 km × 6 km. In the retrieval described in Section 4.4, data from three polarization channels (0.49 μm, 0.67 μm, and 0.865 μm) are used, while one polarimetric channel (0.865 μm) and one non-polarimetric channel (0.865 μm) are used in the retrieval in Section 4.5. In addition to the PARASOL reflectivity data, data from the Moderate Resolution Imaging Spectroradiometer (MODIS) and Atmospheric Infrared Sounder (AIRS) sensors aboard the Aqua satellite are used as ancillary data. The Aqua and PARASOL satellites were flying in formation between 2005 and 2009.

The MODIS Collection 6 Level 2 cloud product (MYD06) provides cloud top temperature and thermodynamic phase that are used to select the pixel suitable for the analysis, and AIRS Level 3 data provides a monthly mean ozone concentration that are used to account for absorption by ozone that reduces reflectivity at visible wavelengths.

The PARASOL Level 1B radiometric data is first collocated with the MODIS Level 2 cloud product (Platnick et al., 2017) to select pixels containing ice clouds. Only PARASOL pixels that have corresponding MODIS observations are selected and filtered by the criteria summarized in Table 4.2. The filtering process is utilized to avoid cloud edge contamination, to avoid supercooled water droplets, and to select pixels where clouds are optically thick. The selection criterion of 208 K used in Model A is a threshold used to identify convective precipitation in the tropics (Mapes and Houze,

1993). The analysis is applied only over oceans so the influence of surface reflection is minimal.

A "pixel" in the PARASOL Level 1 product contains reflectivity data observed from up to 16 viewing angles. An individual reflectivity value stored in a pixel is called a "view", and we select valid views using criteria on scattering angle and sunglint angle (see Table 4.2). When five or more valid views are contained in a pixel that satisfy all pixel criteria previously mentioned, the pixel is marked as valid, and the roughness inference is attempted.

Table 4.2. PARASOL pixel and view selection criteria.

Parameters	Applied to	Model A	Model B
MODIS Infrared Cloud Phase	Pixel	Ice	Ice
PARASOL Ocean/Land Flag	Pixel	Ocean	Ocean
Number of Valid Views	Pixel	At least 5	At least 5
Brightness Temperature at 11 μm	Pixel	less than 208 K	N/A
Heterogeneity Index H_σ	Pixel	N/A	Less than 5
Scattering Angle	View	60° to 160°	90° to 160°
Sunglint Angle Threshold	View	30°	35°

4.3.4 Stage 2-2: Maximum likelihood estimation

In the second stage of the two-stage retrieval, the retrieval parameters are determined so that the forward model most closely simulate the satellite measurements. The simple but powerful maximum likelihood method with a normal error distribution is appropriate for our problem because we have little knowledge about the distribution of

parameters (EOF scores). As each pixel typically contains five to eight valid views at two or three channels, the number of observations in each pixel ranges from 10 to 24.

The standard deviation (SD) and correlation (Corr) of inferred parameters are calculated in the framework of maximum likelihood estimation, and used to avoid under-constrained inferences. The pixel is rejected if $SD(x_1) > 0.02, SD(x_2) > 0.02, Corr(x_1, x_2) > 0.3$ for Model A, and $SD(x_1) > 0.2, SD(x_2) > 0.2, Corr(x_1, x_2) > 0.3$for Model B. The standard deviation and the correlation depend strongly on the observation geometry and particle model and are almost independent of the observed polarized reflectivity. Therefore, this rejection process can be interpreted as the refinement of pixels based on the information content to achieve a reliable inference.

The error distribution is confirmed to be normal (see Section 4.2.2), so if the problem is not strongly nonlinear, the parameters' error distributions are expected to be normal as well (Rodgers, 2000). As expected, Fig. 4.12 demonstrates that the application of the maximum likelihood method with synthetic L_{np} data results in a symmetric distribution about the EOF 1 score corresponding to the true roughness parameter $\sigma^2 = 0.15$. The distribution is not strictly normal because the number of observations in each pixel varies, but the error distribution of each pixel is theoretically derivable, as well as the confidence interval. The detailed description of Fig. 4.12 is provided in Section 4.4.1.

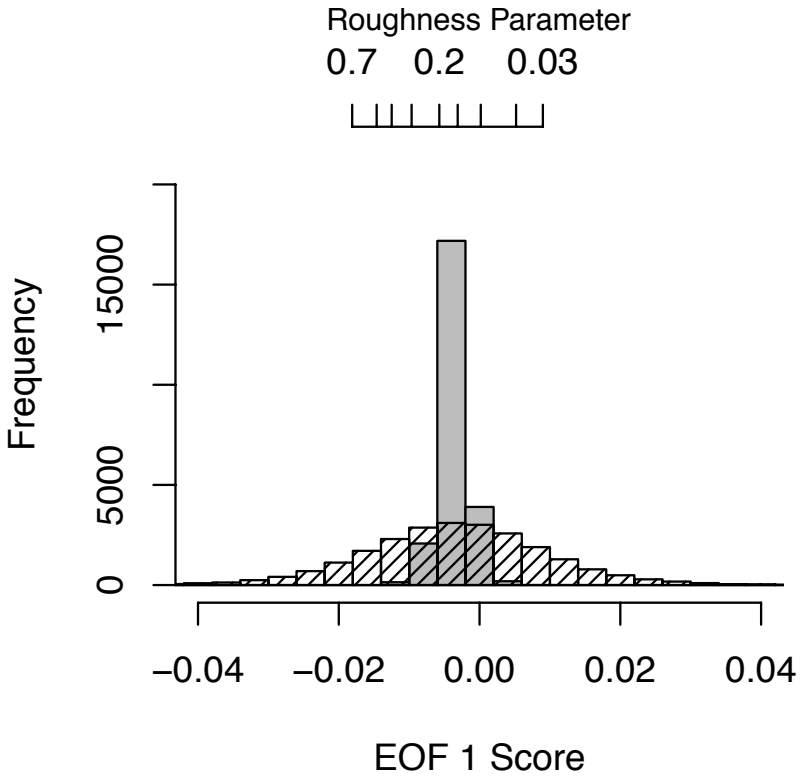

Fig. 4.12. The distribution of inferred EOF 1 scores for synthetic data. The solid bars correspond to retrieval without random measurement noise and the hatched bars correspond to retrieval with measurement noise. The distribution for the noise-added synthetic data is symmetric about the EOF 1 score corresponding to the true roughness. The median of EOF 1 score is -0.00336, corresponding to roughness parameter of $\sigma^2 = 0.14$.

4.4 Results from fixed-shape roughness retrieval (Model A)

4.4.1 Interpreting EOF 1 scores as roughness parameter

As the EOF 1 score is a monotonic function of the roughness parameter and explains most of the $-P_{12}$ variation (85.6%), it can be considered as an effective roughness parameter for the column aggregate shape. The relation between EOF 1 scores and the natural logarithm of roughness parameters is nearly linear (Fig. 4.13), indicating

that the roughness parameter can be subsequently inferred after the inference of the EOF 1 score. The straight line in Fig. 4.13 is the regression line defined in the form:

$$\sigma^2 = \exp[-115.755x_1 - 2.3543]. \tag{4.10}$$

As the roughness parameter computed from Eq. (4.10) does not account for the variation of EOF 2 score, it is inaccurate for the mixture of particles containing multiple degrees of roughness. Equation (4.10) is introduced to compare our retrievals to the conventional discrete parameter space.

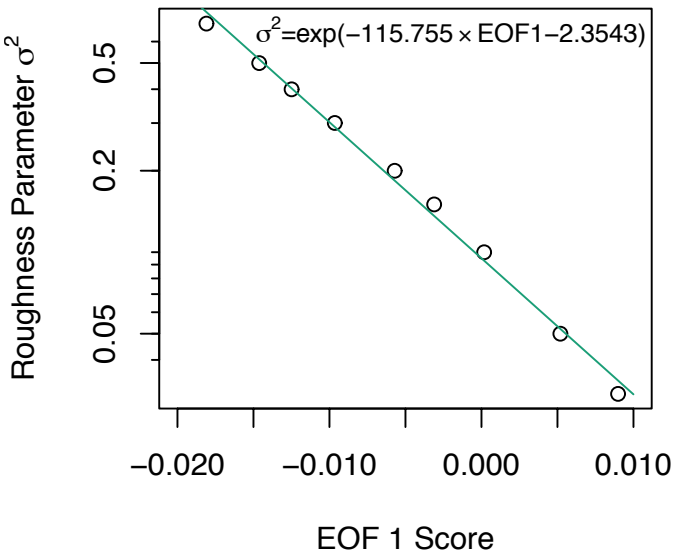

Fig. 4.13. The relation between the particle roughness parameter and the EOF1 score. The natural logarithm of the particle roughness parameter is nearly linear to the EOF 1 score. This implies that the particle roughness can be directly inferred from the EOF 1 score.

An example of the synthetic retrieval is shown in Fig. 4.12. The generation of synthetic data and the retrieval are based on Model A, and observation angles from three

polarimetric channels (0.49 μm, 0.67 μm, and 0.865 μm) are used. The synthetic data is generated by adding random noise following the normal distribution with error variance 1.35×10^{-6} (PARASOL noise level determined in Section 4.1.2). The median of the inverted EOF 1 score is –0.00336 and the corresponding roughness parameter is $\sigma^2 = 0.14$. The interquartile range of the EOF 1 score distribution is $[-0.01146: 0.00476]$, which corresponds to the roughness parameter range of $[0.05: 0.36]$. The result indicates that our approach has a practical skill in estimating the particle roughness parameter out of observations superimposed with noise. This resilience to the instrumental noise is a remarkable contrast with the traditional "best-fit" approach (cf. Fig. 4.1).

The distribution of the χ^2 values for the synthetic retrieval is presented in Fig. 4.14. The χ^2 value is a variance-normalized residual squared sum that is defined for each pixel, and follows the χ^2 distribution with degrees of freedom of N_d if the inversion is successful, where N_d is the observational degree of freedom minus degree of freedom of parameter (approximately, the number of observations minus 3 in the retrieval). As the χ^2 distribution of N_d degrees of freedom has a peak about N_d, the distribution of the χ^2 value indicates whether the inversion is successful. If the location of the peak of a distribution of χ^2 values is smaller than N_d, the observation error may be overestimated, and if the location of the peak is larger than N_d, the observation error is underestimated, or the forward model does not represent reality (Rodgers, 2000). The distribution in Fig. 4.13 has a peak at about 12, and very few pixels have a χ^2 value over 40. This is a reasonable distribution because the number of observations ($\approx N_d$) is about

15 to 24 for most pixels. Because the 95th percentile for the χ^2 distribution with 24 degrees of freedom is 36.42, it is no surprise that very few pixels have a χ^2 value over 40.

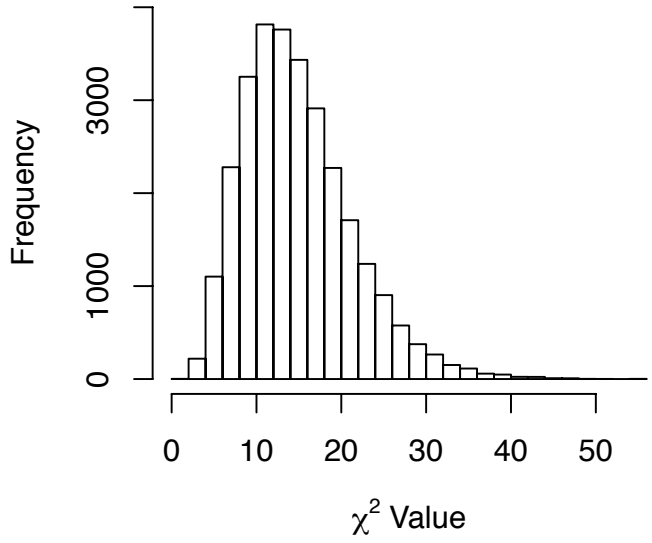

Fig. 4.14. Frequency distribution of the χ^2 values (variance-normalized residual square sum). The distribution has a peak at about 12, tapering to nearly zero at approximately 40. This is a reasonable distribution because most pixels contain 15 to 24 observations.

Figures 4.12 and 4.14 demonstrate the validity of our inference framework under an idealized situation, where the error distribution and the true roughness parameter are constant. In application to actual satellite data, however, the true roughness parameter varies from pixel to pixel while the error distribution stays the same. Therefore, the distribution of the EOF 1 score must be more spread out as a result of convolution of the error distribution and the true roughness parameter distribution. In contrast, the χ^2

distribution is expected to be about the same. The result of the application to actual data is given in the next section.

4.4.2 Roughness parameter of cold ice cloud over oceans

With the cloud selection criteria listed in Table 4.2, 79192 pixels based on one month of collocated PARASOL/MODIS data over oceans during September 2005 were selected for inversion. The information content was sufficient for full analysis of 23359 pixels, for which results are presented in this section.

The histogram of the inferred EOF 1 score is presented in Fig. 4.15 for the extratropical (latitude > 30°) oceans. The width of the histogram in Fig. 4.15 is broader than the monodispersive roughness case (Fig. 4.12), indicating significant variability in the microphysical properties of clouds. The median of the distribution is –0.0293, corresponding to a surface roughness parameter of 2.82. The interquartile range of the EOF 1 score is [–0.0429:–0.0165], implying 50% of the data is within the roughness parameter (σ^2) range of [0.65:13.6]. The result supports the use of the roughened particle model in extratropical ice cloud retrievals as suggested by previous studies. While our analysis is limited to very cold ice clouds over ocean, the validity of using roughened crystals in the MODIS Collection 6 ice model is supported, although further explorations into warmer and optically thinner clouds are desirable. In general, cloud particles become more complex as the cloud temperature increases (Heymsfield, 2002), thus we expect more roughened particles in warmer clouds that are not included in our analysis.

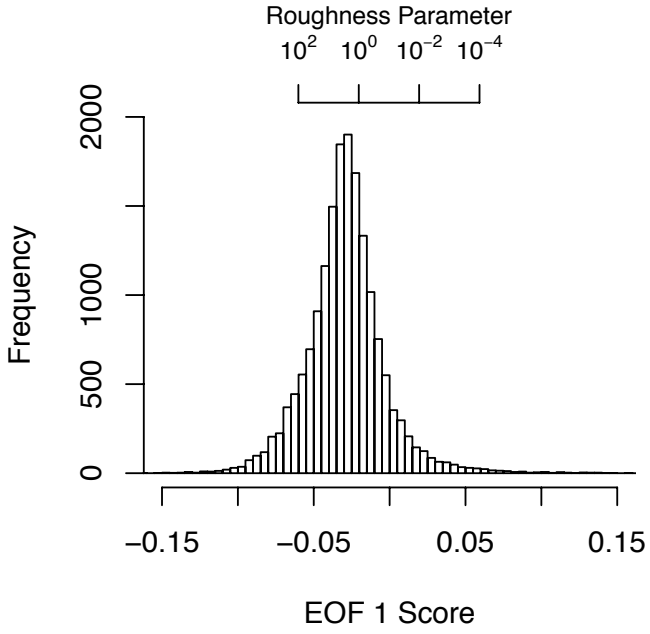

Fig. 4.15. The distribution of EOF 1 scores (retrieval results). Data are obtained from cold ice clouds over extratropical oceans during September 2005. The median of the EOF 1 score is –0.0293, corresponding to a roughness parameter of 2.82. Consistent with previous studies, roughened particles better simulate the measured polarized reflectivity.

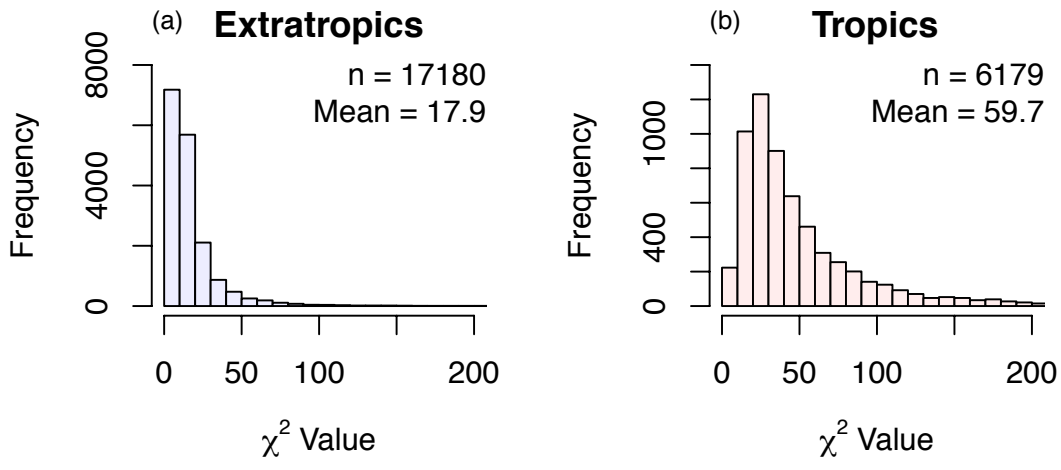

Fig. 4.16. Distributions of χ^2 values in the tropics and extratropics. The distribution of the χ^2 value in the tropics (b) implies that the forward model is not correctly simulating the reflectivity in the tropics, while the distribution of the χ^2 value in the extratropics (a) indicates successful inversion.

The distributions of the χ^2 value in the tropics and extratropics are separately presented in Fig. 4.16. As discussed in the previous section, the distribution of χ^2 values indicates the validity of the inversion. While the distribution of the χ^2 values in the extratropics shows reasonable behavior (Fig. 4.16a), the distribution of the χ^2 values in the tropics has a very long tail with the mean χ^2 being 59.7, which is unacceptably large (Fig. 4.16b). This long tail implies that our forward model does not properly reproduce the observed L_{np} field in the tropics, presumably because some underlying assumptions are not appropriate or the information content is not enough. Some possibilities that violate our underlying assumptions include sub-pixel scale cloud heterogeneity, the presence of ice particles with other habits or aspect ratios, their vertical heterogeneity, cloud 3-D effects, and the effect of aerosols.

4.4.3 Unexpectedly large roughness values in the extratropics

As the roughness parameter of 2.82 lies outside of our prescribed roughness parameter range (0 to 0.7), it is an estimate by extrapolation. Yet, this projection of roughness parameter implies that the conventional degree of roughness may not be sufficient to represent actual cloud particles with the aggregate column model. The proportion of pixels that contains inferred roughness parameter $\sigma^2 > 0.7$ is 74%, which also indicates the limit of this particle shape. As the accuracy of roughness approximation for such a large roughness parameter is questionable, a particle shape that can fit observations with less intense roughening may be suitable for the representation of natural clouds.

To attribute the cause of unphysically large roughness value in the extratropics, the same retrieval process is repeated assuming three additional particle shapes. Figure 4.17a shows the original inference with aggregate of columns shape, in which the observation density peaks away from the line connecting 10 points that corresponds to prescribed roughness values. The aggregate of plates (Fig. 4.17d) performs worst among the tested particles, and the solid bullet rosette shape (Fig. 4.17c) shows the largest overlap of parameter space and observation density. These results indicate that the

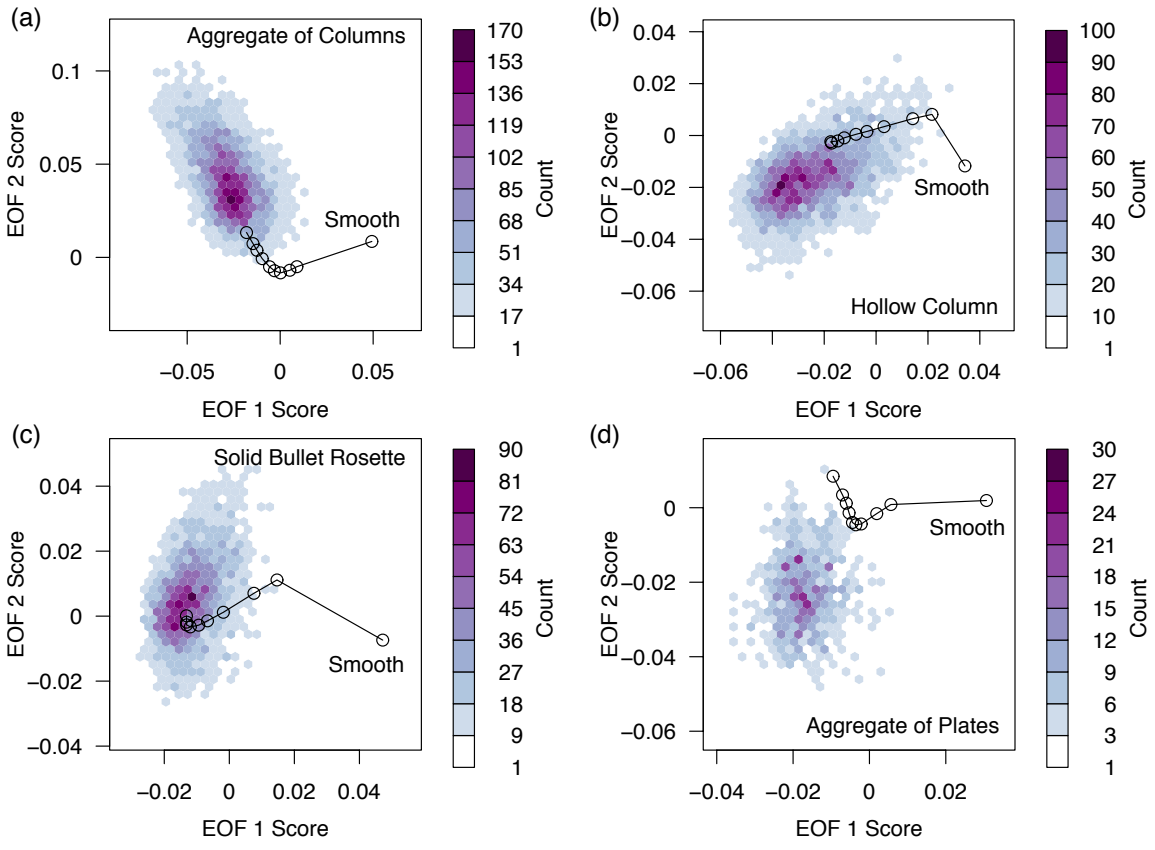

Fig. 4.17. Distributions of EOF 1 and EOF 2 scores with different particle shapes. The observation frequency is shaded with color, and the solid line connects the EOF scores for 10 prescribed roughness values (circles). (a) The result of inference with aggregate of columns, (b) hollow column, (c) solid bullet rosette, and (d) aggregate of plates.

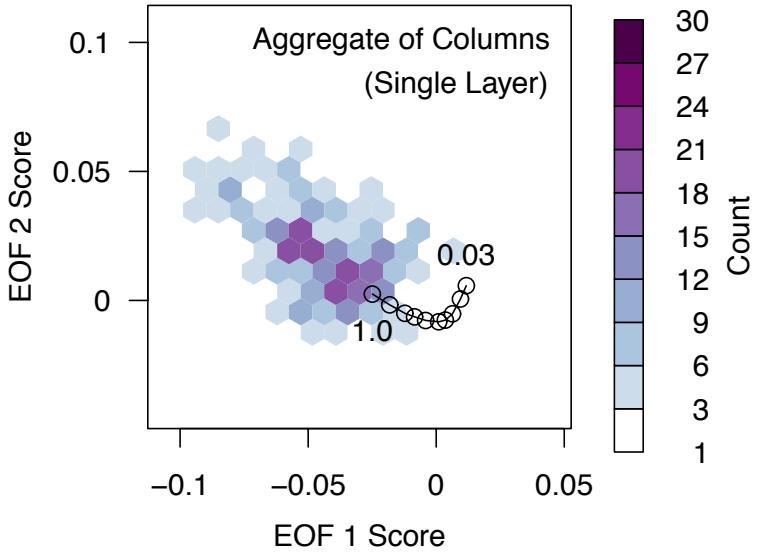

Fig. 4.18. CALIOP-filtered retrieval results. CALIOP data are used to filter out clouds with multiple layers or with aerosols above the cloud. The observation frequency is color shaded, and the EOF scores for column aggregate particles (circles) are connected by a line. This analysis is conducted on a different EOF space from Fig. 4.7. The minimum degree of roughness is $\sigma^2 = 0.03$ and the maximum is $\sigma^2 = 1.0$. To exclude optically thin clouds, pixels are selected if the CALIOP vertical feature mask product marks total attenuation above ground. No temperature threshold is applied.

roughness retrieval is sensitive to an assumed particle shape.

We also investigated the contamination by multi-layer clouds and aerosol above clouds by collocating the Cloud-Aerosol Lidar with Orthogonal Polarization (CALIOP) vertical feature mask and cloud layer products. As September 2005, which is analyzed in this study, is before the launch of the CALIPSO satellite, we analyzed the collocated POLDER3-MODIS-CALIOP dataset in September 2006 in the extratropics. According to the CALIOP vertical feature mask, on the CALIOP track, about 20% of pixels that are colder than the brightness temperature threshold of 233K are possibly contaminated by either multi-layer cloud, aerosol above clouds, or a stratospheric feature. However, the

distribution of the retrieved EOF scores is approximately the same even when assuring the absence of aerosol above cloud and limiting the analysis to single-layer clouds (Fig. 4.18). Therefore, we do not consider that aerosol contamination and multi-layer clouds introduce a large bias that brings our estimate out of the range of prescribed parameters. Removal of the multi-layer clouds helps to reduce the number of pixels with very large χ^2 values.

4.5 Results from variable-shape analysis (Model B)

Finding that the column aggregate model does not necessarily perform the best for cold extratropical clouds over oceans as described in Section 4.4, I apply the two-stage method to a larger parameter space. The parameter space in Model B is constructed to cover the hexagonal column and plate shapes (aspect ration from 1/9 to 9) with surface roughness between $\sigma^2 = 0.01$ to 1. Single-element hexagonal column particles are selected because previous studies show that the phase functions of a single-element particle and the aggregate of it look similar (Um and McFarquhar, 2007, 2009; van Diedenhoven et al. 2012). However, the mean backward scattering of the aggregate shape is usually stronger and the asymmetry parameter is smaller. To incorporate the effect of aggregation, Model B retrieves the mean backward scattering simultaneously. Since a sensitivity study showed that the information content is not sufficient to retrieve three parameters only with polarization channels, I added a non-polarization channel. In addition, two changes are made to the retrieval system: (1) Cloud top pressure is no longer a retrieval parameter and is extracted from the MODIS cloud product. This simplifies the retrieval system so that it uses only one channel (0.865 μm) with and

without polarization. (2) The ozone absorption is not varied because the effect is negligible for the 0.865 μm channel.

4.5.1 Retrieval results

Figure 4.19 shows the retrieval results with Model B in the extratropics and in the tropics. The extratropical result for EOF 1 Score (x_1) and EOF 2 Score (x_2) is centered near the (x_1, x_2) corresponding to a long column particle (aspect ratio 1), as shown in Fig. 4.19(a) with surface roughness $\sigma^2 = 0.2$ (between $0.1 < \sigma^2 < 0.5$). However, the distribution of (x_1, ρ) in Fig. 4.19(b) is along the straight line for severely roughened particles. This result presumably indicates that the anisotropic reflection from the cloud is best simulated with the long column particles, but the observed mean backscattering is stronger than the computation with long column particles. One possible interpretation of this result is the presence of solid bullet rosette particles or aggregate of long column particles that have higher mean backward scattering than the single-element column particles. Another possibility is that the retrieval is contaminated by the factors that are not accounted for in the current framework of the analysis.

The tropical data in Fig. 4.19 (c,d) has the observation density peak outside of the prescribed parameter range, and implies that the forward model does not represent the measurement properly, or the retrievals have failed because of the limited information content. The sampling of phase functions in the tropics are limited to $\Theta > 110°$ as indicated in Figure 4.20. Figure 4.21 shows that the first and second EOFs are smooth increasing and decreasing functions at $\Theta > 130°$, and there is a possibility that some

measurements cannot tell the difference between two EOFs. The failure in the tropics is consistent to the retrieval in Model A.

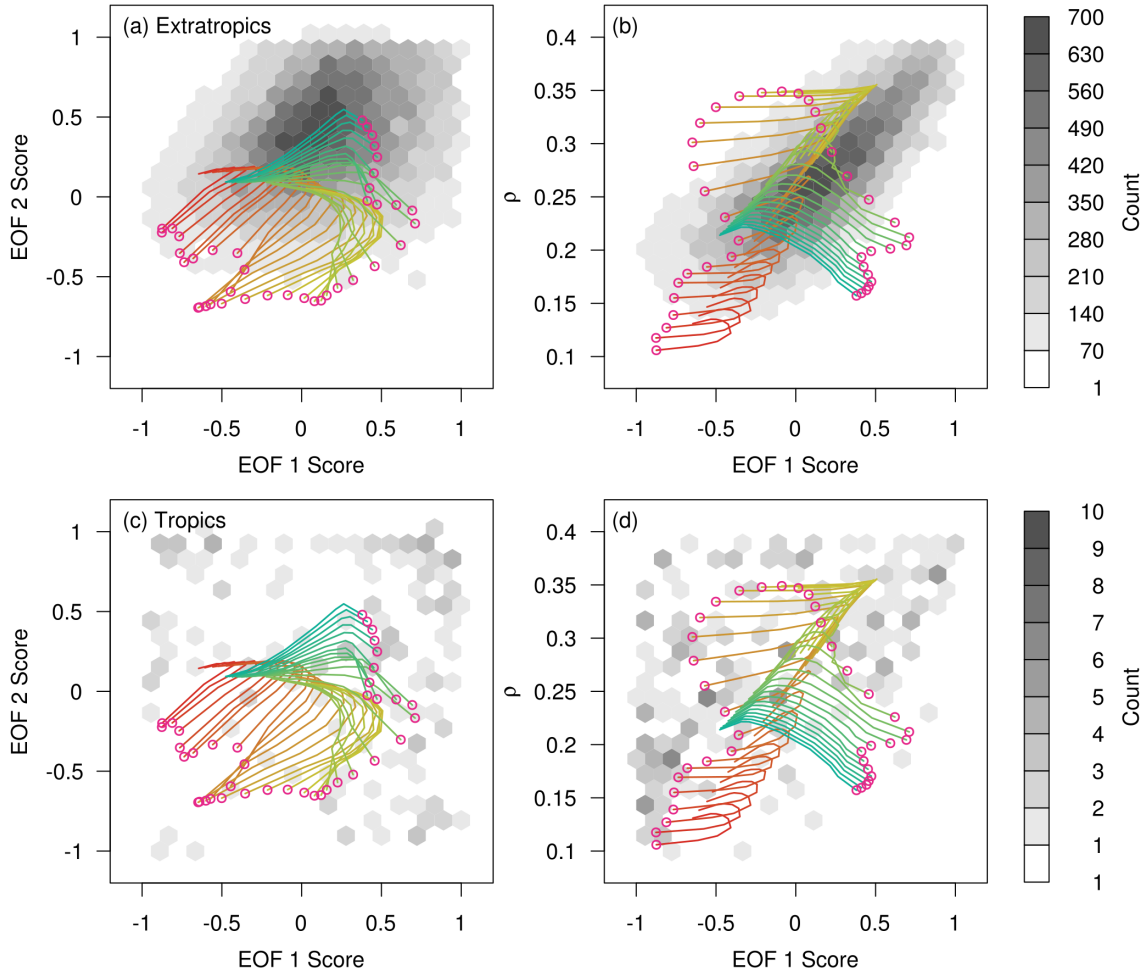

Fig. 4.19. Retrieval results for Model B (hexagonal column and plate particles with varying degree of surface roughness). (a) and (b) are for the extratropics, and (c) and (d) are for the tropics.

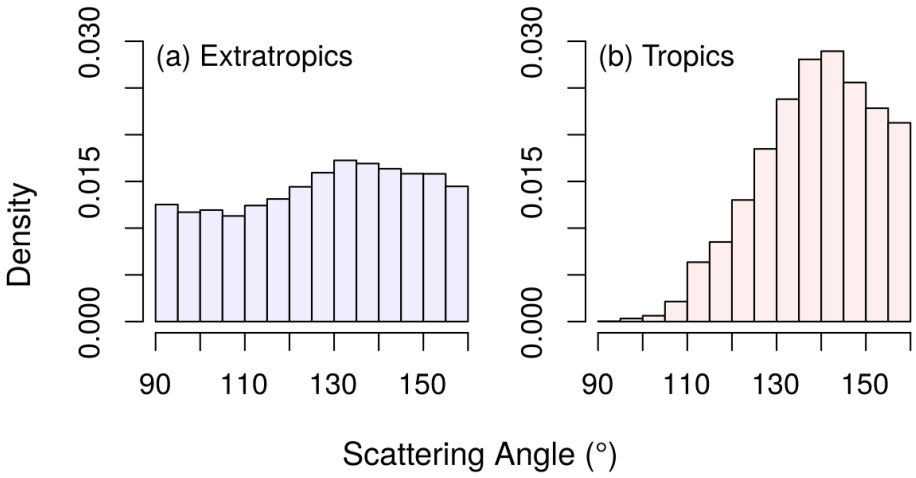

Fig. 4.20. The distributions of scattering angle sampling in the tropics and extratropics.

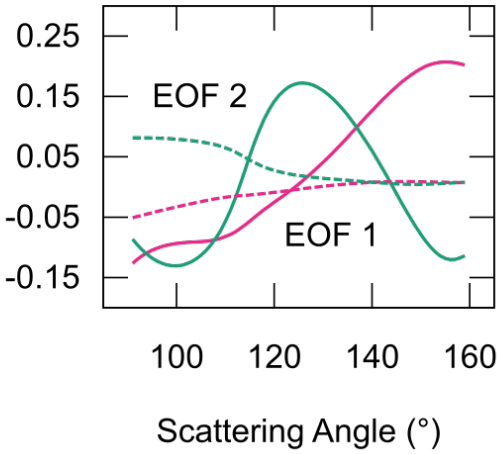

Fig. 4.21. First and second EOFs for Model B. Solid lines are for the phase function ($\mathcal{P}$) and the dotted lines are for $-P_{12}$ element of the phase matrix (primarily responsible for the polarization from the cloud).

4.5.2 Interpretation of the discrepancy

Interpretation of the extratropical data is attempted in this section with focuses on the cloud 3-D effect and horizontally oriented particles. The cloud 3-D effect decreases the reflectivity strongly when the scattering angle is small. This is because

measurements at small scattering angles are made when the instrument looks at the shadowed side of the cloud. This results in the overestimation of EOF 1 values because the first EOF is an increasing function of scattering angle, as shown in Fig. 4.21. Assuming that the polarized reflectivity is less affected by the 3-D effect, EOF 2 may also be overestimated to keep the polarized reflectivity pattern. Figure 4.22 supports this hypothesis as the center of the distribution moves to large x_1 and x_2 when H_σ>2.5. However, even for $H_\sigma < 0.5$, the discrepancy between (x_1, x_2) and (x_1, ρ) distributions are noticeable (Fig. 4.22a, b).

Another possibility is the effect of quasi-horizontally oriented particles. Natural ice particles are anticipated to be quasi-horizontally oriented because of aerodynamic forces (Sassen, 1980), and Noel and Sassen (2005) and Marshak et al. (2017) confirmed the presence quasi-horizontally oriented particles observationally. The effects of oriented particles to total and polarized reflectivity are studied by Masuda and Ishimoto (2004), and they conclude that the effect is significant near the direction of specular reflection even when the standard deviation of the tilt angle reaches 20°. Figure 5c in Masuda and Ishimoto (2004) demonstrates that the reflectivity increases in the direction of specular reflection, and decreases in other directions. The specular reflection in the extratropics occurs when the satellite looks toward the equator, and the scattering angle is $180° - 2\theta_0$. As the results in Fig. 4.19 (a,b) are for extratropical data in September, specular reflection occurs in $\Theta < 120°$. The direction of specular reflection is masked by the glint angle condition, and the suppression of reflectivity may result in the overestimation of x_1. Previous studies show that the concentration of quasi-oriented particles increase with

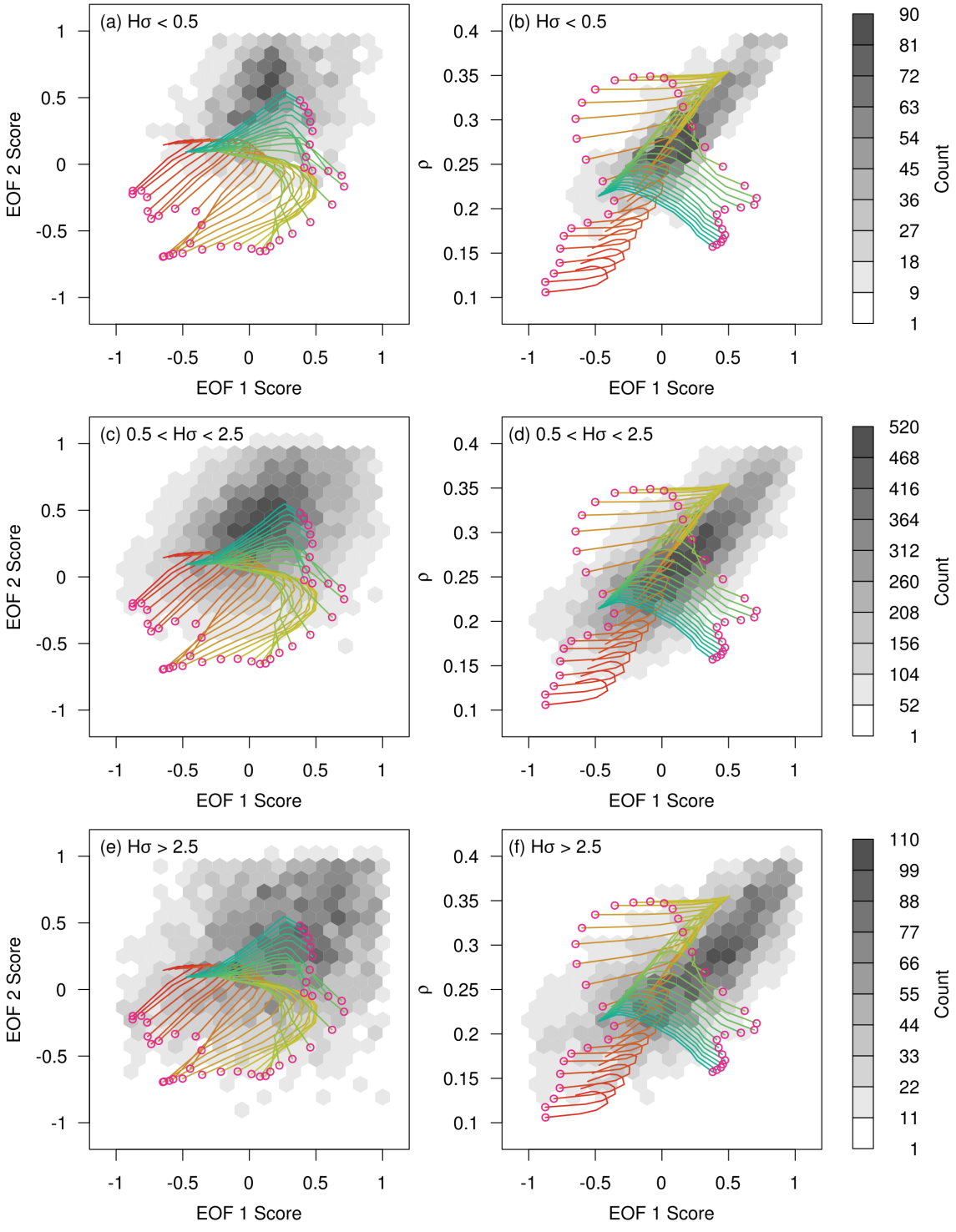

Fig. 4.22. The extratropical retrieval results stratified by H_σ value.

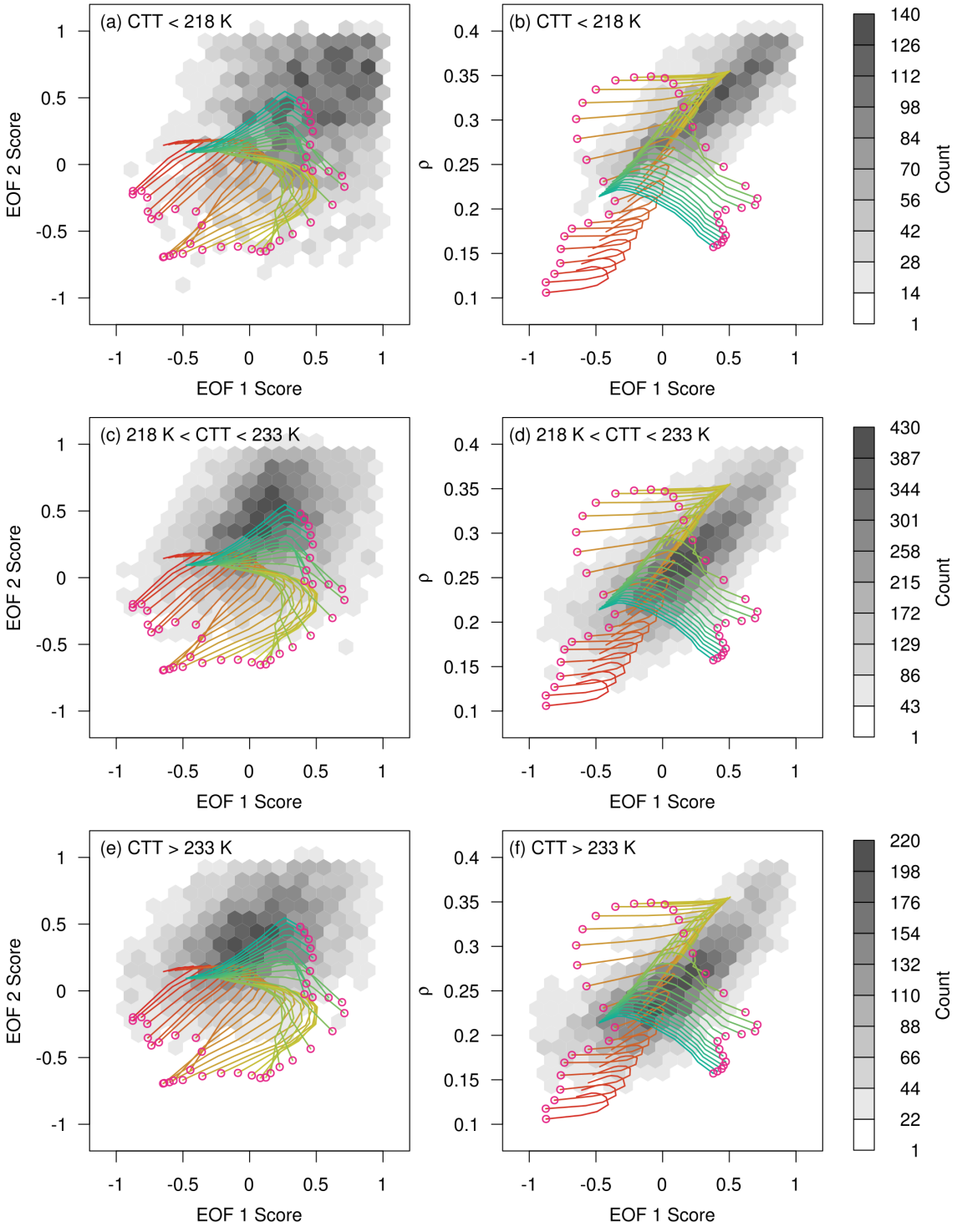

Fig. 4.23. The extratropical retrieval results stratified by cloud top temperature. The cloud top temperature is from the MODIS Level 2 cloud products.

increasing temperature, and the temperature stratification (Fig. 4.23) shows the same trend from what is anticipated from the effect of quasi-horizontally oriented particles. However, the fraction of quasi-horizontally oriented particles for cold ice clouds (i.e. viewed by satellite sensors) is less than 1% (Noel and Sassen, 2005; Zhou et al. 2012), and the actual magnitude of the effect is uncertain. When the effect of quasi-oriented ice particle is small, Figure 4.23 indicates that the surface roughness increases with increasing cloud top temperature.

4.4 Conclusions

In this study, the particle roughness parameter of thick ice clouds over oceans is inferred by employing a new framework that is resilient to the observational error. The distinct feature of the framework is the continuous parameter space that is constructed with an empirical orthogonal function (EOF) analysis. Two EOFs are found to be sufficient to explain the variation of $-P_{12}$ with a changing particle roughness parameter, substantially reducing the number of parameters for the forward model.

From unpolarized cloud reflection at a scattering angle of 170°, the observational error of the PARASOL data is empirically estimated. Supported by the error analysis with parametric bootstrapping, the maximum likelihood method is applied to the inverse problem. The method provides error estimates and correlations for inverted parameters, which are unavailable with the "best-fit" approach used in the previous studies. To correctly incorporate the effect of atmospheric Rayleigh scattering, the cloud-top height is inferred simultaneously.

The application of the present method to cold ice clouds over extratropical oceans results in a roughness parameter of 2.82, implying that the use of the roughened particle model is suitable for cloud property retrievals. Additional analysis with three other particle shapes indicates that solid bullet column models may be more appropriate to represent cold ice clouds over extratropical oceans.

With the analysis employing extended parameter space, moderately to severely roughened ($0.1 < \sigma^2 < 0.5$) long column particles represent the shape of the observed phase function the best, while the mean backward scattering may be underestimated. The cloud 3-D effect may affect the retrieval results, but aggregates of long column particles or solid bullet rosette shapes are recommended to mimic clouds with 1-D radiative transfer calculations. Slight temperature dependence of the shape is seen, implying surface roughness increases with increasing surface roughness with increasing cloud top temperature.

5 ESTIMATION OF PHASE FUNCTION

The implication from the EOF-based two-stage approach in Section 4 is that ice cloud reflectivity in the extratropics shows maximum consistency with roughened hexagonal long column particles, and presumably an aggregate of these, including bullet rosettes. However, it is not appropriate to conclude that ice clouds consist of those particles because the center of the observation density distribution is out of the prescribed range of parameters. The results indicate that the phase function may not be completely reproduced by the mixture of hexagonal column and plate particles. In addition, the number of reliable data in the tropics is limited.

The rest of section introduces a new phase function inference technique based on approximate radiative transfer calculations and presents the result of inference from Multi-angle Imaging Spectroradiometer (MISR) data to supplement the results obtained in Section 4.

5.1 Introduction

This section revisits notable previous studies related to the validation of particle model using multi-angle intensity measurements from satellite sensors. I illustrate that the particle model validation techniques developed in early years require the knowledge of cloud optical thickness, but the later techniques do not. The new inference technique described later is based on these techniques, but further the theory and approximation to infer shape of phase functions.

An early application of multi-angle measurements to infer an appropriate particle shape was attempted by Baran et al. (1998) with the ATSR-2 instrument. They utilized the ratio of reflectivity from two viewing angles, and found that a polycrystalline shape is the most appropriate among the shapes they tested. Chepfer et al. (1998) conducted a similar study with the airborne version of the Polarization and Directionality of the Earth's Reflectance (POLDER) sensor.

These authors chose some realistic particle shapes to compute the single scattering albedos and phase functions, and used the computed single scattering properties to compute the reflectivity at multiple viewing directions with radiative transfer models. They compared the results to the measurements, and the best-fit particle model was considered to be the most appropriate particle shape for the ice cloud. Their approach requires prior knowledge about the optical thickness.

To validate the consistency of multi-angle intensity simulations with measurements without prior knowledge of the optical thickness, Doutriaux-Boucher et al. (2000) proposed the spherical albedo difference (SAD) method. The method defines SAD as the deviation of retrieved spherical albedo in a particular viewing direction from the mean averaged across all viewing directions. As the retrieved spherical albedo depends on an assumed phase function in the forward radiative transfer calculation, the SAD values indicate the difference of anisotropy between the model and measurements. If the assumed phase function is consistent with the actual phase function the SAD values become zero at all scattering angles. Utilizing the SAD method, later studies with the POLDER sensor and the Multiangle Imaging Spectroradiometer (MISR) sensor

show that irregular particle shapes or particles with a high degree of surface roughness are representative models for ice particles at the global scale (Chepfer et al., 2001; C.-Labonnote et al., 2001; Baran and C.-Labonnote, 2006, 2007; McFarlane et al., 2005).

The basic objective of work presented in this section is to semi-analytically estimate the phase function that explains the ice cloud reflectivity observed by the MISR over ice-free ocean and to determine the combination of particle shape and the degree of surface roughness that realizes such phase function. The MISR has 9 fixed "push broom" cameras that record lines of pixels across the satellite track (Diner et al. 1998). The cameras measure the intensity of reflected sunlight at each location over approximately 7 minutes at these angles along the ground track: 70.5°, 60°, 45.6°, and 26.1° forward (cameras Df, Cf, Bf, Af), nadir (camera An), and 26.1°, 45.6°, 60°, 70.5° aft (cameras Aa, Ba, Ca, Da). Camera pixels (275 m at nadir) are averaged over 4 × 4 pixels as data pixels (1.1 km at nadir).

A semi-analytical method described in this study is a modified version of the SAD method and inspired by a property of SAD that it is related to the difference between assumed and actual phase functions. This paper focuses on the results from the MISR sensor, but the same principle is applicable to any multi-angle intensity measurements. Section 5.2 introduces the principles of our phase function estimation. Section 5.3 describes the implementation of the principle, and Section 5.4 presents results from the application to MISR data. Discussions and concluding remarks are given in Section 5.5 and 5.6.

5.2 Principles of the phase function estimation

The semi-analytical technique developed in this study estimates the phase function of a collection of ice particles in clouds. The fundamental assumption in the method is that in-cloud radiance is approximately a sum of the forward-traveling component and azimuthally-independent component. This assumption enables us to derive an analytical expression to estimate an unknown phase function as a difference from a known phase function. As the accuracy of the estimation is high when the known phase function is close to the unknown phase function, our retrieval system consists of three steps: (1) select satellite pixels that qualify for the estimation, (2) estimate the unknown actual phase function with precomputed 39 known phase functions in each viewing direction in every pixel, and (4) select the most appropriate phase function by checking the consistency at a large scale.

In Section 5.2, the derivation of the analytical expression is discussed, whereas the application of the method to the actual data is documented in Section 5.3. Section 5.2.1 describes the approximation of in-cloud radiance we use in our method, and Section 5.2.2 derives a fundamental formula of our phase function estimation.

5.2.1 Approximating radiance

Under the assumption of a single layer ice cloud with optical thickness τ_C in a plane parallel homogeneous atmosphere, the optical thickness and the measured satellite radiance satisfy the formal solution of the radiative transfer equation as follows:

$$\mu\left[I\left(0,\vec{\Omega}\right)-I\left(\tau_C,\vec{\Omega}\right)e^{-\frac{\tau_C}{\mu}}\right]=\int_0^{\tau_C}e^{-\frac{\tau'}{\mu}}\frac{\varpi}{4\pi}\iint_{4\pi}I\left(\tau',\vec{\Omega}'\right)\mathcal{P}\left(\vec{\Omega},\vec{\Omega}'\right)d\vec{\Omega}'\,d\tau', \qquad (5.1)$$

where μ is the cosine of the viewing zenith angle and $I(\tau', \vec{\Omega})$ is the radiance propagating into the viewing direction $\vec{\Omega}$ in the cloud at the optical depth τ'. The phase function of a collection of cloud particles is $\mathcal{P}(\vec{\Omega}, \vec{\Omega}')$, and the single scattering albedo is ϖ. On the right-hand side, the double integral represents a 2-D integration with respect to all directions $\vec{\Omega}'$, and the outermost integral represents an in-cloud integration with respect to optical depth τ'. All quantities with a prime are integration variables. Note that the estimated phase function from this study is an "effective" phase function that includes contributions from cloud heterogeneity and 3-D effects because the framework of this theory is based on plain-parallel homogeneous atmosphere.

We hereby introduce an approximation that the in-cloud radiance is the sum of a forward-traveling component and azimuthally-independent component. This approximation is expected to be accurate within and below the diffusion domain of clouds (azimuthally-independent component) as well as at the top of clouds where strong light beam is concentrated in the solar direction due to the strong forward scattering by cloud particles (forward-traveling component). With this approximation, the in-cloud radiance in an arbitrary direction $\vec{\Omega}'$ becomes:

$$I(\tau', \vec{\Omega}') = C(\tau', \mu_0)\left[4\pi\delta(\vec{\Omega}', \vec{\Omega}_0)s(\tau', \mu_0) + [1 - s(\tau', \mu_0)]\sum_{l=0}^{\infty} c_l(\tau')P_l(\mu')\right] + \varepsilon_1, \quad (5.2)$$

where $C(\tau', \mu_0)$ is the approximate actinic flux, $\vec{\Omega}_0$ is the solar direction, μ_0 is the cosine of the solar zenith angle, $s(\tau', \mu_0)$ is the partitioning factor that divides the in-cloud

radiance into the forward-traveling term and the azimuthally-independent term, $P_l(\mu')$ is the Legendre polynomial of degree l, $c_l(\tau')$ is the expansion coefficient ($c_0 = 1$), and ε_1 is the error of this approximation. $\delta(\vec{\Omega}', \vec{\Omega}_0)$ is the Dirac delta function satisfying

$$f(\vec{\Omega}_0) = \frac{1}{4\pi} \iint_{4\pi} 4\pi\delta(\vec{\Omega}', \vec{\Omega}_0) f(\vec{\Omega}')\, d\vec{\Omega}' \tag{5.3}$$

for an arbitrary function $f(\vec{\Omega})$. Integrating both sides of Eq. (5.2) with respect to $\vec{\Omega}'$, we find that that the function $C(\tau', \mu_0)$ is indeed the approximate actinic flux:

$$\frac{1}{4\pi} \iint_{4\pi} I(\tau', \vec{\Omega}')\, d\vec{\Omega}' = C(\tau', \mu_0) + \iint_{4\pi} \varepsilon_1\, d\vec{\Omega}'. \tag{5.4}$$

In summary, the approximation in Eq. (5.2) expresses the in-cloud radiance at optical depth τ' as a product of approximate actinic flux $C(\tau', \mu_0)$ and the linear combination of a delta function and an azimuthally-independent function.

Substituting Eq. (5.2) into $I(\tau', \vec{\Omega}')$ in the double integral of Eq. (5.1), the double integral can be rewritten as follows:

$$\begin{aligned} &\frac{1}{4\pi} \iint_{4\pi} I(\tau', \vec{\Omega}') \mathcal{P}(\vec{\Omega}, \vec{\Omega}') d\vec{\Omega}' \\ &\quad = C(\tau', \mu_0) s(\tau', \mu_0) \mathcal{P}(\vec{\Omega}, \vec{\Omega}_0) \\ &\quad + C(\tau', \mu_0)[1 - s(\tau', \mu_0)] \times \sum_{l=0}^{\infty} \frac{c_l(\tau')}{4\pi} \int_{-1}^{1} P_l(\mu') \int_0^{2\pi} \mathcal{P}(\vec{\Omega}, \vec{\Omega}') d\varphi'\, d\mu' \\ &\qquad + \varepsilon_1' \end{aligned} \tag{5.5}$$

where φ' is the azimuthal component of integration variable $\vec{\Omega}'$ and

$$\varepsilon_1' = \frac{1}{4\pi}\iint_{4\pi} \varepsilon_1 \mathcal{P}\left(\vec{\Omega}, \vec{\Omega}'\right) d\vec{\Omega}'. \tag{5.6}$$

The phase function $\mathcal{P}\left(\vec{\Omega}, \vec{\Omega}'\right)$ can be expanded with associated Legendre polynomial by using the addition theorem as follows:

$$\mathcal{P}\left(\vec{\Omega}, \vec{\Omega}'\right) = \sum_{m=0}^{\infty} \alpha_m \sum_{n=0}^{m} (2 - \delta_{n0}) \frac{(m-n)!}{(m+n)!} P_m^n(\mu) P_m^n(\mu') \cos n(\varphi - \varphi'), \tag{5.7}$$

where α_m is the expansion coefficient, $P_m^n(\mu)$ is the associated Legendre polynomials with degree m and order n. δ_{n0} is the Kronecker delta (i.e. 1 when $n = 0$, and 0 otherwise). Only $n = 0$ terms survive when Eq. (5.7) is integrated with respect to φ' as appears in Eq. (5.5), i.e.

$$\int_0^{2\pi} \mathcal{P}\left(\vec{\Omega}, \vec{\Omega}'\right) d\varphi' = 2\pi \sum_{m=0}^{\infty} \alpha_m P_m(\mu) P_m(\mu'). \tag{5.8}$$

Note that the associated Legendre polynomials on the right hand side of Eq. (5.7) is reduced to the Legendre polynomials in Eq. (5.8). With Eq. (5.8) and the orthogonality of Legendre polynomials, Eq. (5.5) can be rewritten as follows:

$$\begin{aligned} &\frac{1}{4\pi}\iint_{4\pi} I\left(\tau', \vec{\Omega}'\right) \mathcal{P}\left(\vec{\Omega}, \vec{\Omega}'\right) d\vec{\Omega}' \\ &\quad = C(\tau', \mu_0) s(\tau', \mu_0) \mathcal{P}\left(\vec{\Omega}, \vec{\Omega}_0\right) \\ &\quad + C(\tau', \mu_0)[1 - s(\tau', \mu_0)] \sum_{l=0}^{\infty} \frac{\alpha_l}{2l+1} P_l(\mu)\, c_l(\tau') + \varepsilon_1'. \end{aligned} \tag{5.9}$$

Therefore, substitution of Eq. (5.2) into $I\left(\tau', \vec{\Omega}'\right)$ in the integral of Eq. (5.1) results in the following equation:

$$\mu\left[I\left(0,\vec{\Omega}\right)-I\left(\tau_C,\vec{\Omega}\right)e^{-\frac{\tau_C}{\mu}}\right]$$

$$\begin{aligned}&=\varpi\int_0^{\tau_C}e^{-\frac{\tau}{\mu}}C(\tau',\mu_0)s(\tau',\mu_0)\mathcal{P}\left(\vec{\Omega},\vec{\Omega}_0\right)d\tau'\\&+\varpi\int_0^{\tau_C}e^{-\frac{\tau}{\mu}}C(\tau',\mu_0)[1-s(\tau',\mu_0)]\sum_{l=0}^{\infty}\frac{\alpha_l}{2l+1}P_l(\mu)c_l(\tau')\,d\tau'\\&+\varpi\int_0^{\tau_C}e^{-\frac{\tau}{\mu}}\varepsilon_1'd\tau'.\end{aligned}\tag{5.10}$$

Multiplying π/E_0 and extracting $\mathcal{P}\left(\vec{\Omega},\vec{\Omega}_0\right)$ out of the integral, Eq. (5.9) can be rewritten as follows:

$$\frac{\mu\pi}{E_0}\left[I\left(0,\vec{\Omega}\right)-I\left(\tau_C,\vec{\Omega}\right)e^{-\frac{\tau_C}{\mu}}\right]=S(\tau_C,\mu,\mu_0)\mathcal{P}\left(\vec{\Omega},\vec{\Omega}_0\right)+Q(\tau_C,\mu,\mu_0)+\varepsilon_2,\tag{5.11}$$

where

$$S(\tau_C,\mu,\mu_0)=\frac{\varpi\pi}{E_0}\int_0^{\tau_C}e^{-\frac{\tau'}{\mu}}C(\tau',\mu_0)s(\tau',\mu_0)d\tau'\tag{5.12}$$

$$\begin{aligned}Q(\tau_C,\mu,\mu_0)=\frac{\varpi\pi}{E_0}\int_0^{\tau_C}&e^{-\frac{\tau'}{\mu}}C(\tau',\mu_0)[1-s(\tau',\mu_0)]\\&\times\sum_{l=0}^{\infty}\frac{\alpha_l}{2l+1}P_l(\mu)c_l(\tau')\,d\tau',\end{aligned}\tag{5.13}$$

and E_0 is the solar irradiance at the top of the atmosphere. The function $S(\tau_C,\mu,\mu_0)$ is called the amplification function because it determines the magnitude of the single scattering-like component of the measured reflectance, and the function $Q(\tau_C,\mu,\mu_0)$ is called the anisotropy function because it describes the anisotropy of the radiance that depends only on the solar and viewing zenith angles (not on relative azimuth angle).

Note that the error of fitting varies with direction, and error of fitting ε_2 is related to ε_1 by:

$$\varepsilon_2 = \frac{\pi}{E_0}\int_0^{\tau_C} e^{-\frac{\tau}{\mu}}\frac{\varpi}{4\pi}\iint_{4\pi}\varepsilon_1\mathcal{P}(\vec{\Omega},\vec{\Omega}')d\vec{\Omega}'\,d\tau. \tag{5.14}$$

5.2.2 Improved phase function estimation

In this section, we derive a fundamental formula used in our phase function estimation, utilizing the approximation introduced in Section 5.2.2. From here on, $S(\tau_C,\mu,\mu_0)$ and $Q(\tau_C,\mu,\mu_0)$ are written as $S(\tau_C)$ and $Q(\tau_C)$ for simplicity, and all quantities with a dagger means that they are defined similarly to the non-daggered quantities but for a known phase function, instead of actual phase function.

In the SAD analysis, we first retrieve the spherical albedo from a measurement in each viewing direction independently, assuming a phase function to be evaluated. Denoting the retrieved optical thickness from a measurement in direction $\vec{\Omega}$ as $\tau_C^{\dagger}(\vec{\Omega})$, the retrieved spherical albedo can be written as $\gamma^{\dagger}\left(\tau_C^{\dagger}(\vec{\Omega})\right)$. Daggers are added because the optical thickness retrieval requires the knowledge of the phase function, and the results depend on the assumed phase function. The retrieved optical thickness and the relation between the optical thickness and spherical albedo depend on the assumed phase function. The mean of retrieved spherical albedos averaged over available angles is defined as the mean spherical albedo and written as $\overline{\gamma^{\dagger}} = \overline{\gamma^{\dagger}\left(\tau_C^{\dagger}(\vec{\Omega})\right)}$. The SAD value is the difference between the retrieved spherical albedo and the mean spherical albedo: $\gamma^{\dagger}\left(\tau_C^{\dagger}(\vec{\Omega})\right) - \overline{\gamma^{\dagger}}$. While the SAD value is to some extent indicative of the difference

between assumed phase function and actual phase function, it cannot predict the actual phase function.

We utilize the property of the SAD method that the mean spherical albedo $\overline{\gamma^{\dagger}}$ is a good estimate of the true spherical albedo $\gamma(\tau_C)$, where τ_C is the actual optical thickness. As there is a one-to-one relation between the optical thickness and the spherical albedo for a given phase function (Doutriaux-Boucher et al. 2000), we can define the optical thickness at mean spherical albedo as $\widetilde{\tau_C}^{\dagger}$ satisfying $\gamma^{\dagger}\left(\widetilde{\tau_C}^{\dagger}\right) = \overline{\gamma^{\dagger}}$.

Our approach uses the reflectivity at such cloud optical thickness and defines it as $R_{msa}^{\dagger}(\vec{\Omega})$. From Eq. (5.11), we can write as follows:

$$\mu\mu_0\left[R_{msa}^{\dagger}(\vec{\Omega}) - R_0^{\dagger}(\vec{\Omega})e^{-\frac{\widetilde{\tau_C}^{\dagger}}{\mu}}\right] = S^{\dagger}\left(\widetilde{\tau_C}^{\dagger}\right)\mathcal{P}^{\dagger}(\Theta) + Q^{\dagger}\left(\widetilde{\tau_C}^{\dagger}\right) + \widetilde{\varepsilon_2}^{\dagger}, \qquad (5.15)$$

where $R_0^{\dagger}(\vec{\Omega})$ is the reflectivity of surface and atmosphere below clouds, and $\widetilde{\varepsilon_2}$ is an approximation error. On the other hand, Eq. (5.11) can be written as follws:

$$\mu\mu_0\left[R_{obs}(\vec{\Omega}) - R_0(\vec{\Omega})e^{-\frac{\tau_C}{\mu}}\right] = S(\tau_C)\mathcal{P}(\Theta) + Q(\tau_C) + \varepsilon_2. \qquad (5.16)$$

Taking the difference of Eqs. (5.15) and (5.16),

$$\begin{aligned}\mu\mu_0\left[R_{obs}(\vec{\Omega}) - R_{msa}^{\dagger}(\vec{\Omega})\right] &\\ = \mu\mu_0\left[R_0(\vec{\Omega})e^{-\frac{\tau_C}{\mu}} - R_0^{\dagger}(\vec{\Omega})e^{-\frac{\widetilde{\tau_C}^{\dagger}}{\mu}}\right] &\\ + \left[\mathcal{P}(\Theta) - \mathcal{P}^{\dagger}(\Theta)\right]S^{\dagger}\left(\widetilde{\tau_C}^{\dagger}\right) + \Delta.&\end{aligned} \qquad (5.17)$$

The first term on the right-hand side represents the difference of surface contribution, and this term is usually small for the MISR measurements over oceans at near infrared

wavelengths. The second term is the phase function difference with a amplification function $S^{\dagger}(\widetilde{\tau_C}^{\dagger})$, and the last term is the contribution from the in-cloud radiance difference, i.e.,

$$\Delta = \left[Q(\tau_C) - Q^{\dagger}(\widetilde{\tau_C}^{\dagger})\right] + \mathcal{P}(\Theta)\left[S(\tau_C) - S^{\dagger}(\widetilde{\tau_C}^{\dagger})\right] + \left[\varepsilon_2 - \widetilde{\varepsilon_2}^{\dagger}\right]. \quad (5.18)$$

We find that the magnitude of Δ is reduced by multiplying $S(\tau_C)$ by the mean backward scattering ρ:

$$\rho = \int_{\Theta_{min}}^{\Theta_{max}} \mathcal{P}(\Theta) d\,(\cos\Theta) \quad (5.19)$$

where $\Theta_{min} = 90°$ and $\Theta_{max} = 160°$ in this study. By multiplying ρ/ρ to $\mathcal{P}(\Theta)$ in Eq. (5.16) and $\rho^{\dagger}/\rho^{\dagger}$ to $\mathcal{P}^{\dagger}(\Theta)$ in Eq. (5.15), the rewritten form of Eqs. (5.17) and (5.18) are obtained as follows:

$$\mu\mu_0\left[R_{obs}(\vec{\Omega}) - R^{\dagger}_{msa}(\vec{\Omega})\right] = \left[\frac{\mathcal{P}(\Theta)}{\rho} - \frac{\mathcal{P}^{\dagger}(\Theta)}{\rho^{\dagger}}\right]\rho^{\dagger}S^{\dagger}(\widetilde{\tau_C}^{\dagger}) + \Delta_{MSA}, \quad (5.20)$$

where ρ is the mean backward scattering of the actual phase function (unknown), $\rho^{\dagger}$ is the mean backward scattering of the assumed phase function, and Δ_{MSA} are defined as follows:

$$\Delta_{MSA} = \left[Q(\tau_C) - Q^{\dagger}(\widetilde{\tau_C}^{\dagger})\right] + \frac{\mathcal{P}(\Theta)}{\rho}\left[\rho S(\tau_C) - \rho^{\dagger}S^{\dagger}(\widetilde{\tau_C}^{\dagger})\right] + \left[\varepsilon_2 - \widetilde{\varepsilon_2}^{\dagger}\right]. \quad (5.21)$$

Note that in the actual retrieval, all functions without dagger (i.e. $Q(\tau_C)$, $\mathcal{P}(\Theta)$, $S(\tau_C)$, and ε_2) are true but unknown, so Δ_{MSA} cannot be explicitly computed. The Δ_{MSA} contains contributions from the difference of in-cloud radiance structure between assumed and actual clouds.

The retrieval errors are given by Δ_{MSA}. Readers are reminded that the only differences between functions $Q(\tau_C), S(\tau_C)$, and ε_2 appear in Δ_{MSA} (see Eq. (5.21)), and even when the approximation in Eq. (5.2) introduces approximation error ε_2, the approach in this study is valid as long as a small change of phase function triggers a small change of ε_2.

In this study, results at scattering angles between 100° and 160° are presented because our sensitivity study shows that Eq. (5.20) provides a reliable phase function estimate in this scattering angle range. Further study is needed to identify the relative contributions of each term in Δ_{MSA} to the error outside of this range.

5.3 Data and methodology

This section describes the method of applying Eq. (5.20) to actual satellite data from the MISR sensor. As mentioned in Section 5.2, our phase function estimation consists of three steps: (Step 1) selection of satellite data that qualifies for the analysis, (Step 2) estimation of 39 actual phase function values corresponding to 39 precomputed phase functions, and (Step 3) selection the most appropriate phase function from the 39 candidates.

In Step 2, Eq. (5.20) is applied to actual satellite data, assuming $\Delta_{MSA} = 0$. This assumption is justified as long as (1) the actual phase function $\mathcal{P}(\Theta)$ is close to the precomputed phase function $\mathcal{P}^{\dagger}(\Theta)$ and (2) the number of measurement directions is reasonably large. With $\Delta_{MSA} = 0$, Eq. (5.20) becomes:

$$\frac{\mathcal{P}(\Theta)}{\rho} = \frac{\mathcal{P}^{\dagger}(\Theta)}{\rho^{\dagger}} + \frac{\mu\mu_0\left[R_{obs}(\Theta,\mu,\mu_0) - R^{\dagger}_{msa}(\Theta,\mu,\mu_0)\right]}{\rho^{\dagger}S^{\dagger}\left(\widetilde{\tau_C}^{\dagger},\mu,\mu_0\right)}. \tag{5.22}$$

We apply this formula to estimate the actual renormalized phase function $\mathcal{P}(\Theta)/\rho$ from the precomputed renormalized phase function $\mathcal{P}^{\dagger}(\Theta)/\rho^{\dagger}$ and measured reflectivities $R_{obs}(\Theta, \mu, \mu_0)$.

The precomputed phase function $\mathcal{P}^{\dagger}(\Theta)$ is called a "base phase function" in the following sections. This is because the right-hand side of Eq. (5.22) can be seen as a sum of the renormalized "base phase function" $\mathcal{P}^{\dagger}(\Theta)/\rho^{\dagger}$ and a correction term. Note that $R^{\dagger}_{msa}(\Theta, \mu, \mu_0)$ and $S^{\dagger}(\widetilde{\tau_C}, \mu, \mu_0)$ in the correction term also depend on $\mathcal{P}^{\dagger}(\Theta)/\rho^{\dagger}$, as the dagger symbol indicates. Therefore, when a base phase function is given, a set of multi-angle measurements provides an analytical estimate of the actual phase function through Eq. (5.22). We estimate the actual phase function corresponding to all 39 base phase functions in Step 2 and select the most appropriate base phase function in Step 3.

This section describes the criteria of pixel selection, the method to compute quantities in Eq. (5.22) from actual satellite data, and the selection of the best base phase function. Section 5.3.1 outlines the satellite data we use and Section 5.3.2 explains how we select pixels suitable for the analysis. Section 5.3.3 describes the details of these 39 base phase functions, and Section 5.3.4 illustrates how $S^{\dagger}(\widetilde{\tau_C}, \mu, \mu_0)$ and $R^{\dagger}_{msa}$ are computed for a given base phase function. Finally, Section 5.3.5 describes how Eq. (5.22) is applied to the qualified satellite data and how the best base phase function is selected from 39 candidates.

5.3.1 MISR-MODIS collocated data

This study applies the phase function estimation method introduced in Section 5.2 with practical refinements described in the following part of Section 5.3 to MISR

data, including the MISR Level 1 Radiance product and Level 2 Cloud Product (TC_CLOUD) for a one month period between September 1, 2013 and September 30, 2013. The radiances are projected onto the reference ellipsoid, and co-registered so every pixel is observed from 9 different viewing directions. The stereo-photogrammetric height reported in the Level 2 product is used to correct the parallax in the Level 1 product. The parallax corrected data is collocated to the Moderate Resolution Imaging Spectroradiometer (MODIS) Level 2 Cloud Product (Platnick et al., 2017) to provide additional information needed in the pixel selection.

5.3.2 Selection of pixels

Pixel selection consists of three stages. The first stage detects cloud ridges by finding radiometrically convex parts of clouds because the cloud 3-D effect is least evident in such parts, and the second stage limits clouds to be ice cloud over ice-free ocean between 60°S and 60°N. Finally, we confine our analysis to pixels observed with two cameras at the same scattering angle. As a result of this selection, 208,731 pixels in September 2013 are selected for analysis.

Radiometrically convex and flat parts of clouds are first selected by applying a Sobel on Gaussian (SoG) filter and a Laplace on Gaussian (LoG) filter to the MISR bidirectional reflectance factor (BRF) times the cosine of the solar zenith angle (i.e. reflectance product, following the MODIS terminology). The SoG filter is used to select radiometrically flat parts of clouds, and the LoG filter is used to remove radiometrically concave parts of clouds. The standard deviation of both Gaussian filters is set to 2.0

pixels, and SoG < 0.06, LoG > -0.001 are used as thresholds. These threshold values are validated qualitatively by visual inspection of one day (15 orbits) of MISR data.

The analysis is limited to the brightest cloud pixels (i.e. roughly corresponding to ridges of clouds) identified in this way, and among them, only ice cloud pixels over ice-free ocean are selected. The selection is based on the surface flag in the MISR Ancillary Geographic Product and the Thermal Infrared/Visible combined cloud phase flag in the MODIS Level 2 Cloud product. To avoid contamination from inhomogeneous clouds, we select pixels with sub-pixel inhomogeneity index H_σ (Liang et al. 2009) less than 1.

The last refinement is motivated by the necessity to select the best base phase function from the 39 candidates. To do this by the method described later in Section 5.3.5, we select pixels seen by two cameras at the same scattering angle. We call a pair of such cameras a base-finding pair. Because of the symmetric configurations of MISR cameras, pixels with base-finding pairs appear as multiple latitudinal bands, stretching primarily in the cross-track direction as shown in Fig. 5.1. As a pixel can have up to 4 base-finding pairs, the 9 cameras provides 8, 7, 6, or 5 different scattering angles, and duplicated angles are used to identify the most appropriate base phase function.

In some observation geometries, more than one base-finding pair is available. In such a case, we select the pair that does not involve the An (nadir-viewing) camera. If more than two pairs do not involve the An camera, the pair with the largest scattering angles is selected.

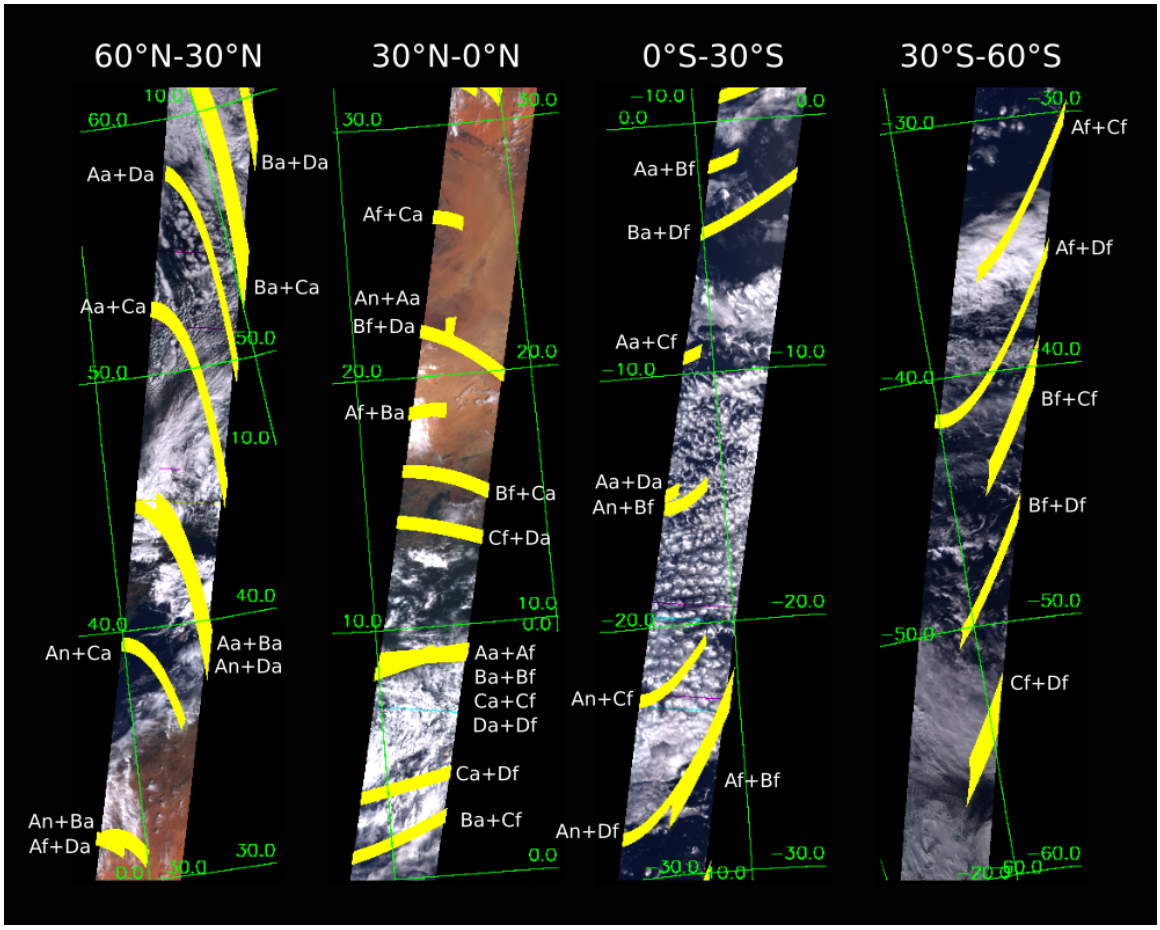

Fig. 5.1. Location of pixels with base-finding pairs. At yellow pixels, there is at least one base-finding pair (a pair of measurements with the same scattering angle). White texts beside yellow bands indicate camera combinations of base-finding pairs, and green lines and texts show latitude and longitude. The geometry data is from orbit 73105 (September 15, 2013).

5.3.3 Base phase functions

The base phase function is the known phase functions utilized in the estimation of unknown actual phase function. The formal definition is given in the beginning of Section 5.3, as the precomputed phase function $\mathcal{P}^{\dagger}(\Theta)$ in Eq. (5.22).

The base phase functions are calculated by assuming the ice cloud particles are single hexagonal shapes. Light scattering calculations are performed to compute base phase functions at 39 aspect ratios varying from $\alpha = 2A/L = 1/9$ (long hexagonal column) to $\alpha = 9$ (thin hexagonal plate) with a constant surface roughness of $\sigma^2 = 0.1$. The surface roughness (Yang and Liou, 1998) in this study is a surrogate for roughened surface textures and other imperfections that exist in natural ice cloud particles. The surface tilt method (Section 2.3.1) with Yang-1 distribution (Section 2.2.2) is used to simulate the surface roughness.

This combination of particle shape, aspect ratio, and surface roughness parameter is selected to capture a wide range of actual phase functions with a minimum number of base phase functions derived from simple particle shapes. Surface roughness is assumed constant at $\sigma^2 = 0.1$ because previous studies indicate that roughened particles provides more consistent multi-angle reflectivities than smooth particles, and our $S(\tau_C, \mu, \mu_0)$ depends primarily on aspect ratio and less on the surface roughness parameter. The moderate roughness $\sigma^2 = 0.1$ is assumed rather than the severe roughness $\sigma^2 = 0.5$ in the MODIS Colleciton 6 ice cloud model and the CERES Edition 4 ice cloud model so that the retrieval successfully covers a wide range of solutions centered at $\sigma^2 = 0.1$ (i.e. either less roughened or more roughened).

These base phase functions and corresponding single scattering properties are computed with the Improved Geometric Optics Method (IGOM; Yang and Liou, 1996) and the Invariant Imbedded T-Matrix (IITM) method (Bi and Yang, 2014). The IITM method is used for small particles with size parameter ($x = \pi D_{max}/\lambda$) less than 40,

where D_{max} is the maximum dimension and λ is the wavelength, and the IGOM is used for larger particles. The edge effect is taken into account by the method described by Yang et al. (2013). A Gamma particle size distribution ($v_{eff} = 0.1, D_{eff} = 60$ μm) is assumed, but our sensitivity study shows that $S(\tau_C, \mu, \mu_0)$ and $Q(\tau_C, \mu, \mu_0)$ are not sensitive to particle size variations for $D_{eff} > 40$ μm.

5.3.4 Computing the amplification function "$S^{\dagger}$" and reflectivity "$R^{\dagger}_{msa}$"

In addition to base phase functions, the correction term in Eq. (5.22) requires the amplification function $S^{\dagger}(\tau_C, \mu, \mu_0)$ and the reflectivity at the mean spherical albedo $R^{\dagger}_{msa}(\vec{\Omega})$. Both quantities are computed from the results of rigorous radiative transfer simulations. For each base phase function, the radiance is computed with the adding-doubling full vector radiative transfer model (Huang et al. 2015) with δ-M truncation (Wiscombe, 1977) and the TMS correction(Nakajima and Tanaka, 1988). No surface reflection and aerosols are assumed, so all reflected radiance is assumed to come from the ice cloud layer. The process described in this section is repeated for all 39 base phase functions, as $S^{\dagger}$ and $R^{\dagger}_{msa}$ depend on the specific base phase function.

5.3.4.1 Computing $S^{\dagger}(\tau_C, \mu, \mu_0)$

As the amplification factor $S^{\dagger}(\tau_C, \mu, \mu_0)$ is defined in the same way as in Eq. (5.12), a straightforward approach to compute $S^{\dagger}(\tau_C, \mu, \mu_0)$ is to directly integrate the product of actinic flux $C^{\dagger}(\tau, \mu_0)$ and partitioning factor $s^{\dagger}(\tau, \mu_0)$ vertically through a cloud. This approach is possible only when the angular profile of the forward peak is well simulated with the radiative transfer simulation. For large ice cloud particles, this usually requires a very large number of ray streams, and the computational cost is

prohibitively large with standard radiative transfer solvers. For this reason, we empirically fit $S^{\dagger}(\tau_C, \mu, \mu_0)$ with the simulated reflectivity, assuming empirical functional forms.

When assuming there is no incident radiance onto the bottom of the cloud, and assuming a precomputed phase function $\mathcal{P}^{\dagger}(\Theta)$ in place of the actual phase function $\mathcal{P}(\Theta)$, Eq. (5.11) is equivalent to:

$$\mu\left[\mu_0 R\left(\vec{\Omega}\right)\right] = S^{\dagger}(\tau_C, \mu, \mu_0)\mathcal{P}^{\dagger}(\Theta) + Q^{\dagger}(\tau_C, \mu, \mu_0) + \gamma^{\dagger}(\tau_C) + \varepsilon_2^{\dagger}. \tag{5.23}$$

We assume the following empirical functional forms:

$$S^{\dagger}(\tau_C, \mu, \mu_0) = s_1 e^{-Ms_2} + s_3 M^{-2} \tag{5.24}$$

$$\begin{aligned} Q^{\dagger}(\tau_C, \mu, \mu_0) = {} & [q_1 e^{-Mq_2} + q_3 M^{-2} + q_4 M^{-4}] \\ & + [q_5 e^{-Mq_6} + q_7 M^{-2} + q_8 M^{-4}] \left(\frac{1}{\mu_0} - \frac{1}{\mu}\right)^2 \end{aligned} \tag{5.25}$$

$$\varepsilon_2^{\dagger} = (a + bM)\cos\Theta + \varepsilon_{fit} \tag{5.26}$$

where $s_1, s_2, s_3, q_1, q_2, q_3, q_4, q_5, q_6, q_7, q_8, a$ and b are regression coefficients at cloud optical thickness τ_C, $M = \left(\frac{1}{\mu_0} + \frac{1}{\mu}\right)$ is the sum of the air mass factor including the incoming and outgoing ray directions, and ε_{fit} is the fitting error. The functional forms defined in Eqs. (5.24), (5.25), and (5.26) are selected based on previous experimental fitting of M-stratified data with M-independent functional forms. By assuming M-dependent functional forms, fitting becomes stable even in directions where the variation of the phase function is too small to accurately compute $S(\tau_C, \mu, \mu_0)$. The accuracy of the

fitting is better than 0.65% or 0.001 (in terms of reflectance product, $\mu_0 R$) for all particle shapes, all optical thickness values from 0.5 to 100, and all directions with $M < 7$.

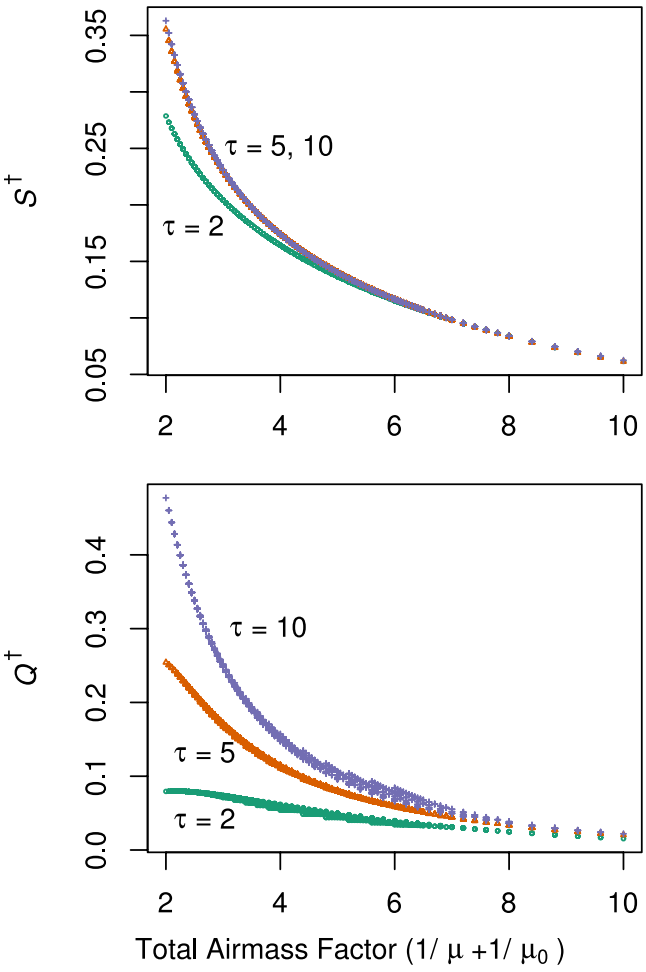

Fig. 5.2. Air mass factor $\left(M = \frac{1}{\mu} + \frac{1}{\mu_0}\right)$ dependence of functions $S^\dagger(\tau, \mu_0, \mu)$ and $Q^\dagger(\tau, \mu_0, \mu) + \gamma^\dagger(\tau)$. A single column ice crystal with aspect ratio $\alpha = \frac{2a}{L} = 1$ and degree of surface roughness $\sigma^2 = 0.1$ is used. Three cloud optical thickness values are assumed: $\tau = 2, 5, 10$.

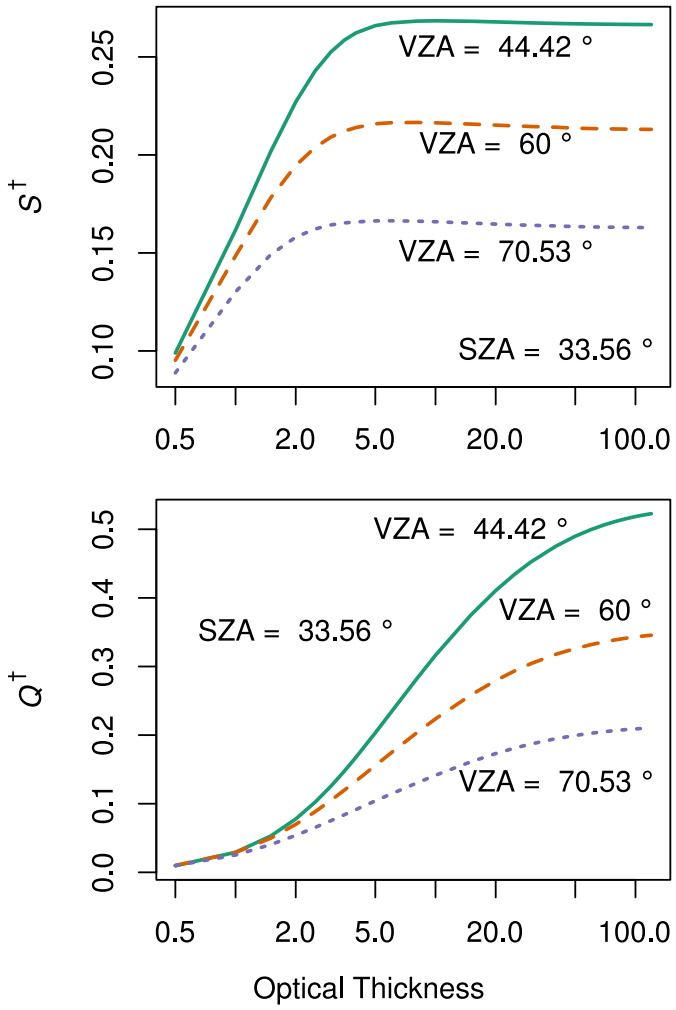

Fig. 5.3. Optical thickness dependence of functions $S^\dagger(\tau, \mu_0, \mu)$ and $Q^\dagger(\tau, \mu_0, \mu) + \gamma^\dagger(\tau)$. A single column ice crystal with aspect ratio $\alpha = \frac{2a}{L} = 1$ and degree of surface roughness $\sigma^2 = 0.1$ is used. Solar zenith angle is 33.56°, and three viewing zenith angles corresponding to MISR B, C, and D cameras are assumed: 44.52°, 60°, 70.53°.

The fitted functions $S^\dagger(\tau_C, \mu, \mu_0)$ and $Q^\dagger(\tau_C, \mu, \mu_0)$ primarily depend on cloud optical thickness and the air mass factor M. They are both monotonically decreasing functions of the air mass factor as shown in Fig. 5.2. Note in Fig. 5.2 that $S^\dagger$ for $\tau_C = 5$ and $\tau_C = 10$ are indistinguishable, whereas the separation of $Q^\dagger$ is clear. This is further

illustrated in Fig.5.3 While both $S^{\dagger}$ and $Q^{\dagger}$ are non-decreasing functions of cloud optical thickness, the value of $S^{\dagger}$ saturates out at about an optical thickness $\tau_C = 5$. The implication of this saturation is that the magnitude of single scattering-like signal is constant at optical thickness 5 or greater, and the increase of cloud reflectivity depends on the azimuthally-independent term. This saturation appears to be analogous to the saturation of polarimetric reflectivity reported by Masuda and Takashima (1992) and others (Goloub, 1994; Goloub et al., 2000; Riedi et al., 2010).

5.3.4.2 Computing $R^{\dagger}_{msa}(\vec{\Omega})$

As defined in Section 5.2.3, $R^{\dagger}_{msa}$ is the reflectivity of a cloud with a specified base phase function when the optical thickness is $\widetilde{\tau_C}^{\dagger}$. The results of the radiative transfer simulation in Section 5.3.4.a are tabulated and used to provide $R^{\dagger}_{msa}(\vec{\Omega}, \vec{\Omega}_0)$. The challenge in computing $\widetilde{\tau_C}^{\dagger}$ is posed by the non-uniform angular sampling in satellite data.

As the satellite angular sampling is not uniform, we use the weighted mean of spherical albedo to compute $\widetilde{\tau_C}^{\dagger}$: $\gamma^{\dagger}\left(\widetilde{\tau_C}^{\dagger}\right) = \overline{\gamma^{\dagger}\left(\tau_C^{\dagger}(\vec{\Omega})\right) w}$, where w is the normalized weight to adjacent scattering angles as follows:

$$w_i = \frac{1}{W}\int_{\Theta_{i-1}}^{\Theta_{i+1}} \frac{1}{2}\, d(\cos\Theta)\,. \tag{5.27}$$

where W is the normalization constant, Θ is the scattering angle, and i is the index of viewing directions out of the sun glitter (glitter angle > 30°) and at scattering angles

between 90° and 160°. For measurements at the largest and smallest scattering angles between 90° and 160°, different weights are used as follows.

$$w_1 = \frac{1}{W}\int_{90^\circ}^{\Theta_1} d(\cos\Theta) + \frac{1}{W}\int_{\Theta_1}^{\Theta_2}\frac{1}{2}\, d(\cos\Theta), \tag{5.28}$$

$$w_n = \frac{1}{W}\int_{\Theta_{n-1}}^{\Theta_n}\frac{1}{2}\, d(\cos\Theta) + \frac{1}{W}\int_{\Theta_n}^{160^\circ} d(\cos\Theta). \tag{5.29}$$

This approach provides a more stable $\widetilde{\tau_C}^{\dagger}$ than a simple arithmetic mean of the retrieved spherical albedo values.

5.3.5 Phase function estimation

Equation (5.22) is applied to each viewing direction in a cloud pixel that passes all these tests to produce 39 sets of estimated renormalized phase function values at 8, 7, 6, or 5 scattering angles. To select the most appropriate base phase function from 39 candidates, the difference of the estimated renormalized phase function values (Δ_{bf}) from the base-finding pair (two viewing directions with the same scattering angle) is computed for all 39 candidates. Then, cloud pixels that pass all previously mentioned tests are collected into cloud groups based on adjacency. When another valid cloud pixel exists in the 8 neighboring pixels around a valid cloud pixel, those two cloud pixels are grouped into the same group. This step is repeated and the group usually contains more than 10 ice cloud pixels. Finally, the mean values of Δ_{bf} averaged over all pixels in the cloud group are compared among the 39 candidates, and the base phase function that gives the smallest average $|\Delta_{bf}|$ is selected as the base function for the all pixels in the group.

In summary, the phase function estimates from the base-finding pair determines the best base phase function. The phase function estimates corresponding to the best base phase function identified in this way is recorded and presented as results in the following section.

5.4. Results

In September 2013, the MISR multi-angle measurements at cloud ridges from 60°S to 60°N show that two hexagonal column models best agree with the estimated renormalized phase functions $\mathcal{P}(\Theta)/\rho$ (Fig. 5.4) at scattering angles greater than 120°. At scattering angles between 135° and 160°, a plate particle model ($\alpha = 3.15, \sigma^2 = 0.5$) agrees with the estimated median, and between 120° and 135°, a column particle model ($\alpha = 0.625, \sigma^2 = 0.5$) performs well. No single hexagonal column or plate model in our calculations ($\alpha = 1/9 - 9, \sigma^2 = 0 - 0.5$) has a renormalized phase function that agrees with the estimate at all scattering angles between 100° and 160°.

The inconsistency of the fitting of the renormalized phase function in portions of the scattering angle range is partly because the estimated renormalized phase functions have different latitudinal weights at different scattering angles. In Fig. 5.5, the tropical (latitude < 30°) data show that a column particle model ($\alpha = 0.625, \sigma^2 = 0.5$) agrees well with the estimated renormalized phase functions. As a large population of tropical cloud pixels in the scattering angle range between 120° and 135° contributes to the global data, a good fit with this particle model is achieved in Fig. 5.4 as well as in Fig. 5.5. In Fig. 5.5, the MODIS Collection 6 particle model also performs as well as the

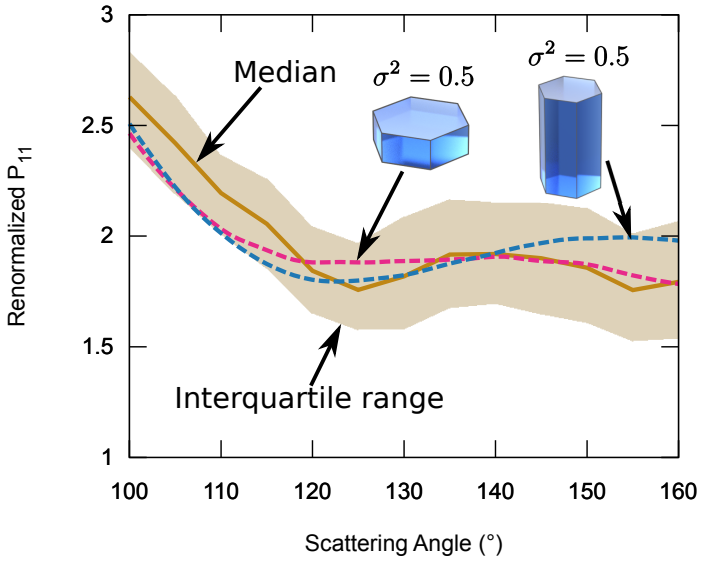

Fig. 5.4. Estimated renormalized phase function from the MISR data for all latitudes (0° to 60°). The data are collected during September 2013. Shading indicates the interquartile range of all estimated values in 5° scattering angle bins, and the solid line is the median. Dotted lines show the partially matching renormalized phase functions: a hexagonal column with $\alpha = 0.625$ and $\sigma^2 = 0.5$; and a hexagonal plate with $\alpha = 3.15$ and $\sigma^2 = 0.5$.

single column model, especially at scattering angles between 135° and 160°. Having an accurate model for this scattering angle range is significantly important for tropical cloud retrievals as a large number of pixels are measured at this scattering angle range in the tropics.

On the other hand, in Fig. 5.6, the extratropical (30° < latitude < 60°) data do not show agreement with any of our single column models or aggregate models (plate and column aggregates, solid bullet rosette) described in Yang et al. (2013). At scattering angles between 135° and 160°, however, a roughened plate particle model ($\alpha = 3.15, \sigma^2 = 0.5$) provides a good fit to the measurements. As extratropical data from scattering angles

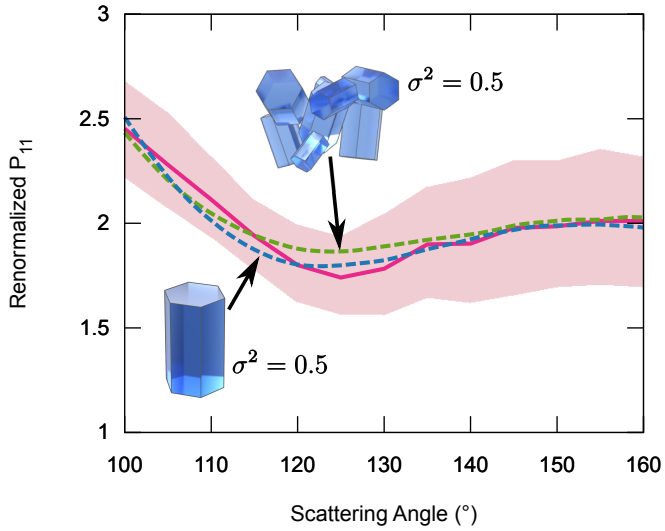

Fig. 5.5. Estimated tropical (latitude < 30°) renormalized phase function. The data are collected by the MISR during September 2013. Shading indicates the interquartile range of the all estimated values in 5° scattering angle bins, and the solid line is the median. Dotted lines show two renormalized phase functions for a hexagonal column with $\alpha = 0.625$ and $\sigma^2 = 0.5$; and the MODIS Collection 6 ice particle model.

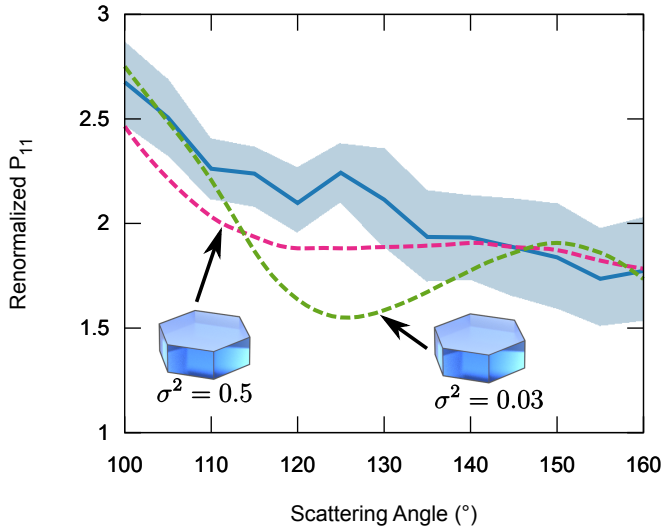

Fig. 5.6. Estimated extratropical (30° < latitude < 60°) renormalized phase function. The data are collected by the MISR during September 2013. Shading indicates the interquartile range of the all estimated values in 5° scattering angle bins, and the solid line is the median. Dotted lines show two renormalized phase functions for a roughened hexagonal plate with $\alpha = 3.15$ and $\sigma^2 = 0.5$; and the same plate particle with less roughness $\sigma^2 = 0.03$.

between 135° and 160° are most numerous, Fig. 5.4 shows a good fit with the roughened plate particle at scattering angles between 135° and 160°.

In the extratropics, estimated renormalized phase function from 100° to 110° is significantly larger than renormalized phase functions of any column and plate particles with severe roughness $\sigma^2 = 0.5$, and can be fitted only by less roughened models such as another plate particle model ($\alpha = 3.15, \sigma^2 = 0.03$) shown in Fig. 5.6. However, less roughened models commonly have a smaller renormalized phase function between 115° and 145°, that does not match the measurements. Further investigation is needed for the extratropical latitudes, with considerations of stronger cloud 3-D effects due to oblique solar illumination.

5.5 Discussion

5.5.1 Performance of the method with other degrees of surface roughness

This study estimates the phase function as a difference from the base phase function computed with a fixed degree of surface roughness $\sigma^2 = 0.1$, and finds that certain scattering angle ranges are fitted better by severely roughened particles with $\sigma^2 = 0.5$. As the measurement principle relies on the approximation theory described in Section 5.2, the use of $\sigma^2 = 0.1$ to define base phase functions must be validated. More precisely, as long as the retrieval errors (Δ_{MSA}) are confirmed to be small enough, $\sigma^2 = 0.1$ models can still be used to retrieve $\sigma^2 = 0.5$ phase functions.

For this purpose, we estimate the renormalized phase functions from synthetic data, using exactly the same technique applied to the estimation from the actual data in Section 5.4. The synthetic data is produced by applying 1% radiometric noise to the

radiative transfer simulation results using one day of MISR geometry data on September 22, 2013. The results indicate that the current method can estimate the phase functions with deeper roughness, while Fig. 5.7 shows that there is an aspect-ratio dependent bias when phase functions of less roughened particles are estimated. In Fig. 5.7, this method is valid at roughness $\sigma^2 = 0.03$ to 0.5 for column particles with $\alpha = 1$, $\sigma^2 = 0.05$ to 0.5 for plate particles with $\alpha = 2.5$, and $\sigma^2 = 0.1$ to 0.5 for column particles with $\alpha = 0.4$.

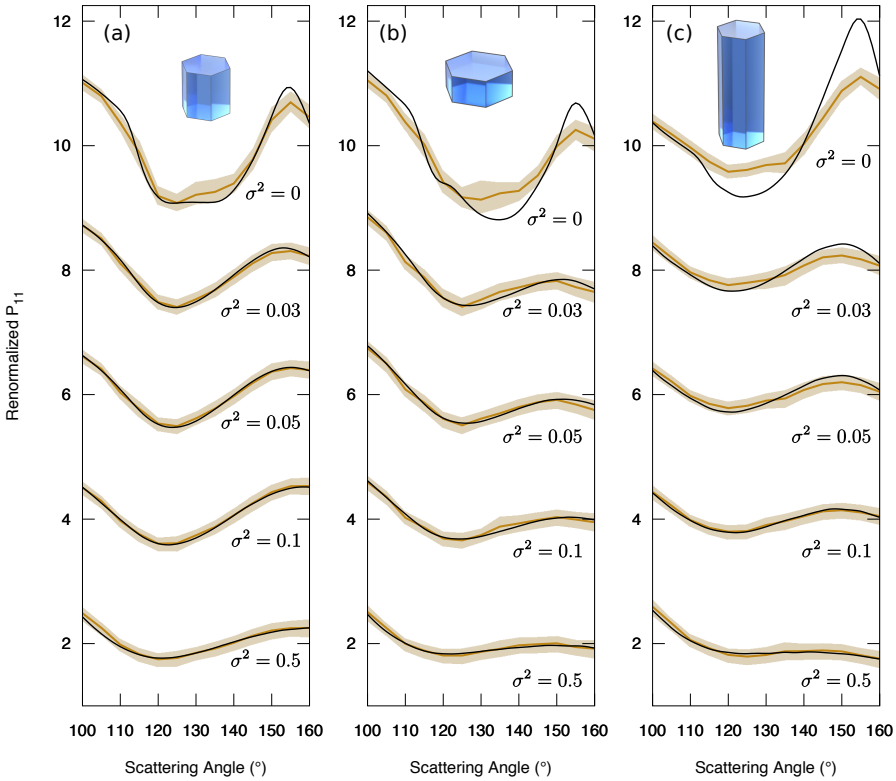

Fig. 5.7. Estimations of renormalized phase function with synthetic data. Each estimated interquartile range and median is shown with brown color shading and a solid line. Black solid lines show true phase functions with roughness $\sigma^2 = 0, 0.03, 0.05, 0.1, 0.5$ (from top to the bottom). A hexagonal column shape with three aspect ratios is assumed in the computation of true phase functions: (a) $\alpha = 1$, (b) $\alpha = 2.5$, and (c) $\alpha = 0.4$.

5.5.2 Performance of the method to infer phase functions of aggregate particle models

A similar test based on synthetic data is conducted to evaluate the performance of the method for aggregate ice particle models. Some light scattering simulations show that the phase function of an aggregate particle resembles that of the constituent elements (Um and McFarquhar, 2007, 2009; van Diedenhoven et al. 2012). Therefore, we anticipate that the same set of single-element base functions works for the aggregate models as well.

In Fig. 5.8, the results of estimation with synthetic data assuming the column aggregate ice particle model show that the interquartile range of the estimated phase function includes the true phase functions with degrees of surface roughness from $\sigma^2 = 0.03$ to 0.5. However, there is a negative bias between scattering angles at 115° and 135° when phase functions of severely roughened particles ($\sigma^2 = 0.1, 0.5$) are estimated. This negative bias might explain the difference in Fig. 5.5 between the estimate in the tropics and the MODIS Collection 6 phase function ($\sigma^2 = 0.5$). The magnitude of the difference between true and the estimated renormalized phase function in Fig. 5.8 is 0.099 for $\sigma^2 = 0.5$, whereas the difference between MODIS Collection 6 and the estimated renormalized phase function is 0.125.

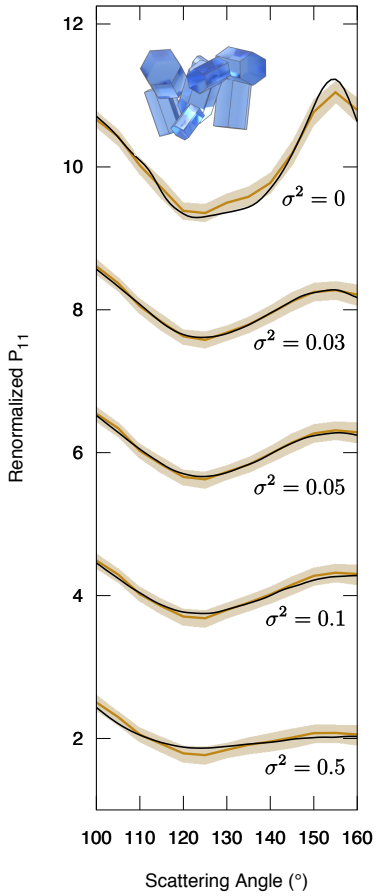

Fig. 5.8. Estimations of renormalized phase function with synthetic data for the MODIS Collection 6 particle shape.

While the performance for the roughened aggregate particle model has a small error, the estimated renormalized phase function for the moderately roughened aggregate particle ($\sigma^2 = 0.03$) shows a nearly perfect match to the true phase function. This indicates that the functions $S^{\dagger}(\tau_C, \mu, \mu_0)$ and $Q^{\dagger}(\tau_C, \mu, \mu_0)$ of less roughened aggregates are close to their counterpart of a more roughened single-element hexagonal column particle. We presume this is not likely to be a mere coincidence because $S^{\dagger}$ and $Q^{\dagger}$ functions are determined by the light that travels into the forward direction in a cloud,

and less surface roughness is required for aggregates to partition more rays from the forward-traveling part ($S^{\dagger}$) into the azimuthally-independent part ($Q^{\dagger}$) than single-element hexagonal particles. Attached aggregate elements deflect light away from the forward direction effectively. Future research is needed to investigate whether $S^{\dagger}$ and $Q^{\dagger}$ functions of less roughened aggregates are approximated by the $S^{\dagger}$ and $Q^{\dagger}$ functions of more roughened single-element hexagonal particles in general.

5.5.3 Selection of the base phase function to reduce estimation errors

Some estimation errors are seen in the experiments with synthetic data as in Sections 5.5.1 and 5.5.2. However, mitigating the errors by adding more base phase function candidates (specifically, more possible ice particle shape and size distributions) requires caution. The top panel in Fig. 5.9 shows the magnitude of estimation error $|\Delta_{MSA}|$ using the Ca camera for a single tropical pixel, and the bottom panel shows the difference of estimated phase function between base-finding pairs (Bf and Ca cameras) at $\Theta = 121°$ (hereafter, Δ_{bf}). Both values are computed when assuming the cloud layer consists of a moderately roughened hexagonal plate particle ($\alpha = 2.5, \sigma^2 = 0.03$). Note that the phase function of this particle is accurately estimated as shown in Fig. 5.7.

As our current candidates of the base phase function are confined to 39 models with degree of roughness $\sigma^2 = 0.1$, the selected model is at the minimum of Δ_{bf} along the blue vertical line in the bottom panel. The location of the selected base particle model is shown in a purple circle. The estimation error, $|\Delta_{MSA}|$, in the purple circle is less than 0.001 as read from the top panel, so the retrieval is successful. The situation would be different when adding a candidate in Zone A in the left bottom corner (nearly

smooth hexagonal plates). The Δ_{bf} in Zone A is small enough to accept such a candidate as a base model, but the estimation error $|\Delta_{MSA}|$ is large enough to produce incorrect estimation. This result implies that we need more base-finding pairs to estimate phase functions more accurately by distinguishing the most appropriate base phase function effectively.

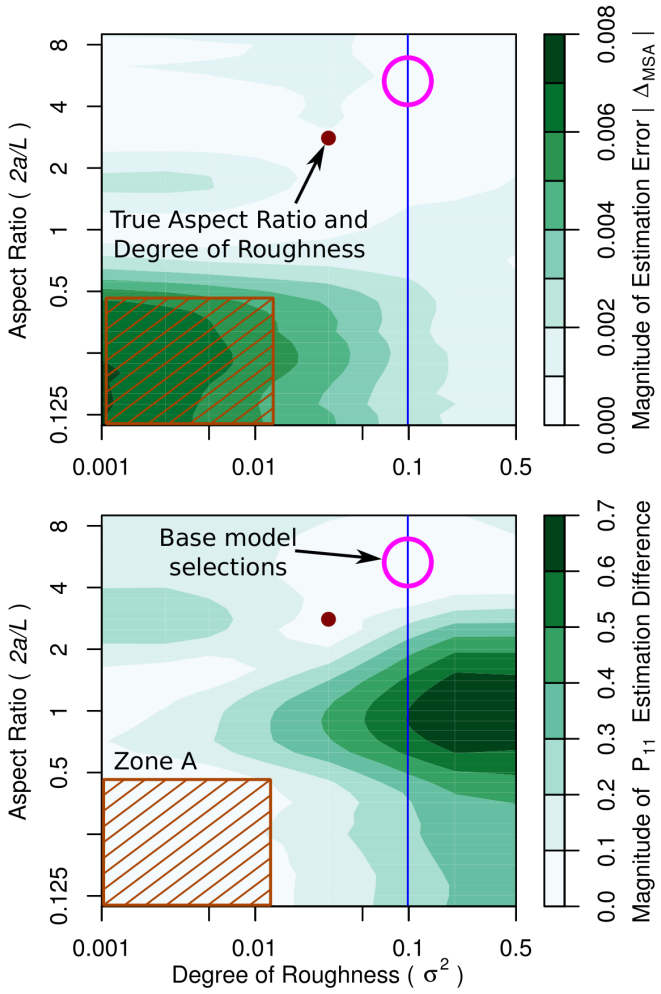

Fig. 5.9. Performance of estimation at a fixed viewing direction for plate particles. The top panel shows the magnitude of estimation error ($|\Delta_{MSA}|$) for the Ca camera, and the bottom panel shows the magnitude of estimated renormalized phase function difference at $\Theta = 121°$ (Bf and Ca cameras). The true phase function is assumed to be for a single hexagonal plate particle with aspect ratio $\alpha = 2.5$.

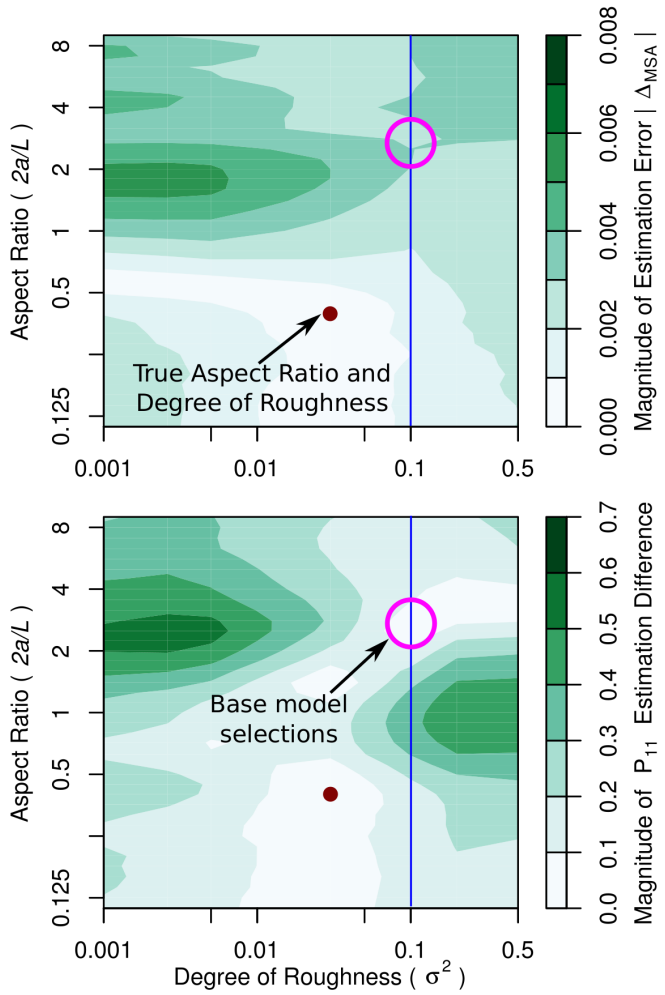

Fig. 5.10. Performance of estimation at a fixed viewing direction for column particles. The viewing direction is the same as Fig. 5.9, but the true phase function is assumed to be for a single hexagonal column particle with aspect ratio $\alpha = 0.4$.

The analysis technique introduced in Fig. 5.9 can also be applied to demonstrate why the phase function of a long column particle ($\alpha = 0.4, \sigma^2 = 0.03$) is less accurately estimated than that of a plate particle (Fig. 5.7). Figure 5.10 shows the estimation error $|\Delta_{MSA}|$ and the estimation difference at the base-finding cameras (Δ_{bf}) for the long column particle. The error pattern Δ_{bf} in Fig. 5.10 resembles Fig. 5.9, so a plate phase

function is likely to be selected as a base phase function, even though the actual shape is a column. This particle selection introduces an error as shown in the purple circle at the top panel, biasing the phase function estimation as in Fig. 5.7. Even though it is not actually possible to explain the estimation error from all latitudes as in Fig. 5.7 with a single-pixel error analysis as in Fig. 5.10, Figs. 5.9 and 5.10 provide valuable insights into the appropriate selection of base phase functions.

5.6 Conclusions

This study introduces a phase function estimation technique that is derived from the radiative transfer equation for a plane parallel homogeneous medium. The inspiration of the technique comes from the resemblance of the spherical albedo difference and the phase function difference reported in previous studies. It is shown that the reflectivity difference is proportional to the difference between the actual phase function and the phase function assumed in the retrievals under certain circumstances. The proportionality coefficient is a decreasing function of air mass factor and an increasing function of the optical thickness, and saturates at optical thickness $\tau \geq 5$.

The proposed method is applied to MISR data collected over global ice-free oceans during September 2013 to compare the estimated phase functions at scattering angles between 100° and 160°. The estimated renormalized phase function shows two scattering angle ranges with different biases in the tropical (latitude < 30°) and extratropical (30° < latitude < 60°) bands. In the global average, the tropical band contributed strongly at scattering angles between 120° and 140°, and the extratropical band between 140° and 160°. In these two latitudinal bands, the estimated renormalized

phase functions are significantly different from the other, resulting in failure of global fitting by any single-element hexagonal particle model with aspect ratios ranging from $\alpha = 1/9$ to 9 and roughness ranging from $\sigma^2 = 0$ to 0.5.

In the tropical latitudes, the estimated renormalized phase function is in good agreement with the phase function of a hexagonal column particle model with aspect ratio $\alpha = 0.625$ and severe surface roughness $\sigma^2 = 0.5$, or with the MODIS Collection 6 cloud models, especially at scattering angles between 135° and 160°.

On the other hand, extratropical data does not match any phase function from the range of pre-computed single hexagonal particle models. However, a plate particle with aspect ratio $\alpha = 3.15$ and surface roughness $\sigma^2 = 0.5$ fits the measurements at scattering angles between 140° and 160°.

Experiments with synthetic data show the validity of the method to estimate renormalized phase functions by assuming hexagonal particles with moderate roughness ($\sigma^2 = 0.1$). The performance is best for a column particle with aspect ratio $\alpha = 1$, but aspect ratio- and scattering angle-dependent biases are found for less roughened particles. The bias in estimating the phase function of a long column particle is especially large, presumably because the analysis selects a plate particle as the base phase function.

The accuracy of the technique is expected to improve when a wider range of ice particle models is employed as base phase function candidates. However, there are some combinations of aspect ratio and optical thickness that might reduce the retrieval accuracy. A theoretical framework developed in this study is helpful to identify such

combinations and to make an appropriate choice of ice particle models used in the retrieval. It also suggests the importance of a well-designed measurements, especially multi-viewing measurements at the same scattering angle.

6 CONCLUSIONS

Recent advances in light scattering calculations made it possible to implement more complex and realistic particle shapes into satellite retrieval algorithms and general circulation model (GCM) radiation schemes. To incorporate the complexity and irregularity of natural cloud particles, various models were developed and validated in the past. These previous studies are based on the "best-fit" method and the effect of instrumental and observational noise are not considered in the validation. Light scattering calculations for these ice cloud models often involve the simulation of surface roughening, but the implementations are poorly documented. In addition, some truncation techniques used in polarized radiative transfer calculations need more solid theoretical support.

Section 2 investigates the tilt angle distribution and tilt methods implemented in the light scattering calculations. It is demonstrated that the surface and beam tilt methods result in different effective roughness distributions due to different rejection criteria for the generated tilt angle and direction. Four tilt angle distributions are summarized and the probability density functions of tilt angles are derived for comparison.

Section 3 derives the application of the δ-fit method to polarized radiative transfer based on the theoretical developments of truncation approximations. The accuracy of the δ-fit and δ-M methods are comparable for the backward scattering directions and the error is on the order of 0.1%.

In Section 4 and 5, different methods are applied to infer the particle shape and surface roughness from multi-angle satellite measurements over tropical and extratropical oceans. In Section 4, the application of the Empirical Orthogonal Function (EOF) analysis reduced the number of parameters to describe particle shapes and surface roughness, allowing the statistical inference technique to play a central role in the retrieval system. The extratropical results indicate that the long column particle shapes, or aggregates of them, with moderate to severe ($0.1 < \sigma^2 < 0.5$) roughness most closely reproduce the total and polarized reflectivity measured by the Polarization and Directionality of Earth's Reflectance (POLDER) sensor. Weak temperature dependence and cloud heterogeneity dependence are seen in the retrieval results. The trend of both dependences are not surprising when the effect of cloud inhomogeneity and the presence of quasi-horizontally oriented particles are considered. The cloud pixels with a large inhomogeneity index ($H_\sigma > 2.5$) showed a broader distribution of retrieved parameters, indicating that cloud inhomogeneity reduces the precision of retrieved particle shape and surface roughness.

In Section 5, a supplementary retrieval of phase functions from Multi-angle Imaging Spectroradiometer (MISR) data showed that phase functions for both column aggregate particle and compact hexagonal column particle fit the observation in the tropics.

This doctoral research project contributes to the better understanding of the particle shape and surface roughness to simulate natural clouds, existing framework of surface roughness simulations, and truncation approximation in polarized radiative

transfer calculations. The response of newly-developed two retrieval methods to instrumental noise is more predictable than the “best-fit” approaches conventionally used.

REFERENCES

Asano, S., and G. Yamamoto (1975), Light-scattering by a spheroidal particle, Appl. Optics, 14(1), 29-49, doi=10.1364/AO.14.000029.

Bailey, M., and J. Hallett (2002), Nucleation effects on the habit of vapour grown ice crystals from -18 to -42 °C, Q. J. R. Meteorol. Soc., 128(583, A), 1461-1483, doi=10.1256/00359000260247318.

Bailey, M., and J. Hallett (2004), Growth rates and habits of ice crystals between -20° and -70 °C, J. Atmos. Sci., 61(5), 514-544, doi=10.1175/1520-0469(2004)061<0514:GRAHOI>2.0.CO;2.

Bailey, M. P., and J. Hallett (2009), A comprehensive habit diagram for atmospheric ice crystals: Confirmation from the laboratory, AIRS II, and other field studies, J. Atmos. Sci., 66(9), 2888-2899, doi=10.1175/2009JAS2883.1.

Baran, A. J., and L. C.-Labonnote (2006), On the reflection and polarisation properties of ice cloud, J. Quant. Spectrosc. Radiat. Transf., 100(1-3), 41-54, doi=10.1016/j.jqsrt.2005.11.062.

Baran, A. J., and L. C.-Labonnote (2007), A self-consistent scattering model for cirrus. I: The solar region, Q. J. R. Meteorol. Soc., 133(629b), 1899-1912, doi=10.1002/qj.164.

Baran, A. J., and P. N. Francis (2004), On the radiative properties of cirrus cloud at solar and thermal wavelengths: A test of model consistency using high-resolution

airborne radiance measurements, Q. J. R. Meteorol. Soc., 130(598a), 763-778, doi=10.1256/qj.03.151.

Baran, A. J., P. D. Watts, and J. S. Foot (1998), Potential retrieval of dominating crystal habit and size using radiance data from a dual-view and multiwavelength instrument: A tropical cirrus anvil case, J. Geophys. Res., 103(D6), 6075-6082, doi=10.1029/97JD03122.

Baum, B. A., A. J. Heymsfield, P. Yang, and S. T. Bedka (2005), Bulk scattering properties for the remote sensing of ice clouds. Part I: Microphysical data and models, J. Appl. Meteorol., 44(12), 1885-1895, doi=10.1175/JAM2308.1.

Baum, B. A., D. P. Kratz, P. Yang, S. C. Ou, Y. X. Hu, P. F. Soulen, and S. C. Tsay (2000), Remote sensing of cloud properties using MODIS airborne simulator imagery during SUCCESS 1. Data and models, J. Geophys. Res., 105(D9), 11767-11780, doi=10.1029/1999JD901089.

Baum, B. A., P. Yang, A. J. Heymsfield, A. Bansemer, B. H. Cole, A. Merrelli, C. Schmitt, and C. Wang (2014), Ice cloud single-scattering property models with the full phase matrix at wavelengths from 0.2 to 100 μm, J. Quant. Spectrosc. Radiat. Transf., 146(SI), 123-139, doi=10.1016/j.jqsrt.2014.02.029.

Baum, B. A., P. Yang, A. J. Heymsfield, C. G. Schmitt, Y. Xie, A. Bansemer, Y.-X. Hu, and Z. Zhang (2011), Improvements in shortwave bulk scattering and absorption models for the remote sensing of ice clouds, J. Appl. Meteorol. Climatol., 50(5), 1037-1056, doi=10.1175/2010JAMC2608.1.

Baum, B. A., P. Yang, Y.-X. Hu, and Q. Feng (2010), The impact of ice particle roughness on the scattering phase matrix, J. Quant. Spectrosc. Radiat. Transf., 111(17-18), 2534-2549, doi=10.1016/j.jqsrt.2010.07.008.

Bi, L., P. Yang, C. Liu, B. Yi, B. A. Baum, B. van Diedenhoven, and H. Iwabuchi (2014), Assessment of the accuracy of the conventional ray-tracing technique: Implications in remote sensing and radiative transfer involving ice clouds, J. Quant. Spectrosc. Radiat. Transf., 146(SI), 158-174, doi=10.1016/j.jqsrt.2014.03.017.

Box, G. E. P., and M. E. Muller (1958), A note on the generation of random normal deviates, Ann. Math. Stat., 29(2), 610-611, doi=10.1214/aoms/1177706645.

Buriez, J. C., C. Vanbauce, F. Parol, P. Goloub, M. Herman, B. Bonnel, Y. Fouquart, P. Couvert, and G. Seze (1997), Cloud detection and derivation of cloud properties from POLDER, Int. J. Remote Sens., 18(13), 2785-2813, doi=10.1080/014311697217332.

Butterfield, N., P. M. Rowe, E. Stewart, D. Roesel, and S. Neshyba (2017), Quantitative three-dimensional ice roughness from scanning electron microscopy, J. Geophys. Res., 122(5), 3023-3041, doi=10.1002/2016JD026094.

Chepfer, H., G. Brogniez, and Y. Fouquart (1998), Cirrus clouds' microphysical properties deduced from POLDER observations, J. Quant. Spectrosc. Radiat. Transf., 60(3), 375-390, doi=10.1016/S0022-4073(98)00013-2.

Chepfer, H., P. Goloub, J. Riedi, J. F. de Haan, J. W. Hovenier, and P. H. Flamant (2001), Ice crystal shapes in cirrus clouds derived from POLDER/ADEOS-1, J. Geophys. Res., 106(D8), 7955-7966, doi=10.1029/2000JD900285.

C.-Labonnote, L., G. Brogniez, J. C. Buriez, M. Doutriaux-Boucher, J. F. Gayet, and A. Macke (2001), Polarized light scattering by inhomogeneous hexagonal monocrystals: Validation with ADEOS-POLDER measurements, J. Geophys. Res., 106(D11), 12139-12153.

Cole, B. H., P. Yang, B. A. Baum, J. Riedi, and L. C.-Labonnote (2014), Ice particle habit and surface roughness derived from PARASOL polarization measurements, Atmos. Chem. Phys., 14(7), 3739-3750, doi=10.5194/acp-14-3739-2014.

Cole, B. H., P. Yang, B. A. Baum, J. Riedi, L. C.-Labonnote, F. Thieuleux, and S. Platnick (2013), Comparison of PARASOL observations with polarized reflectances simulated using different ice habit mixtures, J. Appl. Meteorol. Climatol., 52(1), 186-196, doi=10.1175/JAMC-D-12-097.1.

Cox, C., and W. Munk (1954), Measurement of the roughness of the sea surface from photographs of the suns glitter, , 44(11), 838-850, doi=10.1364/JOSA.44.000838.

Curran, R. J., and M. L. C. Wu (1982), Skylab near-infrared observations of clouds indicating supercooled liquid water droplets, J. Atmos. Sci., 39(3), 635-647, doi=10.1175/1520-0469(1982)039<0635:SNIOOC>2.0.CO;2.

de Haan, J. F., P. B. Bosma, and J. W. Hovenier (1987), The adding method for multiple-scattering calculations of polarized-light, Astron. Astrophys., 183(2), 371-391.

Deirmendjian, D. (1964), Scattering and polarization properties of water clouds and hazes in visible and infrared, Appl. Optics, 3(2), 187-196, doi=10.1364/AO.3.000187.

Deschamps, P. Y., F. M. Breon, M. Leroy, A. Podaire, A. Bricaud, J. C. Buriez, and G. Seze (1994), The POLDER mission - Instrument characteristics and scientific objectives, IEEE Trans. Geosci. Remote Sensing, 32(3), 598-615, doi=10.1109/36.297978.

Diner, D. J., J. C. Beckert, T. H. Reilly, C. J. Bruegge, J. E. Conel, R. A. Kahn, J. V. Martonchik, T. P. Ackerman, R. Davies, S. A. W. Gerstl, H. R. Gordon, J. P. Muller, R. B. Myneni, P. J. Sellers, B. Pinty, and M. M. Verstraete (1998), Multi-angle imaging spectroradiometer (MISR) - Instrument description and experiment overview, IEEE Trans. Geosci. Remote Sensing, 36(4), 1072-1087, doi=10.1109/36.700992.

Ding, J., P. Yang, G. W. Kattawar, M. D. King, S. Platnick, and K. G. Meyer (2017), Validation of quasi-invariant ice cloud radiative quantities with MODIS satellite-based cloud property retrievals, J. Quant. Spectrosc. Radiat. Transf., 194, 47-57, doi=10.1016/j.jqsrt.2017.03.025.

Doutriaux-Boucher, M., J. C. Buriez, G. Brogniez, L. C. Labonnote, and A. J. Baran (2000), Sensitivity of retrieved POLDER directional cloud optical thickness to various ice particle models, Geophys. Res. Lett., 27(1), 109-112, doi=10.1029/1999GL010870.

Ebert, E. E., and J. A. Curry (1992), A parameterization of ice-cloud optical-properties for climate models, J. Geophys. Res., 97(D4), 3831-3836, doi=10.1029/91JD02472.

Evans, M. J., and J. S. Rosenthal (2010), Probability and statistics: The science of uncertainty, 2nd ed., New York, NY: W. H. Freeman and Company.

Fougnie, B., G. Bracco, B. Lafrance, C. Ruffel, O. Hagolle, and C. Tinell (2007), PARASOL in-flight calibration and performance, Appl. Optics, 46(22), 5435-5451, doi=10.1364/AO.46.005435.

Fritz, S., and H. Wexler (1960), Cloud pictures from satellite TIROS I, Mon. Weather Rev., 88(3), 79-87.

Fu, Q. A. (1996), An accurate parameterization of the solar radiative properties of cirrus clouds for climate models, J. Clim., 9(9), 2058-2082, doi=10.1175/1520-0442(1996)009<2058:AAPOTS>2.0.CO;2.

Fu, Q., and K. N. Liou (1993), Parameterization of the radiative properties of cirrus clouds, J. Atmos. Sci., 50(13), 2008-2025, doi=10.1175/1520-0469(1993)050<2008:POTRPO>2.0.CO;2.

Fu, Q., P. Yang, and W. B. Sun (1998), An accurate parameterization of the infrared radiative properties of cirrus clouds for climate models, J. Clim., 11(9), 2223-2237, doi=10.1175/1520-0442(1998)011<2223:AAPOTI>2.0.CO;2.

Geogdzhayev, I., and B. van Diedenhoven (2016), The effect of roughness model on scattering properties of ice crystals, J. Quant. Spectrosc. Radiat. Transf., 178(SI), 134-141, doi=10.1016/j.jqsrt.2016.03.001.

Goloub, P., J. L. Deuze, M. Herman, and Y. Fouquart (1994), Analysis of the POLDER polarization measurements performed over cloud covers, IEEE Trans. Geosci. Remote Sensing, 32(1), 78-88, doi=10.1109/36.285191.

Goloub, P., M. Herman, H. Chepfer, J. Riedi, G. Brogniez, P. Couvert, and G. Seze (2000), Cloud thermodynamical phase classification from the POLDER spaceborne instrument, J. Geophys. Res., 105(D11), 14747-14759, doi=10.1029/1999JD901183.

Grenfell, T. C., and S. G. Warren (1999), Representation of a nonspherical ice particle by a collection of independent spheres for scattering and absorption of radiation, J. Geophys. Res., 104(D24), 31697-31709, doi=10.1029/1999JD900496.

Heymsfield, A. J., and J. Iaquinta (2000), Cirrus crystal terminal velocities, J. Atmos. Sci., 57(7), 916-938, doi=10.1175/1520-0469(2000)057<0916:CCTV>2.0.CO;2.

Heymsfield, A. J., A. Bansemer, P. R. Field, S. L. Durden, J. L. Stith, J. E. Dye, W. Hall, and C. A. Grainger (2002), Observations and parameterizations of particle size distributions in deep tropical cirrus and stratiform precipitating clouds: Results from in situ observations in TRMM field campaigns, J. Atmos. Sci., 59(24), 3457-3491, doi=10.1175/1520-0469(2002)059<3457:OAPOPS>2.0.CO;2.

Heymsfield, A. J., C. Schmitt, and A. Bansemer (2013), Ice cloud particle size distributions and pressure-dependent terminal velocities from in situ observations at temperatures from 0° to -86°C, J. Atmos. Sci., 70(12), 4123-4154, doi=10.1175/JAS-D-12-0124.1.

Holz, R. E., S. Platnick, K. Meyer, M. Vaughan, A. Heidinger, P. Yang, G. Wind, S. Dutcher, S. Ackerman, N. Amarasinghe, F. Nagle, and C. Wang (2016), Resolving ice cloud optical thickness biases between CALIOP and MODIS using infrared retrievals, Atmos. Chem. Phys., 16(8), 5075-5090, doi=10.5194/acp-16-5075-2016.

Hong, G., P. Yang, B. A. Baum, A. J. Heymsfield, and K.-M. Xu (2009), Parameterization of shortwave and longwave radiative properties of ice clouds for use in climate models, J. Clim., 22(23), 6287-6312, doi=10.1175/2009JCLI2844.1.

Houghton, J. T., and G. E. Hunt (1971), Detection of ice clouds from remote measurements of their emission in far infra-red, Q. J. R. Meteorol. Soc., 97(411), 1-17.

Houghton, J. T., and S. D. Smith (1970), Remote sounding of atmospheric temperature from satellites .1. Introduction, Proc. Royal Soc. A, 320(1540), 23-33, doi=10.1098/rspa.1970.0195.

Hovenier, J. W., C. V. M. van der Mee, and H. Domke (2004), Transfer of polarized light in planetary atmospheres: Basic concepts and practical methods, Dordrechet, The Netherlands: Kluwer.

Huang, X., P. Yang, G. Kattawar, and K.-N. Liou (2015), Effect of mineral dust aerosol aspect ratio on polarized reflectance, J. Quant. Spectrosc. Radiat. Transf., 151, 97-109, doi=10.1016/j.jqsrt.2014.09.014.

Hu, Y. X., B. Wielicki, B. Lin, G. Gibson, S. C. Tsay, K. Stamnes, and T. Wong (2000), Delta-fit: A fast and accurate treatment of particle scattering phase functions with weighted singular-value decomposition least-squares fitting, J. Quant. Spectrosc. Radiat. Transf., 65(4), 681-690, doi=10.1016/S0022-4073(99)00147-8.

Inoue, T. (1987), A cloud type classification with noaa 7 split-window measurements, J. Geophys. Res., 92(D4), 3991-4000, doi=10.1029/JD092iD04p03991.

Iwabuchi, H., and T. Suzuki (2009), Fast and accurate radiance calculations using truncation approximation for anisotropic scattering phase functions, J. Quant. Spectrosc. Radiat. Transf., 110(17), 1926-1939, doi=10.1016/j.jqsrt.2009.04.006.

Kikuchi, K., T. Kameda, K. Higuchi, A. Yamashita, and . Working grp members for new classification of snow Crystals} (2013), A global classification of snow crystals, ice crystals, and solid precipitation based on observations from middle latitudes to polar regions, Atmos. Res., 132, 460-472, doi=10.1016/j.atmosres.2013.06.006.

Knap, W. H., L. C.-Labonnote, G. Brogniez, and P. Stammes (2005), Modeling total and polarized reflectances of ice clouds: Evaluation by means of POLDER and ATSR-2 measurements, Appl. Optics, 44(19), 4060-4073, doi=10.1364/AO.44.004060.

King, M. D., W. P. Menzel, Y. J. Kaufman, D. Tanre, B. C. Gao, S. Platnick, S. A. Ackerman, L. A. Remer, R. Pincus, and P. A. Hubanks (2003), Cloud and aerosol properties, precipitable water, and profiles of temperature and water vapor from MODIS, IEEE Trans. Geosci. Remote Sensing, 41(2), 442-458, doi=10.1109/TGRS.2002.808226.

King, M. D., S. Platnick, P. Yang, G. T. Arnold, M. A. Gray, J. C. Riedi, S. A. Ackerman, and K. N. Liou (2004), Remote sensing of liquid water and ice cloud optical thickness and effective radius in the arctic: Application of airborne multispectral MAS data, J. Atmos. Ocean. Technol., 21(6), 857-875, doi=10.1175/1520-0426(2004)021<0857:RSOLWA>2.0.CO;2.

Kobayashi, T. (1957), Experimental researches on the snow crystal habit and growth by means of a diffusion cloud chamber, J. Meteorol. Soc. Jpn., 35, 38-47.

Lawson, R. P., B. Baker, B. Pilson, and Q. Mo (2006), In situ observations of the microphysical properties of wave, cirrus, and anvil clouds. Part II: Cirrus clouds, J. Atmos. Sci., 63(12), 3186-3203, doi=10.1175/JAS3803.1.

Liang, L., L. Di Girolamo, and S. Platnick (2009), View-angle consistency in reflectance, optical thickness and spherical albedo of marine water-clouds over the northeastern pacific through MISR-MODIS fusion, Geophys. Res. Lett., 36, L09811, doi=10.1029/2008GL037124.

Liou, K. N. (1972), Electromagnetic scattering by arbitrarily oriented ice cylinders, Appl. Optics, 11(3), 667-674, doi=10.1364/AO.11.000667.

Liou, K. N. (1972), Light-scattering by ice clouds in visible and infrared - Theoretical study, J. Atmos. Sci., 29(3), 524-536, doi=10.1175/1520-0469(1972)029<0524:LSBICI>2.0.CO;2.

Liou, K. N. (1973), Transfer of solar irradiance through cirrus cloud layers, J. Geophys. Res., 78(9), 1409-1418, doi=10.1029/JC078i009p01409.

Liou, K. N., and G. D. Wittman (1979), Parameterization of the radiative properties of clouds, J. Atmos. Sci., 36(7), 1261-1273, doi=10.1175/1520-0469(1979)036<1261:POTRPO>2.0.CO;2.

Liu, C., P. Yang, P. Minnis, N. Loeb, S. Kato, A. Heymsfield, and C. Schmitt (2014), A two-habit model for the microphysical and optical properties of ice clouds, Atmos. Chem. Phys., 14(24), 13719-13737, doi=10.5194/acp-14-13719-2014.

Loeb, N. G., P. Yang, F. G. Rose, G. Hong, S. Sun-Mack, P. Minnis, S. Kato, S.-H. Ham, J. Smith, S. Hioki, and G. Tang (2018), Impact of ice cloud microphysics on

satellite cloud retrievals and broadband flux radiative transfer model calculations, J. Clim., 31(5), 1851-1864, doi=10.1175/JCLI-D-17-0426.1.

Macke, A., and M. I. Mishchenko (1996), Applicability of regular particle shapes in light scattering calculations for atmospheric ice particles, Appl. Optics, 35(21), 4291-4296, doi=10.1364/AO.35.004291.

Macke, A., J. Mueller, and E. Raschke (1996), Single scattering properties of atmospheric ice crystals, J. Atmos. Sci., 53(19), 2813-2825, doi=10.1175/1520-0469(1996)053<2813:SSPOAI>2.0.CO;2.

Manabe, S., and R. T. Wetheral (1967), Thermal equilibrium of atmosphere with a given distribution of relative humidity, J. Atmos. Sci., 24(3), 241-259, doi=10.1175/1520-0469(1967)024<0241:TEOTAW>2.0.CO;2.

Mapes, B. E., and R. A. Houze (1993), Cloud clusters and superclusters over the oceanic warm pool, Mon. Weather Rev., 121(5), 1398-1415, doi=10.1175/1520-0493(1993)121<1398:CCASOT>2.0.CO;2.

Marshak, A., T. Varnai, and A. Kostinski (2017), Terrestrial glint seen from deep space: Oriented ice crystals detected from the lagrangian point, Geophys. Res. Lett., 44(10), 5197-5202, doi=10.1002/2017GL073248.

Masuda, K., and H. Ishimoto (2004), Influence of particle orientation on retrieving cirrus cloud properties by use of total and polarized reflectances from satellite measurements, J. Quant. Spectrosc. Radiat. Transf., 85(2), 183-193, doi=10.1016/S0022-4073(03)00224-3.

Masuda, K., and T. Takashima (1992), Feasibility study of derivation of cirrus information using polarimetric measurements from satellite, Remote Sens. Environ., 39(1), 45-59, doi=10.1016/0034-4257(92)90139-B.

Masuda, K., H. Ishimoto, and T. Takashima (2002), Retrieval of cirrus optical thickness and ice-shape information using total and polarized reflectance from satellite measurements, J. Quant. Spectrosc. Radiat. Transf., 75(1), 39-51, doi=10.1016/S0022-4073(01)00291-6.

Mcfarlane, S. A., R. T. Marchand, and T. P. Ackerman (2005), Retrieval of cloud phase and crystal habit from multiangle imaging spectroradiometer (MISR) and moderate resolution imaging spectroradiometer (MODIS) data, J. Geophys. Res., 110(D14), D14201, doi=10.1029/2004JD004831.

Mckellar, B. H. J., and M. A. Box (1981), The scaling group of the radiative-transfer equation, J. Atmos. Sci., 38(5), 1063-1068, doi=10.1175/1520-0469(1981)038<1063:TSGOTR>2.0.CO;2.

Minnis, P., D. P. Garber, D. F. Young, and R. F. Arduini (1998), Parameterizations of reflectance and effective emittance for satellite remote sensing of cloud properties, J. Atmos. Sci., 55(22), 3313-3339, doi=10.1175/1520-0469(1998)055<3313:PORAEE>2.0.CO;2.

Minnis, P., P. W. Heck, and D. F. Young (1993), Inference of cirrus cloud properties using satellite-observed visible and infrared radiances .2. Verification of theoretical cirrus radiative properties, J. Atmos. Sci., 50(9), 1305-1322, doi=10.1175/1520-0469(1993)050<1305:IOCCPU>2.0.CO;2.

Minnis, P., S. Sun-Mack, D. F. Young, P. W. Heck, D. P. Garber, Y. Chen, D. A. Spangenberg, R. F. Arduini, Q. Z. Trepte, J. Smith, J. K. Ayers, S. C. Gibson, W. F. Miller, G. Hong, V. Chakrapani, Y. Takano, K.-N. Liou, Y. Xie, and P. Yang (2011), CERES Edition-2 cloud property retrievals using TRMM VIRS and Terra and Aqua MODIS data-Part I: Algorithms, IEEE Trans. Geosci. Remote Sensing, 49(11, 2), 4374-4400, doi=10.1109/TGRS.2011.2144601.

Mitchell, D. L., A. Macke, and Y. G. Liu (1996), Modeling cirrus clouds. Part II: Treatment of radiative properties, J. Atmos. Sci., 53(20), 2967-2988, doi=10.1175/1520-0469(1996)053<2967:MCCPIT>2.0.CO;2.

Mitrescu, C., and G. L. Stephens (2004), On similarity and scaling of the radiative transfer equation, J. Quant. Spectrosc. Radiat. Transf., 86(4), 387-394, doi=10.1016/j.jqsrt.2003.12.028.

Morrison, H., J. A. Curry, and V. I. Khvorostyanov (2005), A new double-moment microphysics parameterization for application in cloud and climate models. Part I: Description, J. Atmos. Sci., 62(6), 1665-1677, doi=10.1175/JAS3446.1.

Nakajima, T., and M. D. King (1990), Determination of the optical-thickness and effective particle radius of clouds from reflected solar-radiation measurements. Part I: Theory, J. Atmos. Sci., 47(15), 1878-1893, doi=10.1175/1520-0469(1990)047<1878:DOTOTA>2.0.CO;2.

Nakajima, T., and M. Tanaka (1988), Algorithms for radiative intensity calculations in moderately thick atmospheres using a truncation approximation, J. Quant. Spectrosc. Radiat. Transf., 40(1), 51-69, doi=10.1016/0022-4073(88)90031-3.

Nakaya, U. (1951), The formation of ice crystals, Compendium of Meteorology, Malone, T. F. Ed., Boston, MA: American Meteorological Society.

Neale, R. B., C.-C. Chen, A. Gettelman, P. H. A. P. Lauritzen, D. L. Williamson, A. J. Conley, R. Garcia, D. A. L. Kinnison, D. March, M. Mills, A. K. Smith, S. A. V. Tilmes, H. Morrison, P. Cameron-Smith, W. D. Collins, M. J. A. E. Iacono, S. J. Ghan, X. Liu, P. J. Rasch, and M. A. Taylor (2012), Description of the NCAR Community Atmosphere Model (CAM 5.0): Ncar technical note ncar/tn-486+str, Boulder, CO: National Center for Atmospheric Research, http://www.cesm.ucar.edu/models/cesm1.0/cam/docs/description/cam5_desc.pdf, Accessed on April 23, 2018.

Neshyba, S. P., B. Lowen, M. Benning, A. Lawson, and P. M. Rowe (2013), Roughness metrics of prismatic facets of ice, J. Geophys. Res., 118(8), 3309-3318, doi=10.1002/jgrd.50357.

Noel, V., and K. Sassen (2005), Study of planar ice crystal orientations in ice clouds from scanning polarization lidar observations, J. Appl. Meteorol., 44(5), 653-664, doi=10.1175/JAM2223.1.

Oreopoulos, L., S. Platnick, G. Hong, P. Yang, and R. F. Cahalan (2009), The shortwave radiative forcing bias of liquid and ice clouds from MODIS observations, Atmos. Chem. Phys., 9(16), 5865-5875.

Parol, F., J. C. Buriez, C. Vanbauce, P. Couvert, G. Seze, P. Goloub, and S. Cheinet (1999), First results of the POLDER "earth radiation budget and clouds"

operational algorithm, IEEE Trans. Geosci. Remote Sensing, 37(3, 2), 1597-1612, doi=10.1109/36.763273.

Platnick, S., M. D. King, S. A. Ackerman, W. P. Menzel, B. A. Baum, J. C. Riedi, and R. A. Frey (2003), The MODIS cloud products: Algorithms and examples from Terra, IEEE Trans. Geosci. Remote Sensing, 41(2), 459-473, doi=10.1109/TGRS.2002.808301.

Platnick, S., K. G. Meyer, M. D. King, G. Wind, N. Amarasinghe, B. Marchant, G. T. Arnold, Z. Zhang, P. A. Hubanks, R. E. Holz, P. Yang, W. L. Ridgway, and J. Riedi (2017), The MODIS cloud optical and microphysical products: Collection 6 updates and examples from Terra and Aqua, IEEE Trans. Geosci. Remote Sensing, 55(1), 502-525, doi=10.1109/TGRS.2016.2610522.

Platt, C. M. R. (1983), On the bispectral method for cloud parameter determination from satellite VISSR data - Separating broken cloud and semitransparent cloud, J. Clim. Appl. Meteorol., 22(3), 429-439, doi=10.1175/1520-0450(1983)022<0429:OTBMFC>2.0.CO;2.

Potter, J. F. (1970), Delta function approximation in radiative transfer theory, J. Atmos. Sci., 27(6), 943-949, doi=10.1175/1520-0469(1970)027<0943:TDFAIR>2.0.CO;2.

Reynolds, D. W., and T. H. Vonder Haar (1977), Bispectral method for cloud parameter determination, Mon. Weather Rev., 105(4), 446-457, doi=10.1175/1520-0493(1977)105<0446:ABMFCP>2.0.CO;2.

Riedi, J., B. Marchant, S. Platnick, B. A. Baum, F. Thieuleux, C. Oudard, F. Parol, J.-M. Nicolas, and P. Dubuisson (2010), Cloud thermodynamic phase inferred from merged POLDER and MODIS data, Atmos. Chem. Phys., 10(23), 11851-11865, doi=10.5194/acp-10-11851-2010.

Rodgers, C. D. (2010), Inverse methods for atmospheric sounding: Theory and practice, Singapore: World Scientific Publishing.

Rolland, P., K. N. Liou, M. D. King, S. C. Tsay, and G. M. Mcfarquhar (2000), Remote sensing of optical and microphysical properties of cirrus clouds using moderate-resolution imaging spectroradiometer channels: Methodology and sensitivity to physical assumptions, J. Geophys. Res., 105(D9), 11721-11738, doi=10.1029/2000JD900028.

Rozanov, V. V., and A. I. Lyapustin (2010), Similarity of radiative transfer equation: Error analysis of phase function truncation techniques, J. Quant. Spectrosc. Radiat. Transf., 111(12-13), 1964-1979, doi=10.1016/j.jqsrt.2010.03.018.

Sanghavi, S., and G. Stephens (2015), Adaptation of the delta-M and delta-fit truncation methods to vector radiative transfer: Effect of truncation on radiative transfer accuracy, J. Quant. Spectrosc. Radiat. Transf., 159, 53-68, doi=10.1016/j.jqsrt.2015.03.007.

Sassen, K. (1980), Remote sensing of planar ice crystal fall attitudes, J. Meteorol. Soc. Jpn., 58, 422-433.

Shenk, W. E., and R. J. Curran (1973), A multi-spectral method for estimating cirrus cloud top heights, J. Appl. Meteorol., 12(7), 1213-1216.

Slingo, A. (1989), A GCM parameterization for the shortwave radiative properties of water clouds, J. Atmos. Sci., 46(10), 1419-1427, doi=10.1175/1520-0469(1989)046<1419:AGPFTS>2.0.CO;2.

Slingo, A., and H. M. Schrecker (1982), On the shortwave radiative properties of stratiform water clouds, Q. J. R. Meteorol. Soc., 108(456), 407-426, doi=10.1256/smsqj.45606.

Sobolev, V. V. (1975), Approximate formulas, Light scattering in plaentary atmospheres, Oxford, United Kingdom: Pergamon Press.

Sourdeval, O., L. C. Labonnote, A. J. Baran, and G. Brogniez (2015), A methodology for simultaneous retrieval of ice and liquid water cloud properties. Part I: Information content and case study, Q. J. R. Meteorol. Soc., 141(688, A), 870-882, doi=10.1002/qj.2405.

Stephens, G. L. (1980), Radiative properties of cirrus clouds in the infrared region, J. Atmos. Sci., 37(2), 435-446, doi=10.1175/1520-0469(1980)037<0435:RPOCCI>2.0.CO;2.

Stephens, G. L. (1980), Radiative-transfer on a linear lattice - Application to anisotropic ice crystal clouds, J. Atmos. Sci., 37(9), 2095-2104, doi=10.1175/1520-0469(1980)037<2095:RTOALL>2.0.CO;2.

Stroud, W. G. (1960), Initial results of the TIROS I meteorological satellite, J. Geophys. Res., 65(5), 1643-1644, doi=10.1029/JZ065i005p01643.

Takano, Y., and K. N. Liou (1989), Solar radiative transfer in cirrus clouds. Part I: Single-scattering and optical properties of hexagonal ice crystals, J. Atmos. Sci., 46(1), 3-19, doi=10.1175/1520-0469(1989)046<0003:SRTICC>2.0.CO;2.

Ulanowski, Z., E. Hesse, P. H. Kaye, and A. J. Baran (2006), Light scattering by complex ice-analogue crystals, J. Quant. Spectrosc. Radiat. Transf., 100(1-3), 382-392, doi=10.1016/j.jqsrt.2005.11.052.

Ulanowski, Z., P. H. Kaye, E. Hirst, R. S. Greenaway, R. J. Cotton, E. Hesse, and C. T. Collier (2014), Incidence of rough and irregular atmospheric ice particles from small ice detector 3 measurements, Atmos. Chem. Phys., 14(3), 1649-1662, doi=10.5194/acp-14-1649-2014.

Um, J., and G. M. Mcfarquhar (2007), Single-scattering properties of aggregates of bullet rosettes in cirrus, J. Appl. Meteorol. Climatol., 46(6), 757-775, doi=10.1175/JAM2501.1.

Um, J., and G. M. Mcfarquhar (2009), Single-scattering properties of aggregates of plates, Q. J. R. Meteorol. Soc., 135(639), 291-304, doi=10.1002/qj.378.

van Diedenhoven, B., B. Cairns, I. V. Geogdzhayev, A. M. Fridlind, A. S. Ackerman, P. Yang, and B. A. Baum (2012), Remote sensing of ice crystal asymmetry parameter using multi-directional polarization measurements - Part 1: Methodology and evaluation with simulated measurements, Atmos. Meas. Tech., 5(10), 2361-2374, doi=10.5194/amt-5-2361-2012.

van Diedenhoven, B., A. M. Fridlind, B. Cairns, and A. S. Ackerman (2014), Variation of ice crystal size, shape, and asymmetry parameter in tops of tropical deep

convective clouds, J. Geophys. Res., 119(20), 11809-11825, doi=10.1002/2014JD022385.

Wait, J. R. (1955), Scattering of a plane wave from a circular dielectric cylinder at oblique incidence, Can. J. Phys., 33(5), 189-195, doi=10.1139/p55-024.

Waliser, D. E., J.-L. F. Li, C. P. Woods, R. T. Austin, J. Bacmeister, J. Chern, A. Del Genio, J. H. Jiang, Z. Kuang, H. Meng, P. Minnis, S. Platnick, W. B. Rossow, G. L. Stephens, S. Sun-Mack, W.-K. Tao, A. M. Tompkins, D. G. Vane, C. Walker, and D. Wu (2009), Cloud ice: A climate model challenge with signs and expectations of progress, J. Geophys. Res., 114, D00A21, doi=10.1029/2008JD010015.

Wiscombe, W. J. (1977), Delta-m method - Rapid yet accurate radiative flux calculations for strongly asymmetric phase functions, J. Atmos. Sci., 34(9), 1408-1422, doi=10.1175/1520-0469(1977)034<1408:TDMRYA>2.0.CO;2.

Xie, Y., P. Yang, G. W. Kattawar, P. Minnis, and Y. X. Hu (2009), Effect of the inhomogeneity of ice crystals on retrieving ice cloud optical thickness and effective particle size, J. Geophys. Res., 114, D11203, doi=10.1029/2008JD011216.

Yang, P., and K. N. Liou (1996), Geometric-optics-integral-equation method for light scattering by nonspherical ice crystals, Appl. Optics, 35(33), 6568-6584, doi=10.1364/AO.35.006568.

Yang, P., and K. N. Liou (1998), Single-scattering properties of complex ice crystals in terrestrial atmosphere, Contrib. Atmos. Phys., 71(2), 223-248.

Yang, P., G. Hong, G. W. Kattawar, P. Minnis, and Y. Hu (2008), Uncertainties associated with the surface texture of ice particles in satellite-based retrieval of cirrus

clouds: Part II - Effect of particle surface roughness on retrieved cloud optical thickness and effective particle size, IEEE Trans. Geosci. Remote Sensing, 46(7), 1948-1957, doi=10.1109/TGRS.2008.916472.

Yang, P., L. Bi, B. A. Baum, K.-N. Liou, G. W. Kattawar, M. I. Mishchenko, and B. Cole (2013), Spectrally consistent scattering, absorption, and polarization properties of atmospheric ice crystals at wavelengths from 0.2 to 100 μm, J. Atmos. Sci., 70(1), 330-347, doi=10.1175/JAS-D-12-039.1.

Yang, P., G. W. Kattawar, G. Hong, P. Minnis, and Y. Hu (2008), Uncertainties associated with the surface texture of ice particles in satellite-based retrieval of cirrus clouds - Part I: Single-scattering properties of ice crystals with surface roughness, IEEE Trans. Geosci. Remote Sensing, 46(7), 1940-1947, doi=10.1109/TGRS.2008.916471.

Yang, P., K. N. Liou, K. Wyser, and D. Mitchell (2000), Parameterization of the scattering and absorption properties of individual ice crystals, J. Geophys. Res., 105(D4), 4699-4718, doi=10.1029/1999JD900755.

Yang, P., H. L. Wei, H. L. Huang, B. A. Baum, Y. X. Hu, G. W. Kattawar, M. I. Mishchenko, and Q. Fu (2005), Scattering and absorption property database for nonspherical ice particles in the near- through far-infrared spectral region, Appl. Optics, 44(26), 5512-5523, doi=10.1364/AO.44.005512.

Yang, P., L. Zhang, G. Hong, S. L. Nasiri, B. A. Baum, H.-L. Huang, M. D. King, and S. Platnick (2007), Differences between collection 4 and 5 MODIS ice cloud optical/microphysical products and their impact on radiative forcing simulations, IEEE Trans. Geosci. Remote Sensing, 45(9), 2886-2899, doi=10.1109/TGRS.2007.898276.

Yurkin, M. A., V. P. Maltsev, and A. G. Hoekstra (2007), The discrete dipole approximation for simulation of light scattering by particles much larger than the wavelength, J. Quant. Spectrosc. Radiat. Transf., 106(1-3), 546-557, doi=10.1016/j.jqsrt.2007.01.033.

Zhai, P.-W., Y. Hu, C. R. Trepte, and P. L. Lucker (2009), A vector radiative transfer model for coupled atmosphere and ocean systems based on successive order of scattering method, Opt. Express, 17(4), 2057-2079, doi=10.1364/OE.17.002057.

Zhang, Z., P. Yang, G. Kattawar, J. Riedi, L. C. Labonnote, B. A. Baum, S. Platnick, and H. .-L. Huang (2009), Influence of ice particle model on satellite ice cloud retrieval: Lessons learned from MODIS and POLDER cloud product comparison, Atmos. Chem. Phys., 9(18), 7115-7129.

Zhou, C., P. Yang, A. E. Dessler, Y. Hu, and B. A. Baum (2012), Study of horizontally oriented ice crystals with CALIPSO observations and comparison with Monte Carlo radiative transfer simulations, J. Appl. Meteorol. Climatol., 51(7), 1426-1439, doi=10.1175/JAMC-D-11-0265.1.

APPENDIX A

DERIVATION OF THE DENSITY FUNCTIONS OF THE TILT ANGLE DISTRIBUTION USED IN MACKE'S LIGHT SCATTERING PROGRAM

A.1 Implementation in Macke's code

The geometric optics computer program by Macke et al. (1996) is publicly available from the following web site: http://tools.tropos.de/. The probability density function (PDF) and cumulative distribution function (CDF) derived in this appendix is based on the "tilt" subroutine of the distributed computer programs.

In the "tilt" subroutine, the new direction of the beam $\vec{k} = \left(k_x, k_y, k_z\right)^T$ is determined from the original direction of the beam $\overrightarrow{k_0} = \left(k_{0x}, k_{0y}, k_{0z}\right)^T$ by the following formula:

$$\vec{k} = \frac{\overrightarrow{k_0} + \left(2\vec{U} - 1\right)\alpha}{\left|\overrightarrow{k_0} + \left(2\vec{U} - 1\right)\alpha\right|}. \tag{A.1}$$

where $\vec{U} = (U_1, U_2, U_3)^T$ and α is the distortion parameter specified by a user. U_1, U_2 and U_3 are random variable following identical and independent uniform distribution spanning from 0 to 1 (i.e. $U_1, U_2, U_3 \sim \text{Uniform}(0,1), i.i.d.$).

The distribution of tilt angle depends on the original direction of the beam $\overrightarrow{k_0}$ because the probability density function of vector $\vec{U}$ is not isotropic. This implementation is not physical because the magnitude of roughness depends on the rotation of coordinate system to. In this Appendix, I derive the CDF and PDF for a fixed incident direction. A Monte Carlo simulation shows that the distribution of tilt angle for

a fixed $\overrightarrow{k_0}$ is a good approximation for the distribution for completely random $\overrightarrow{k_0}$. I fixed the incident direction at $\overrightarrow{k_0} = (0,0,1)^T$ because the direction of incident beam is fixed at $\overrightarrow{k_0} = (0,0,-1)^T$ in Macke's code. This selection implies that derived CDF and PDF are for initial reflection/refraction event.

When assuming $\overrightarrow{k_0} = (0,0,1)^T$, cosine of tilt angle the angle θ can be written with samples u_1, u_2 and u_3 from random variables U_1, U_2 and U_3 as follows:

$$\cos\theta = \vec{k} \cdot \overrightarrow{k_0}$$

$$= \frac{(2u-1)\alpha + 1}{\sqrt{(2u_1-1)^2\alpha^2 + (2u_2-1)^2\alpha^2 + \left((2u_3-1)\alpha+1\right)^2}}. \tag{A.2}$$

Assuming that distortion parameter is not zero,

$$\cos\theta = \vec{k} \cdot \overrightarrow{k_0} = \frac{u_3 - \frac{1}{2} + \frac{1}{2\alpha}}{\sqrt{\left(u_1 - \frac{1}{2}\right)^2 + \left(u_2 - \frac{1}{2}\right)^2 + \left(u_3 - \frac{1}{2} + \frac{1}{2\alpha}\right)^2}}. \tag{A.3}$$

As the slope ($s = \tan\theta$) and cosine of tilt angle ($\cos\theta$) are related by

$$1 + s^2 = \frac{1}{\cos^2\theta}, \tag{A.4}$$

the slope can be written with the random variables U_1, U_2 and U_3 as follows:

$$\mathrm{s} = \frac{\sqrt{\left(u_1 - \frac{1}{2}\right)^2 + \left(u_2 - \frac{1}{2}\right)^2}}{\sqrt{\left(u_3 - \frac{1}{2} + \frac{1}{2\alpha}\right)^2}}. \tag{A.5}$$

A new random variable S_{M1} is defined as follows:

$$S_{M1} = \frac{\sqrt{\left(U_1 - \frac{1}{2}\right)^2 + \left(U_2 - \frac{1}{2}\right)^2}}{\sqrt{\left(U_3 - \frac{1}{2} + \frac{1}{2\alpha}\right)^2}}. \tag{A.6}$$

In the following parts of this appendix, the PDF and CDF of variable S_{M1} are discussed. For the sake of simplification, following two new random variables X and Y are defined:

$$\mathrm{X} = \sqrt{\left(U_1 - \frac{1}{2}\right)^2 + \left(U_2 - \frac{1}{2}\right)^2} \tag{A.7}$$

$$\mathrm{Y} = \frac{1}{\sqrt{\left(U_3 - \frac{1}{2} + \frac{1}{2\alpha}\right)^2}}. \tag{A.8}$$

Using these two new random variables, $S_{M1} = XY$. To obtain the PDF and CDF for S_{M1}, PDFs and CDFs of X and Y are investigated in this subsection.

A.2 PDF and CDF of component *X*

From the definition of CDF, the CDF of $U_1' = \left(U_1 - \frac{1}{2}\right)^2$ can be written as probability of U_1 satisfying a specific condition:

$$F_{U_1'}(u_1) = \mathrm{P}\left[\left(U_1 - \tfrac{1}{2}\right)^2 \le u_1\right] = 2\mathrm{P}[U_1 < \sqrt{u_1}] - 1. \tag{A.9}$$

It is obvious that the CDF of uniform distribution is a linear curve. Thus,

$$F_{U_1'}(u_1) = \begin{cases} 0 & u_1 \le 0 \\ 2\sqrt{u_1} & 0 < u_1 \le 1/4. \\ 1 & 1/4 < u_1 \end{cases} \tag{A.10}$$

Similarly,

$$F_{U_2'}(u_2) = \begin{cases} 0 & u_2 \le 0 \\ 2\sqrt{u_2} & 0 < u_2 \le 1/4. \\ 1 & 1/4 < u_2 \end{cases} \tag{A.11}$$

Therefore, CDF of X^2 can be written as follows:

$$F_{X^2}(x) = P(X^2 \le x) = \iint_{U_1'+U_2' \le x} f_{U_1'}(u_1) f_{U_2'}(u_2)\ dS \tag{A.12}$$

where $f_{U_1'}(u_1)$ and $f_{U_2'}(u_2)$ are PDFs:

$$f_{U_1'}(u_1) = \frac{dF_{U_1'}}{du_1} = \begin{cases} 0 & u_1 \le 0 \\ 1/\sqrt{u_1} & 0 < u_1 \le 1/4, \\ 0 & 1/4 < u_1 \end{cases} \tag{A.13}$$

$$f_{U_2'}(u_2) = \frac{dF_{U_2'}}{du_2} = \begin{cases} 0 & u_2 \le 0 \\ 1/\sqrt{u_2} & 0 < u_2 \le 1/4. \\ 1 & 1/4 < u_2 \end{cases} \tag{A.14}$$

The CDF of X^2 is finally:

$$F_{X^2}(x) = \begin{cases} 0 & x \le 0 \\ \pi x^2 & 0 < x \le \dfrac{1}{2} \\ 2\displaystyle\int_{1/4}^{x} \sin^{-1}\left(\frac{1}{2u} - 1\right) du + \frac{\pi}{4} & \dfrac{1}{2} < x \le \dfrac{1}{\sqrt{2}}. \\ 1 & \dfrac{1}{\sqrt{2}} \le x \end{cases} \tag{A.15}$$

Therefore, the CDF of X is obtained as follows:

$$F_X(x) = P(X^2 \le x^2) = \begin{cases} 0 & x \le 0 \\ \pi x^2 & 0 < x \le \frac{1}{2} \\ 2\int_{1/4}^{x^2} \sin^{-1}\left(\frac{1}{2u} - 1\right) du + \frac{\pi}{4} & \frac{1}{2} < x \le \frac{1}{\sqrt{2}} \\ 1 & \frac{1}{\sqrt{2}} \le x \end{cases}. \quad \text{(A.16)}$$

To evaluate the integral we first change the variable from u to $u = t^2$.

$$2\int_{1/4}^{x^2} \sin^{-1}\left(\frac{1}{2u} - 1\right) du = 4\int_{1/2}^{x} t \sin^{-1}\left(\frac{1}{2t^2} - 1\right) dt. \quad \text{(A.17)}$$

Since this form of integral appears many times in later part of derivation, I define $\phi(t)$ and $M_n(a, b)$ as follows:

$$\phi(t) = \sin^{-1}\left(\frac{1}{2t^2} - 1\right), \quad \text{(A.18)}$$

$$M_n(a, b) = \int_a^b t^n \, \phi(t) \, dt, \quad \text{(A.19)}$$

and the desired integral can be written as follows:

$$2\int_{1/4}^{x^2} \sin^{-1}\left(\frac{1}{2u} - 1\right) du = 4M_1\left(\frac{1}{2}, x\right). \quad \text{(A.20)}$$

To evaluate $M_1(a,b)$, defining $p = \frac{1}{2t^2} - 1$ is helpful. Integrating by parts:

$$\begin{aligned} M_n(a,b) &= \int_a^b t^n \sin^{-1} p \, dt \\ &= -\frac{1}{\sqrt{2^{n+3}}} \int_{p_a}^{p_b} \frac{\sin^{-1} p}{(p+1)^{\frac{n+3}{2}}} dp \\ &= \frac{1}{\sqrt{2^{n+3}}} \frac{2}{n+1} \left[\frac{\sin^{-1} p}{(p+1)^{\frac{n+1}{2}}} \right]_{p_a}^{p_b} \\ &\quad - \frac{1}{\sqrt{2^{n+3}}} \frac{2}{n+1} \int_{p_a}^{p_b} \frac{1}{(p+1)^{\frac{n+1}{2}}} \frac{1}{\sqrt{1-p^2}} dp, \end{aligned} \tag{A.21}$$

where $p_a = \frac{1}{2a^2} - 1$ and $p_b = \frac{1}{2b^2} - 1$. Taking $p = \cos 2\theta$,

$$M_n(a,b) = \frac{1}{n+1} [t^{n+1} \phi(t)]_a^b + \frac{1}{2^n} \frac{1}{n+1} \int_{\theta_a}^{\theta_b} \frac{1}{\cos^{n+1} \theta} d\theta, \tag{A.22}$$

where $\theta_a = \frac{1}{2} \cos^{-1} \left(\frac{1}{2a^2} - 1 \right)$ and $\theta_b = \frac{1}{2} \cos^{-1} \left(\frac{1}{2b^2} - 1 \right)$.

When $n = 1$,

$$\int_{\theta_a}^{\theta_b} \frac{1}{\cos^2 \theta} d\theta = \left[\tan \left(\frac{1}{2} \cos^{-1} \left(\frac{1}{2t^2} - 1 \right) \right) \right]_a^b = [2t^2 \cos \phi(t)]_a^b. \tag{A.23}$$

This result produces:

$$M_1(a,b) = \frac{1}{2} [t^2 (\phi(t) + \cos \phi(t))]_a^b, \tag{A.24}$$

and

$$M_1 \left(\frac{1}{2}, x \right) = \frac{1}{2} [x^2 (\phi(x) + \cos \phi(x))] - \frac{\pi}{16}. \tag{A.25}$$

Therefore, the CDF of X is obtained as follows:

$$F_X(x) = \begin{cases} 0 & x \le 0 \\ \pi x^2 & 0 < x \le \frac{1}{2} \\ 2[x^2(\phi(x) + \cos\phi(x))] & \frac{1}{2} < x \le \frac{1}{\sqrt{2}} \\ 1 & \frac{1}{\sqrt{2}} \le x \end{cases}. \tag{A.26}$$

From Eq. (19), the derivative of $M_1\left(\frac{1}{2}, x\right)$ is easily obtained:

$$\frac{d}{dx} M_1\left(\frac{1}{2}, x\right) = \frac{d}{dx} \int_{\frac{1}{2}}^{x} t\ \phi(t)\ \ dt = x\ \phi(x). \tag{A.27}$$

Therefore, the PDF of X is as follows:

$$f_X(x) = \begin{cases} 0 & x \le 0 \\ 2\pi x & 0 < x \le \frac{1}{2} \\ 4x\ \phi(x) & \frac{1}{2} < x \le \frac{1}{\sqrt{2}} \\ 0 & \frac{1}{\sqrt{2}} \le x \end{cases}. \tag{A.28}$$

A.3 PDF and CDF of component *Y*

From the definition of CDF, the CDF of $Y = \left|U_3 - \frac{1}{2} + \frac{1}{2\alpha}\right|^{-1}$ can be written as probability of U_3 satisfying a specific condition:

$$F_Y(y) = \mathrm{P}\left[\left(U_3 - \frac{1}{2} + \frac{1}{2\alpha}\right)^{-1} \le y\right] = \mathrm{P}\left[U_3 > \frac{1}{y} + \frac{1}{2} - \frac{1}{2\alpha}\right]. \tag{A.29}$$

Defining β as:

$$\beta = \frac{1}{2}\left(\frac{1}{\alpha} - 1\right), \tag{A.30}$$

The CDF of Y is as follows:

$$F_Y(y) = 1 - \mathrm{P}\left[U_3 \le \frac{1}{y} - \beta\right] = \begin{cases} 0 & y \le \dfrac{1}{\beta+1} \\ 1 + \beta - \dfrac{1}{y} & \dfrac{1}{\beta+1} < y \le \dfrac{1}{\beta} \\ 1 & \dfrac{1}{\beta} < y \end{cases}. \tag{A.31}$$

The PDF of Y is the first derivative of the CDF:

$$f_Y(y) = \frac{d}{dy} F_Y(y) = \begin{cases} 0 & y \le \dfrac{1}{\beta+1} \\ -\dfrac{1}{y^2} & \dfrac{1}{\beta+1} < y \le \dfrac{1}{\beta} \\ 0 & \dfrac{1}{\beta} < y \end{cases}. \tag{A.32}$$

A.4 The outline of PDF and CDF of S_{M1}

From the discussions in previous subsections, PDFs of random variables X and Y are obtained. The PDF of random variable X is nonzero when $0 < x \le 1/\sqrt{2}$, and the PDF of random variable Y is nonzero when $\frac{1}{\beta+1} < y \le \frac{1}{\beta}$. Figure A.1 shows the location where PDFs are nonzero (Domains A and B), and black lines are contours of $S_{M1} = XY$. Note that for different distortion parameters, contours intersect with Domain B ($1/2 < x \le 1/\sqrt{2}$) in a different way. For distortion parameter $\alpha > 1 - \frac{\sqrt{2}}{2} \approx 0.293$, the contours run the nonzero domain horizontally, while they run vertically for distortion parameter $\alpha < 1 - \frac{\sqrt{2}}{2}$.

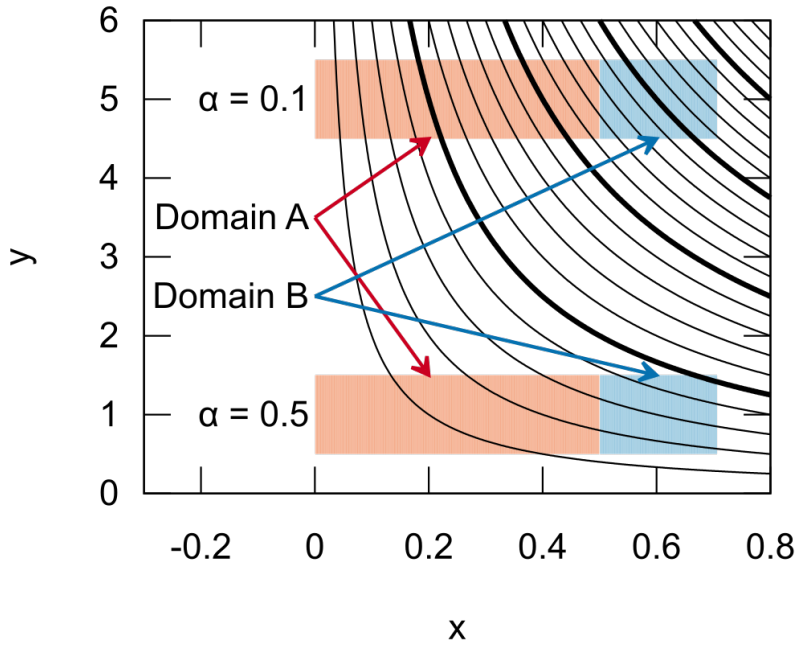

Fig. A.1. Contours of $s - xy$ and domains A and B for $\alpha = 0.1$ and $\alpha = 0.5$. The contours are from 0.2 to 4.6 with interval of 0.2. Thick contours are at $s = 1, 2, 3$, and 4.

Because the way of intersection depends on the distortion parameter, the PDF and CDF of S_{M1} have three subtypes. Each subtype consists of several piecewise continuous functions. Integration intervals are as follows:

$$
\begin{array}{lllll}
(1) & x_A \le \frac{1}{2} & \text{and} & x_B \le \frac{1}{2} \\
(2) & x_A \le \frac{1}{2} & \text{and} & \frac{1}{2} < x_B \le \frac{1}{\sqrt{2}} \\
(3) & x_A \le \frac{1}{2} & \text{and} & \frac{1}{\sqrt{2}} < x_B \\
(4) & \frac{1}{2} < x_A \le \frac{1}{\sqrt{2}} & \text{and} & \frac{1}{2} < x_B \le \frac{1}{\sqrt{2}} \\
(5) & \frac{1}{2} < x_A \le \frac{1}{\sqrt{2}} & \text{and} & \frac{1}{\sqrt{2}} < x_B \\
(6) & \frac{1}{\sqrt{2}} < x_A & \text{and} & \frac{1}{\sqrt{2}} < x_B
\end{array}
\tag{A.33}
$$

where $x_A = \beta s$ and $x_B = (\beta + 1)s$. The first subtype of PDF and CDF uses (1), (2), (3), (5), and (6), the second subtype (1), (2), (4), (5), (6), and the third subtype (1), (2), (5), (6). The first subtype corresponds to less distorted particle $\alpha < 1 - \frac{\sqrt{2}}{2}$, second subtype corresponds to more distorted particle $\alpha > 1 - \frac{\sqrt{2}}{2}$ and the third subtype is only when $\alpha = 1 - \frac{\sqrt{2}}{2}$. In following subsections, I derive the explicit formulae for each subsection.

A.5 PDF and CDF of S_{M1} in each interval

Before starting, I evaluate the integral $M_2(a,b)$. From Eq. (A.22),

$$M_2(a,b) = \frac{1}{3}[t^3\phi(t)]_a^b + \frac{1}{12}\int_{\theta_a}^{\theta_b} \frac{1}{\cos^3\theta}\,d\theta. \tag{A.34}$$

Integrating the integral on the right hand side by parts, the integral produces itself as follows:

$$\begin{aligned}\int_{\theta_a}^{\theta_b} \frac{1}{\cos^3\theta}\,d\theta &= \int_{\theta_a}^{\theta_b} \frac{1}{\cos^2\theta}\frac{1}{\cos\theta}\,d\theta \\ &= \left[\frac{\tan\theta}{\cos\theta}\right]_{\theta_a}^{\theta_b} - \int_{\theta_a}^{\theta_b} \frac{\tan^2\theta}{\cos\theta}\,d\theta \\ &= \left[\frac{\tan\theta}{\cos\theta}\right]_{\theta_a}^{\theta_b} - \int_{\theta_a}^{\theta_b} \frac{1}{\cos\theta}\,d\theta - \int_{\theta_a}^{\theta_b} \frac{1}{\cos^3\theta}\,d\theta\end{aligned} \tag{A.35}$$

Thus,

$$M_2(a,b) = \frac{1}{3}[t^3\phi(t)]_a^b + \frac{1}{24}\left[\frac{\tan\theta}{\cos\theta}\right]_{\theta_a}^{\theta_b} + \frac{1}{24}\int_{\theta_a}^{\theta_b} \frac{1}{\cos\theta}\,d\theta. \tag{A.36}$$

Defining $q = \ln\left(\tan\left(\frac{\theta}{2}+\frac{\pi}{4}\right)\right)$, the derivative of q is $1/\cos\theta$ as follows:

$$\begin{aligned}\frac{dq}{d\theta} &= \frac{1}{2\tan\left(\frac{\theta}{2}+\frac{\pi}{4}\right)}\frac{1}{\cos^2\left(\frac{\theta}{2}+\frac{\pi}{4}\right)} \\ &= \frac{1}{\sin\left(\theta+\frac{\pi}{2}\right)} \\ &= \frac{1}{\cos\theta}.\end{aligned} \tag{A.37}$$

Substituting Eq. (A.37) to Eq. (A.36),

$$M_2(a,b) = \frac{1}{3}[t^3\phi(t)]_a^b + \frac{1}{24}\left[\frac{\tan\theta}{\cos\theta}\right]_{\theta_a}^{\theta_b} + \frac{1}{24}[q(\theta)]_{\theta_a}^{\theta_b}. \tag{A.38}$$

With the properties of trigonometric functions, q can be simplified as follows:

$$q(\theta) = \ln\left(\tan\left(\frac{\theta}{2}+\frac{\pi}{4}\right)\right) = \ln\left(\tan\theta + \frac{1}{\cos\theta}\right). \tag{A.39}$$

In addition,

$$\tan\theta = \tan\left(\frac{1}{2}\cos^{-1}\left(\frac{1}{2t^2}-1\right)\right) = 2t^2\cos\phi(t)\text{, and} \tag{A.40}$$

$$\frac{1}{\cos\theta} = \frac{1}{\cos\left[\frac{1}{2}\cos^{-1}\left(\frac{1}{2t^2}-1\right)\right]} = \frac{\sqrt{2}}{\sqrt{1+\left(\frac{1}{2t^2}-1\right)}} = 2t. \tag{A.41}$$

Substituting Eq. (A.39) through Eq. (A.41) into Eq. (A.38),

$$M_2(a,b) = \frac{1}{3}\left[t^3\left(\phi(t)+\frac{1}{2}\cos\phi(t)\right) + \frac{1}{8}\ln(2t+2t^2\cos\phi(t))\right]_a^b. \tag{A.42}$$

A.5.1 $x_A \le \frac{1}{2}$ *and* $x_B \le \frac{1}{2}$

This is when only the domain A is involved in the integral.

$$\begin{aligned} I_{A1} &= \int_0^{x_A} f_X(x)\,dx + \int_{x_A}^{x_B} f_X(x)P\left(Y \le \frac{s}{x}\right)dx \\ &= \int_0^{x_a} f_X(x)\,dx + \int_{x_A}^{x_B} f_X(x)\left((\beta+1)-\frac{x}{s}\right)dx \\ &= P(X \le x_B) + \beta[P(X \le x_B) - P(X \le x_A)] - \frac{1}{s}\int_{x_A}^{x_B} 2\pi x^2\,dx. \end{aligned} \tag{A.43}$$

The integral can be evaluated as follows:

$$\frac{2\pi}{s}\int_{x_A}^{x_B} x^2\,dx = \frac{2\pi}{3s}[x_B^3 - x_A^3] = \frac{2\pi}{3}[(\beta+1)^3 - \beta^3]s^2. \tag{A.44}$$

Therefore, the CDF of S_{M1} is

$$F_{S_{M_1}}(s) = I_{A1} = \frac{1}{3}[(\beta+1)^3 - \beta^3]\pi s^2, \tag{A.45}$$

and the PDF is derived as the first derivative of the CDF as follows:

$$f_{S_{M_1}}(s) = \frac{2}{3}[(\beta+1)^3 - \beta^3]\pi s. \tag{A.46}$$

A.5.2 $x_A \le \frac{1}{2}$ *and* $\frac{1}{2} < x_B \le \frac{1}{\sqrt{2}}$

The CDF involves both domain A and domain B. The integral in domain A is defined as I_{A2} and the integral in domain B is defined as I_{B2}. The CDF is $F_{S_{M1}}(x) = I_{A2} + I_{B2}$. The integral I_{A2} is the special case of the integral I_{A1} with the upper limit being $1/2$:

$$\begin{aligned} I_{A2} &= \int_0^{x_A} f_X(x)\,dx + \int_{x_A}^{\frac{1}{2}} f_X(x) P\left(Y \le \frac{s}{x}\right) sx \\ &= P(X \le x_B) + \beta\left[P\left(X \le \frac{1}{2}\right) - P(X \le x_A)\right] - \frac{1}{s}\int_{x_A}^{\frac{1}{2}} 2\pi x^2\,dx \\ &= \frac{\pi}{4} + \beta\pi\left(\frac{1}{4} - {x_A}^2\right) - \frac{2\pi}{3s}\left(\frac{1}{8} - {x_A}^3\right) \\ &= \frac{\pi}{4}(\beta+1) - \frac{\pi}{3}\beta^3 s^2 - \frac{\pi}{12s} \end{aligned} \tag{A.47}$$

$$I_{B2} = \int_{\frac{1}{2}}^{x_B} f_X(x)\left((\beta+1) - \frac{x}{s}\right)dx$$

$$= (\beta+1)\left[P(X \le x_B) - \frac{\pi}{4}\right] - \frac{4}{s}\int_{\frac{1}{2}}^{x_B} x^2\phi(x)\,dx \tag{A.48}$$

$$= -\frac{\pi}{4}(\beta+1) + 2{x_B}^2(\beta+1)[\phi(x_B) + \cos\phi(x_B)] - \frac{4}{s}M_2\left(\frac{1}{2}, x_B\right).$$

From Eq. (A.42), we can write M_2 as follows:

$$M_2\left(\frac{1}{2}, x_B\right) = \frac{1}{3}\left[{x_B}^3\left(\phi(x_B) + \frac{1}{2}\cos\phi(x_B)\right)\right.$$
$$\left. + \frac{1}{8}\ln(2x_B + 2{x_B}^2\cos\phi(x_B))\right] - \frac{\pi}{48}. \tag{A.49}$$

Therefore, the CDF of S_{M1} is obtained as:

$$F_{S_{M1}}(s) = -\frac{\pi}{3}{x_A}^2\beta + \frac{2}{3}{x_B}^2(\beta+1)[\phi(x_B) + 2\cos\phi(x_B)]$$
$$- \frac{1}{6s}\ln(2x_B + 2{x_B}^2\cos\phi(x_B)). \tag{A.50}$$

Differentiating Eq. (A.48) with respect to s,

$$\frac{d}{ds}I_{B2} = 4(\beta+1)^2 s\phi(s) + \frac{4}{s^2}M_2\left(\frac{1}{2}, x_B\right) - \frac{4}{s}\frac{d}{ds}M_2\left(\frac{1}{2}, x_B\right) \tag{A.51}$$

and utilizing:

$$\frac{d}{ds}M_2\left(\frac{1}{2}, x_B\right) = (\beta+1){x_B}^2\phi(x_B) = (\beta+1)^2 s x_B\phi(x_B), \tag{A.52}$$

I_{B2} is simplified as follows:

$$\frac{d}{ds}I_{B2} = \frac{4}{s^2}M_2\left(\frac{1}{2}, x_B\right). \tag{A.53}$$

Therefore, the PDF of S_{M1} is as follows:

$$f_{S_{M_1}}(s) = -\frac{2\pi}{3}x_A\beta^2 + \frac{4}{3}x_B(\beta+1)^2\left[\phi(x_B) + \frac{1}{2}\cos\phi(x_B)\right] + \frac{1}{6s^2}\ln(2x_B + 2{x_B}^2\cos\phi(x_B)). \tag{A.54}$$

A.5.3 $x_A \le \frac{1}{2}$ *and* $\frac{1}{\sqrt{2}} < x_B$

The CDF involves both domain A and domain B. The integral in domain A is already computed as I_{A2} and the integral in domain B is defined as I_{B3}. The CDF is thence $F_{S_{M_1}}(x) = I_{A2} + I_{B3}$. The integral I_{B3} is the special case of the integral I_{B2} with the upper limit being $1/\sqrt{2}$:

$$\begin{aligned} I_{B2} &= \int_{\frac{1}{2}}^{\frac{1}{\sqrt{2}}} f_X(x)\left((\beta+1) - \frac{x}{s}\right)dx \\ &= (\beta+1)\left(1-\frac{\pi}{4}\right) - \frac{4}{s}\int_{\frac{1}{2}}^{\frac{1}{\sqrt{2}}} x^2\phi(x)\,dx \\ &= (\beta+1)\left(1-\frac{\pi}{4}\right) - \frac{4}{s}M_2\left(\frac{1}{2},\frac{1}{\sqrt{2}}\right). \end{aligned} \tag{A.55}$$

From Eq. (A.42), M_2 can be written as:

$$M_2\left(\frac{1}{2},\frac{1}{\sqrt{2}}\right) = \frac{1}{12\sqrt{2}} + \frac{1}{24}\ln\left(\sqrt{2}-1\right) - \frac{\pi}{48}. \tag{A.56}$$

Therefore, the CDF and PDF of S_{M1} are obtained as follows:

$$F_{S_{M_1}}(x) = (\beta+1) - \frac{\pi}{3}\beta{x_A}^2 - \frac{1}{s}\left[\frac{1}{3\sqrt{2}} + \frac{1}{6}\ln\left(\sqrt{2}-1\right)\right]. \tag{A.57}$$

$$f_{S_{M_1}}(x) = -\frac{2\pi}{3}\beta^2 x_A + \frac{1}{s^2}\left[\frac{1}{3\sqrt{2}} + \frac{1}{6}\ln\left(\sqrt{2}-1\right)\right]. \tag{A.58}$$

A.5.4 $\frac{1}{2} < x_A \leq \frac{1}{\sqrt{2}}$ ***and*** $\frac{1}{2} < x_B \leq \frac{1}{\sqrt{2}}$

The CDF involves both domain A and domain B. The integral in domain A is defined as I_{A4} and the integral in domain B is defined as I_{B4}. The CDF is $F_{S_{M1}}(x) = I_{A4} + I_{B4}$. Since $x_A > 1/2$, $I_{A4} = \pi/4$.

$$I_{A4} = \int_0^{\frac{1}{2}} f_X(x)\, dx = \frac{\pi}{4} \tag{A.59}$$

The integral in the domain B is as follows:

$$\begin{aligned} I_{B4} &= \int_{\frac{1}{2}}^{x_A} f_X(x)\, dx + \int_{x_A}^{x_B} f_X(x)\left((\beta+1) - \frac{x}{s}\right) dx \\ &= -\frac{\pi}{4} + (\beta+1)P(X \leq x_B) - \beta P(X \leq x_A) - \frac{4}{s}\int_{x_A}^{x_B} x^2 \phi(x)\, dx \\ &= -\frac{\pi}{4} + 2{x_B}^2(\beta+1)(\phi(x_B) + \cos\phi(x_B)) \\ &\quad - 2{x_A}^2\beta(\phi(x_A) + \cos\phi(x_A)) - \frac{4}{s}M_2(x_A, x_B) \end{aligned} \tag{A.60}$$

From Eq. (A.42),

$$\begin{aligned} M_2(x_A, x_B) = \frac{s}{3}\Big[&{x_B}^2(\beta+1)\left(\phi(x_B) + \frac{1}{2}\cos\phi(x_B)\right) \\ &- {x_A}^2\beta\left(\phi(x_A) + \frac{1}{2}\cos\phi(x_A)\right)\Big] \\ &+ \frac{1}{24}[\ln(2x_B + 2{x_B}^2\cos\phi(x_B)) \\ &- \ln(2x_A + 2{x_A}^2\cos\phi(x_A))], \end{aligned} \tag{A.61}$$

and

$$I_{B4} = -\frac{\pi}{4} + \frac{2}{3}{x_B}^2(\beta+1)(\phi(x_B) + 2\cos\phi(x_B)) - \frac{2}{3}{x_A}^2\beta(\phi(x_A) + 2\cos\phi(x_A)) - \frac{1}{6s}[\ln(2x_B + 2{x_B}^2\cos\phi(x_B)) - \ln(2x_A + 2{x_A}^2\cos\phi(x_A))]. \quad \text{(A.62)}$$

Therefore, the CDF of S_{M1} is as follows:

$$F_{S_{M1}}(s) = \frac{2}{3}{x_B}^2(\beta+1)(\phi(x_B) + 2\cos\phi(x_B)) - \frac{2}{3}{x_A}^2\beta(\phi(x_A) + 2\cos\phi(x_A)) - \frac{1}{6s}[\ln(2x_B + 2{x_B}^2\cos\phi(x_B)) - \ln(2x_A + 2{x_A}^2\cos\phi(x_A))]. \quad \text{(A.63)}$$

The PDF is obtained by differentiating Eq. (A.60) as follows:

$$\frac{d}{ds}F_{S_{M1}} = (\beta+1)\frac{d}{ds}P(X \le x_B) - \beta\frac{d}{ds}P(X \le x_A) - \frac{4}{s}\frac{d}{ds}M_2(x_A, x_B) + \frac{4}{s^2}M_2(x_A, x_B). \quad \text{(A.64)}$$

First three terms in the right hand side of Eq. (A.64) cancel out because

$$\frac{d}{ds}P(X \le x_A) = \beta f_X(x_A) = 4x_A\beta\phi(x_A), \quad \text{(A.65)}$$

$$\frac{d}{ds}P(X \le x_B) = (\beta+1)f_X(x_B) = 4x_B(\beta+1)\phi(x_B), \text{ and} \quad \text{(A.66)}$$

$$\frac{d}{ds}M_2(x_A, x_B) = s[x_B(\beta+1)^2\phi(x_B) - x_A\beta^2\phi(x_A)]. \quad \text{(A.67)}$$

Therefore, the PDF of $S_{M1}$is:

$$\begin{aligned} f_{S_{M_1}}(x) &= \frac{4}{s^2} M_2(x_A, x_B) \\ &= \frac{4}{3}\Big[x_B(\beta+1)^2\left(\phi(x_B)+\frac{1}{2}\cos\phi(x_B)\right) \\ &\quad - x_A\beta^2\left(\phi(x_A)+\frac{1}{2}\cos\phi(x_A)\right)\Big] \\ &\quad + \frac{1}{6s^2}[\ln(2x_B + 2{x_B}^2\cos\phi(x_B)) \\ &\quad - \ln(2x_A + 2{x_A}^2\cos\phi(x_A))]. \end{aligned} \tag{A.68}$$

A.5.5 $\frac{1}{2} < x_A \leq \frac{1}{\sqrt{2}}$ ***and*** $\frac{1}{\sqrt{2}} < x_B$

The CDF involves both domain A and domain B. The integral in domain A is I_{A4} and the integral in domain B is defined as I_{B5}. Note that I_{B5} is a special case of I_{B4} when the upper limit of the integral is $1/\sqrt{2}$. The CDF is thence $F_{S_{M_1}}(x) = I_{A4} + I_{B5}$. The integral in domain B is as follows:

$$\begin{aligned} I_{B5} &= \int_{\frac{1}{2}}^{x_A} f_X(x)\,dx + \int_{x_A}^{\frac{1}{\sqrt{2}}} f_X(x)\left((\beta+1) - \frac{x}{s}\right)dx \\ &= -\frac{\pi}{4} + (\beta+1) - \beta P(X \leq x_A) - \frac{4}{s}\int_{x_A}^{\frac{1}{\sqrt{2}}} x^2\phi(x)\,dx \\ &= -\frac{\pi}{4} - 2{x_A}^2\beta(\phi(x_A) + \cos\phi(x_A)) - \frac{4}{s}M_2\left(x_A, \frac{1}{\sqrt{2}}\right). \end{aligned} \tag{A.69}$$

From Eq. (A.42),

$$M_2\left(x_A, \frac{1}{\sqrt{2}}\right) = \frac{s}{3}\left[\frac{1}{4\sqrt{2}}(\beta+1) - {x_A}^2\beta\left(\phi(x_A) + \frac{1}{2}\cos\phi(x_A)\right)\right] + \frac{1}{24}\left[\ln\left(\sqrt{2}+1\right) - \ln(2x_A + 2{x_A}^2\cos\phi(x_A))\right], \tag{A.70}$$

and

$$I_{B5} = -\frac{\pi}{4} + \frac{1}{3}(\beta+1) - \frac{2}{3}{x_A}^2\beta(\phi(x_A) + 2\cos\phi(x_A)) - \frac{1}{6s}\left[\ln\left(\sqrt{2}+1\right) - \ln(2x_A + 2{x_A}^2\cos\phi(x_A))\right]. \tag{A.71}$$

Therefore, the CDF of S_{M1} is as follows:

$$F_{S_{M1}}(s) = \frac{1}{3}(\beta+1) - \frac{2}{3}{x_A}^2\beta(\phi(x_A) + 2\cos\phi(x_A)) - \frac{1}{6s}\left[\ln\left(\sqrt{2}+1\right) - \ln(2x_A + 2{x_A}^2\cos\phi(x_A))\right]. \tag{A.72}$$

The PDF is obtained by differentiating Eq. (A.69) as follows:

$$\frac{d}{ds}F_{S_{M1}} = -\beta\frac{d}{ds}P(X \le x_A) - \frac{4}{s}\frac{d}{ds}M_2\left(x_A, \frac{1}{\sqrt{2}}\right) + \frac{4}{s^2}M_2\left(x_A, \frac{1}{\sqrt{2}}\right) \tag{A.73}$$

First two terms in the right hand side of Eq. (A.73) cancel out because

$$\frac{d}{ds}P(X \le x_A) = \beta f_X(x_A) = 4x_A\beta\phi(x_A), \text{ and} \tag{A.74}$$

$$\frac{d}{ds}M_2\left(x_A, \frac{1}{\sqrt{2}}\right) = -sx_A\beta^2\phi(x_A). \tag{A.75}$$

Therefore, the PDF of $S_{M1}$is:

$$f_{S_{M_1}}(x) = \frac{4}{s^2} M_2\left(x_A, \frac{1}{\sqrt{2}}\right)$$

$$= \frac{\sqrt{2}}{3}(\beta+1)^2 - \frac{4}{3}x_A\beta^2\left(\phi(x_A) + \frac{1}{2}\cos\phi(x_A)\right) \tag{A.76}$$

$$+ \frac{1}{6s^2}\left[\ln\left(\sqrt{2}+1\right) - \ln(2x_A + 2{x_A}^2\cos\phi(x_A))\right]$$

A.5.6 $\frac{1}{\sqrt{2}} < x_A$ ***and*** $\frac{1}{\sqrt{2}} < x_B$

This is when the contour does not cross any of two domains. The CDF and PDF are as follows:

$$F_{S_{M_1}}(x) = 1, \text{and} \tag{A.77}$$

$$f_{S_{M_1}}(x) = 0. \tag{A.78}$$